UAB

Universitat Autònoma de Barcelona

Facultat de Ciències - Departament de Física

Estudis de Doctorat en Ciència de Materials

Simple and Low Cost Nanostructured Plasmonic Biosensor for Sensitive and Multiplexed Biodetection

Doctoral Thesis - October 2018

Gerardo Arturo López Muñoz

Author

Prof. Laura M. Lechuga Gómez

Director

Dr. Mª Carmen Estévez Alberola

Co-Director

Dr.Eva Maria Pellicer Vilà

Tutor

ICN2

Institut Català de Nanociència i Nanotecnologia

EXCELENCIA SEVERO OCHOA

To divine love and to all my loved ones,

Eat, Pray and Love

Abstract

The increasing demand for analytical platforms that are reliable and, at the same time, easy to use and compact, that require low sample consumption and provide high sensitivity and real-time response, have provided considerable innovation in the design of biosensor devices in the last years. Among all of them, those based on Surface Plasmon Resonance phenomena (SPR) have been the subject of great scientific interest because they provide high sensitivity and simplicity in the detection schemes. With the advance in nanofabrication techniques, the development of optical sensors based on plasmonic nanostructures has represented an excellent way to integrate them into Lab-on-a-chip platforms with a small size, with the ability to solve some of the current challenges related to the analysis time, the volume of sample required and the feasibility of detecting several analytes at the same time.

With the purpose of offering simple and inexpensive biosensor tools, this Doctoral Thesis presents the development of nanoplasmonic biosensors integrated in Lab-on-a-Chip (LOC) platforms for the multiplexed biosensing of different analytes in real time. The developed sensor is based on the use of commercial Blu-Ray discs as a substrate containing nano-slits to generate the plasmon resonance phenomena by coating them with different metallic layers at a nanometric scale. The new nanobiosensors are a very promising alternative that could replace conventional analytical techniques, simplifying processes and overcoming the main current challenges related to sensitivity, cost and time required for clinical diagnosis.

The first part of this Thesis includes a theoretical analysis of the optical behavior of plasmonic nanostructures by using different types and thicknesses of metal layers under a reflectance detection scheme. For this purpose, Finite Differences in the Time Domain (FDTD) simulations were performed. Once the designs were selected, a manufacturing scheme was developed for the different materials and their combinations at laboratory scale, as well as the integration with the corresponding microfluidics to develop Lab-on-a-Chip prototypes.

Next, the assembly of the corresponding experimental systems and the optical characterization of the sensors were done in order to evaluate their performance as a sensor. Proofs of concept were developed to evaluate their capacity as a biosensor without the need of using any labeling, studying the detection of an antigen associated with the early detection of colon cancer and the presence of C-reactive protein, a biomarker related to inflammation and infection processes.

On the other hand, a microfluidic system was developed to allow the multianalyte detection of biomarkers using a biosensor with four independent channels. Different microfluidic designs were evaluated to promote a homogenous flow division and, as a consequence, a homogeneous mass transfer between the sensor channels. A spatial multiplexed system was proposed as the optical reading platform. Proofs-of-concept were developed to evaluate the capacity as a multianalyte biosensor with four channels of the manufactured sensors, studying the presence of the C reactive protein in buffer solution and in urine with a coefficient of variation between the sensor channels close to 10%. For the multi-analyte biodetection, the presence of C-reactive protein and interleukin-6 was studied. A localized deposition of the metallic layer was proposed to spatially separate the process of immobilization of the corresponding antibodies. The biosensor was able to detect both analytes without any cross-interference between them.

Finally, the development of a multilayer biosensor combining silver/gold nanolayers with the aim of improving the biosensing capacity of the final device is presented. A comparative study was made between the sensor with a gold monolayer and the multilayer silver/gold sensor. An improvement in the chemical stability of the multilayer sensor was observed when using a three-layer gold/silver/gold structure without the increase of plasmonic losses due to ohmic effects, also achieving nanostructures with very low roughness (surface roughness <0.5 nm). When evaluating the performance as biosensor of the three-layer sensor, it was possible to improve the performance in up to **95%** (for the Figure of Merit) with the three-layer gold/silver/gold sensor compared with the gold monolayer sensor.

Resumen

La creciente demanda de plataformas de análisis que sean fiables y, al mismo tiempo, fáciles de usar y compactas, que requieran un bajo consumo de muestras y proporcionen una alta sensibilidad y una respuesta en tiempo real, ha proporcionado una considerable innovación en el diseño de los dispositivos biosensores en los últimos años. Entre todos ellos, aquellos basados en fenómenos de Resonancia de Plasmón Superficial (SPR) han sido objeto de un gran interés científico en las últimas décadas porque aportan una alta sensibilidad y simplicidad en los esquemas de detección. Con el avance de las técnicas de nanofabricación, el desarrollo de sensores ópticos basados en nanoestructuras plasmónicas ha representado una excelente vía para su integración en plataformas Lab-on-a-chip de reducido tamaño, con la capacidad de resolver algunos de los retos actuales relacionados con los tiempos de análisis, el volumen de muestra requerido y la viabilidad de detectar varios analitos a la vez de forma multiplexada.

Con el propósito de ofrecer herramientas biosensoras simples y de bajo costo, la presente Tesis Doctoral presenta el desarrollo de biosensores nanoplasmónicos integrados en plataformas Lab-on-a-Chip (LOC) para la biodetección multiplexada de diferentes analitos en tiempo real. El nuevo sensor desarrollado se basa en el empleo de soportes comerciales de discos Blu-Ray como un sustrato que contiene nano-rejillas para general el fenómeno de resonancia de plasmón al recubrirlos con diferentes capas metálicas a escala nanométrica. Los nanobiosensores desarrollados constituyen una alternativa muy prometedora que podrían sustituir a las técnicas de análisis convencionales, simplificando los procesos y superando los principales retos actuales relacionados con la sensibilidad, el coste y el tiempo requerido para el diagnóstico clínico.

La primera parte de la tesis incluye un análisis teórico del comportamiento óptico de las nanoestructuras plasmónicas al utilizar diferentes tipos y espesores de capas metálicas bajo un esquema de detección por reflectancia. Para este propósito, se realizaron simulaciones de Diferencias Finitas en el Dominio del

Tiempo (FDTD). Una vez que se seleccionaron los diseños, se desarrolló un esquema de fabricación para los diferentes materiales y sus combinaciones a escala de laboratorio, así como la integración con la microfluídica correspondiente para desarrollar prototipos Lab-on-a-Chip.

A continuación, se diseñó el montaje de los sistemas experimentales correspondientes y se procedió a la caracterización óptica de los sensores para evaluar su capacidad como sensor. Se desarrollaron pruebas de concepto para evaluar la capacidad como biosensor sin necesidad de marcaje de los sensores fabricados, estudiando la detección de un antígeno asociado a la detección precoz del cáncer de colon y la presencia de la proteína C reactiva, un biomarcador relacionado con inflamación y procesos de infección.

Por otro lado, se desarrolló un esquema microfluídico que permitiera la detección multianalito del sensor con cuatro canales. Se evaluaron diferentes diseños microfluídicos que promovieran una división de flujo homogéneo y, como consecuencia, una transferencia de masa homogénea entre los canales sensores. Se propuso un sistema multiplexado espacial como la plataforma de lectura óptica. Se desarrollaron pruebas de concepto para evaluar la capacidad como biosensor multianalito con cuatro canales de los sensores fabricados, estudiando la presencia de la proteína C reactiva en solución buffer y en orina con un coeficiente de variación entre los canales sensores cercano al 10%. Para la biodetección multi-analito, se estudió la presencia de la proteína C reactiva y de la proteína interleuquina-6. Se propuso una deposición localizada de la capa metálica para separar espacialmente el proceso de inmovilización de los anticuerpos correspondientes. El biosensor fue capaz de detectar ambos analitos sin interferencia cruzada entre ellos.

Finalmente, se procedió al desarrollo de un biosensor multicapa combinando nanocapas de plata/oro con el objetivo de mejorar la capacidad de biodetección del dispositivo final. Se realizó un estudio comparativo entre el sensor con una monocapa de oro y el sensor multicapa de plata/oro. Se observó una mejora en la estabilidad química del sensor de multicapa al utilizar una estructura tricapa oro/plata/oro sin el incremento de pérdidas plasmónicas por efectos óhmicos,

logrando además obtener nanoestructuras de muy baja rugosidad (rugosidad superficial <0.5 nm). Al evaluar el comportamiento como biosensor del sensor tricapa, se logró mejorar el rendimiento en hasta el 95% (para la Figura de Mérito) con el sensor tricapa oro/plata/oro comparando con el sensor monocapa de oro.

Acknowledgements

Al final nos damos cuenta que la vida nos lleva a las personas y los momentos necesarios para nuestra propia evolución y que todo lo que nos molesta de otros seres es sólo una proyección de lo que no hemos resuelto de nosotros mismos. Tenemos dos opciones seguir dormidos o despertar y simplemente disfrutar de la sinfonía de la vida. Cada persona en nuestra vida se asemeja al instrumento de una orquesta, existirán instrumentos que prefiramos y otros que no nos agraden, sin embargo, sería estúpido no disfrutar de todos pues el conjunto de todos ellos da armonía a la sinfonía de la vida. Le agradezco al amor divino, a todos mis seres queridos y a los que no soy de su agrado porque quien yo soy este día es gracias a todos esos pequeños detalles y experiencias del día a día. Quisiera acabar este mensaje para cada uno de ustedes con este versículo *"Y aún más, yo estimo como pérdida todas las cosas en vista del incomparable valor de conocer a Cristo Jesús, mi Señor, por quien lo he perdido todo, y lo considero como basura a fin de ganar a Cristo."* Considerando la esencia del mensaje divino yo lo expresaría de la siguiente forma este día: *"Y aún más, yo estimo como pérdida todas las cosas (mis apegos, mis miedos y mis reconocimientos) en vista del incomparable valor de conocer el amor genuino, por quien lo he perdido todo, y lo considero como basura a fin de vivir y sentir el amor todos los días de mi vida."* Así sea, así es.

Quiero agradecer a mis Directoras de Tesis Laura L. y Mari Carmen E. quienes depositaron su confianza y su guía en mi persona. A pesar de las diferencias y adversidades ellas creyeron en mi potencial para llevar este proyecto a su culminación.

A todos los integrantes que son parte o formaron parte del grupo NanoB2A pues el compartir con cada uno de ustedes me ha llevado a evolucionar como hombre y como espíritu día a día. No deseo priorizar o dar importancia a una u otra persona pues todas son importantes en la sinfonía de mi vida. Así que lo único que puedo terminar diciéndoles es: "Yo decreto que el señor y la vida les multiplique mil

veces sus deseos para conmigo, así como el señor y la vida me multiplique mil veces los deseos que yo tengo para con ustedes" Así sea, así es.

Gerardo A. López Octubre 2018

"Perfect love casts out fear. Where there is love there are no demands, no expectations, no dependency. I do not demand that you make me happy; my happiness does not lie in you. If you were to leave me, I will not feel sorry for myself; I enjoy your company immensely, but I do not cling."

Amar sin poseer.
Acompañar sin invadir.
Vivir sin depender.

"Happiness is our natural state. Happiness is the natural state of little children, to whom the kingdom belongs until they have been polluted and contaminated by the stupidity of society and culture. To acquire happiness, you don't have to do anything, because happiness cannot be acquired. Does anybody know why? Because we have it already. How can you acquire what you already have? Then why don't you experience it? Because you've got to drop something. You've got to drop illusions. You don't have to add anything in order to be happy; you've got to drop something. Life is easy, life is delightful. It's only hard on your illusions, your ambitions, your greed, and your cravings. Do you know where these things come from? From having identified with all kinds of labels!"

Anthony de Mello

Table of Contents

Motivation

Biosensor devices provide the possibility to create miniaturized tools containing some of the functionalities of an entire analytical laboratory; this fact has increased the scientific research during the last decades. Over the last years, a multitude of biosensing platforms based on different detection schemes have been proposed for application in a wide variety of fields that range from environmental monitoring to medical diagnosis. Despite the recent technological achievements, the transition from proof-of-concept devices at a laboratory scale to real application in field with a tangible impact on research and industry is often lacking. On the other hand, this may be correlated to the fact that most of the recent biosensing platforms are based on complex and expensive fabrication methods with bulky detection schemes, limiting their use mainly to laboratory scale. As a consequence, biosensor devices with a simple and reproducible fabrication schemes with high potential to portable detection schemes are highly desirable. Between the different sensing technologies, those optical sensors based on plasmonic nanostructures have represented an excellent way to integrate them into Lab-on-a-chip platforms of small size and with the possibility to move them to real applications by solving one of the main challenges related to the efficient biofunctionalization of the sensing surface.

In this context, simple nanostructure-based plasmonic biosensing platforms represent a highly attractive tool for multiplexed detection and the development of portable point-of-care (POC) platforms in a cost-effective manner. Under this assumption, the main objective of this thesis is focused on developing a novel nanoplasmonic biosensor based on industrially produced Blu-ray optical discs as a substrate containing nano-slits to generate the plasmon resonance phenomena by coating them with different metallic layers on a nanometric scale. The final scope is the integration into lab-on-a-chip (LOC) platform for the real-time and simultaneous detection of different biomarkers in human fluids.

Objectives

The main objective of this work is organized as follows:

- *Sensor Design and Fabrication Scheme*

- ➢ The computation of finite-difference time-domain (FDTD) optical simulations to analyze the plasmon resonance generation in nanostructured optical discs by coating them with different metallic layers on a nanometric scale and at different incident angles of light.

- ➢ The development of a fabrication scheme for plasmonic sensors using Blu-ray optical discs as substrates containing nano-slits.

- ➢ The analysis of batch to batch reproducibility of the fabricated plasmonic sensors

- *Sensor Integration and Multianalyte Platform*

- ➢ The development and fabrication of the microfluidic design and the optical readout for a single and multichannel biosensing platform.

- ➢ The development of proof-of-concepts to evaluate their performance as multianalyte biosensor.

- *Multilayer Au/Ag Sensing Platform*

- ➢ The development and fabrication scheme of a gold/silver/gold trilayer biosensor and their evaluation as biosensing platform.

Chapter 1. Introduction

This chapter comprises a general introduction to nanoplasmonic biosensing. A short description of biosensors and its subfield, optical biosensors, is followed by a brief discussion of refractometric biosensing based on Surface Plasmon Resonance phenomena in thin metallic layers and metallic nanostructures. Later, the key concepts of nanoplasmonic biosensing are discussed and a brief overview regarding the state-of-the-art of this research field to achieve Lab-on-a-Chip (LOC) platforms is given.

1.1 Fundamentals in Plasmonic biosensors

1.1.1 Definition of a biosensor and classification

What does a "biosensor" mean? The International Union of Pure and Applied Chemists (IUPAC), the recognized authority for chemical analysis, defines a biosensor as[1] "a device that uses specific biochemical reactions mediated by isolated enzymes, immunosystems, tissues, organelles or whole cells to detect chemical compounds usually by electrical, thermal or optical signals". Considering this definition, we focus on two key aspects: a biosensor is a device which uses a biological recognition element retained in direct spatial contact with a transduction system, and a biosensor is a device that converts a physical or biological event into a measurable signal. To achieve these, in general a biosensor consists of three main parts[2]: first a biomimetic material or recognition element (i.e. enzymes, antibodies, nucleic acids, etc.) that provides selectivity and specificity to detect the chemical or biochemical target (analyte); the second is a transducer (i.e. optical, electrochemical, mechanical, etc.) that converts or transforms the biomolecular interaction in a physical quantity, it which can be measured and quantified, commonly into an electrical signal. Finally, the third part is the signal processing that allows a user-friendly visualization of the results (see -Figure 1.1).
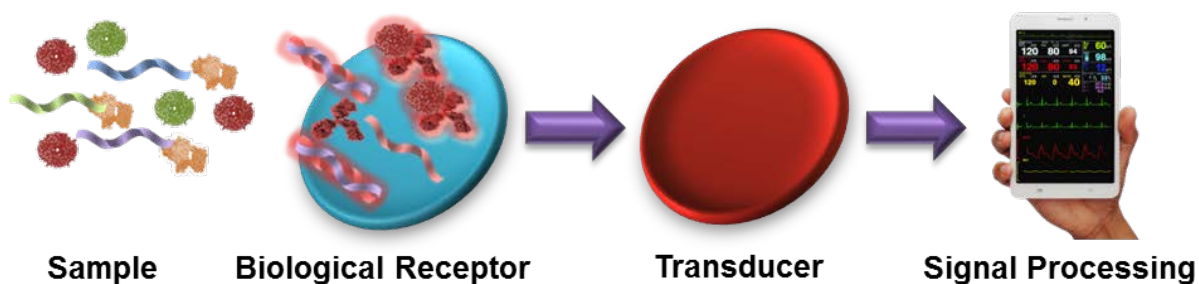
Figure 1.1 Schematic representation of a biosensor including the analyte in the sample, the recognition element, the transducer and the signal processing that allows a user-friendly visualization of the results.

As a complementary definition, we can define biosensors as tools used for analyzing biomolecular interactions, providing quantitative analytical information with elevated accuracy in a few minutes, using low sample volumes and minimum sample pretreatment without the need of trained personnel and complex bulky instrumentation. They are considered the most appropriate analytical tools to be miniaturized and integrating different functional components (i.e. microfluidics, electronics, etc.) in single LOC platforms that could render in the fabrication of portable and easy-to-use analytical devices[2]. The research and development of biosensors has extended in the last years due to the described promising advantages, and have contributed to advances in the next-generation of medical technologies such as individualized medicine and ultrasensitive point-of-care devices.

Considering the type of transducer employed in the detection, biosensors can be divided mainly into: electrochemical, mechanical and optical biosensors[3].

Electrochemical biosensors are based on the measurement of electrochemical changes in the medium caused by the biomolecular interaction; the working electrode of the biosensor is covered by the recognition component and at an applied potential, conversion of electroactive species generated in the enzyme layer occurs at the electrode, and the resulting current is quantified. They are the most commonly used biosensors mainly due to their analytical features, related with a simple and high-throughput fabrication scheme, and simplicity of instrumentation[4].

One of the best examples of this technology is the glucose biosensor. Leland C. Clark introduced their working principle in 1962; it was based on a potentiometric measurement of glucose oxidase immobilized in the enzymatic electrode to quantify glucose in blood plasma. In less than 15 years after the Clark report, the first glucometer was commercially available in 1975 by Yellow Springs Instrument Company (YSI; Yellow Springs, Ohio, USA), until our days the detection scheme of commercial glucometers is based on the amperometric detection of hydrogen peroxide[4]. Although great improvements have been made in electrochemical biosensors, there are many challenges to overcome, especially those involving the development of new materials to improve the specificity and sensitivity of biorecognition events, and those involving the stability of these biosensor devices[5,6].

In mechanical biosensors, the biochemical interaction is measured as changes of mass on the surface of the transducer. The quartz crystal microbalance is the most representative biosensor device based on this detection scheme[7]. The quartz crystal microbalance (QCM) operation principle is based on the decrease in the crystal's resonant frequency following the binding of the target biomolecules. When a mass binds to the oscillating surface, the shift in the resonance frequency is proportional to the mass bound[8]. This was first proved by Sauerbrey in 1959. Henceforth, QCM has been used to quantify the number of target cells[9] and bacteria[10] in a sample. Mechanical biosensors have attractive features such as label-free detection and high multiplexing capabilities. However, the mechanical nature of the sensing mechanism requires high precision and alignment which makes the diagnosing systems expensive[11]. Also, the water environment causes thermal management issues, leading to erroneous readings[12].

Optical biosensors detect the biological interaction by measuring variations of the different optical properties of the propagated light, such as intensity, wavelength, refractive index or polarization[13]. Optical biosensors are mainly based in the evanescent wave mechanism[14]. These biosensors exploit the possibility of the electromagnetic (EM) wave confinement in interfaces with different refractive index values, which can result in either localized or propagating EM modes[14]. Part of the EM mode penetrates into the external medium, forming a so-called evanescent field.

The evanescent field acts as a probe to detect refractive index (RI) changes providing a quantitative measure for the analyte involved in the biomolecular interaction[15]. Besides, given the exponential decay of the evanescent wave into the external medium, only changes that take place close to the surface of the material on which the light is propagated can be detected, thereby minimizing the possibility of interference with other substances present in the solution. As a direct consequence, biosensors based on this sensing principle do not need of any molecular label, thereby allowing label-free detection[16]. To date, most of evanescent field biosensors can be distinguished between those using conventional dielectric waveguides like interferometers[17] and resonators[18,19] (Figure 1.2A, left), and those based on plasmonic modes at a planar metal-dielectric interface (Figure 1.2A, right). These devices achieve high detection sensitivities with short response times; they do not suffer from electromagnetic or mechanical interferences and present potential miniaturization capabilities[19].
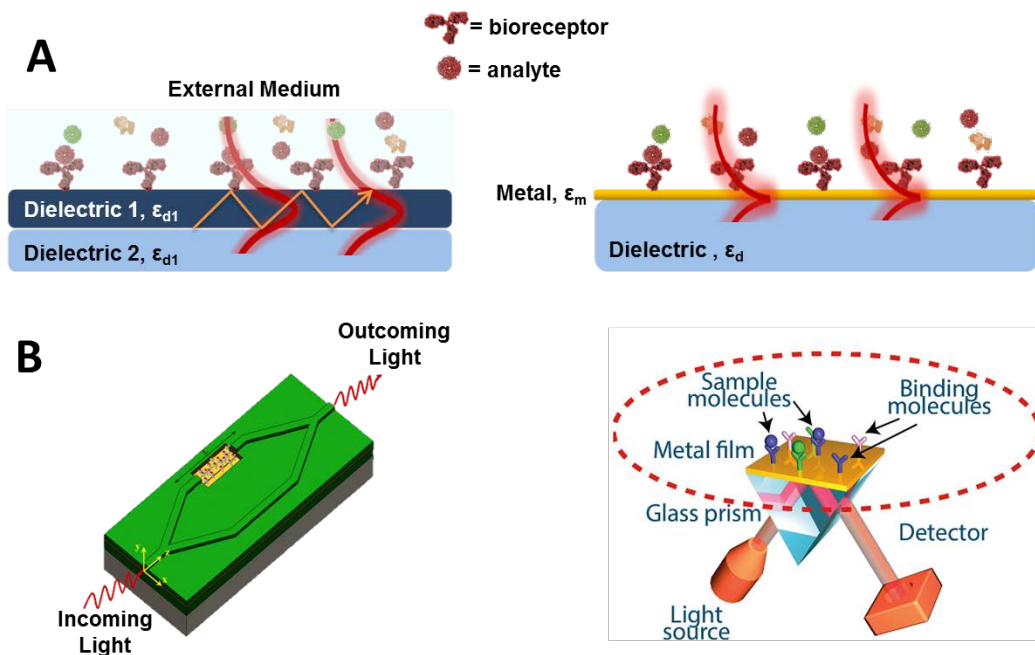

Figure 1.2 (A) Schematics depicting the sensing principle of evanescent wave sensors, thereby distinguishing between those devices relying on conventional waveguides (left), and those on surface plasmon resonances (right). (B) The Mach-Zehnder interferometer and the SPR based on Kretschmann configuration are examples of biosensors based on these sensing principles.

1.1.2 Plasmonic biosensors

For more than three decades, the field of optical sensing has been dominated by sensing platforms based on Surface Plasmon Resonance (SPR), since the introduction of plasmonic based refractometric sensors by Nylander and Liedberg[20]. Plasmonic biosensors are nowadays the most widely used and commercialized label-free optical sensors, and have become a widespread tool for the study of any type of biochemical interactions[20]. They show excellent properties for its application in different fields that range from environmental monitoring[21] to medical diagnosis[22].

How does a "surface plasmon resonance" biosensor work? Surface plasmon resonances occur when a photon of incident light hits a metallic surface. At a certain condition like momentum or wavelength between others, a portion of the light energy couples through the metal coating with the electrons in the metal surface layer, which then move due to excitation. The electron movements are called plasmon, and they propagate parallel to the metal surface[23] (see Figure 1.3). The plasmon oscillation in turn generates an EM field with their maxima located at the metal-dielectric interface and exhibit exponentially decaying evanescent fields into both media (whose range is in the nm order from the boundary between the metal surface and sample solution).
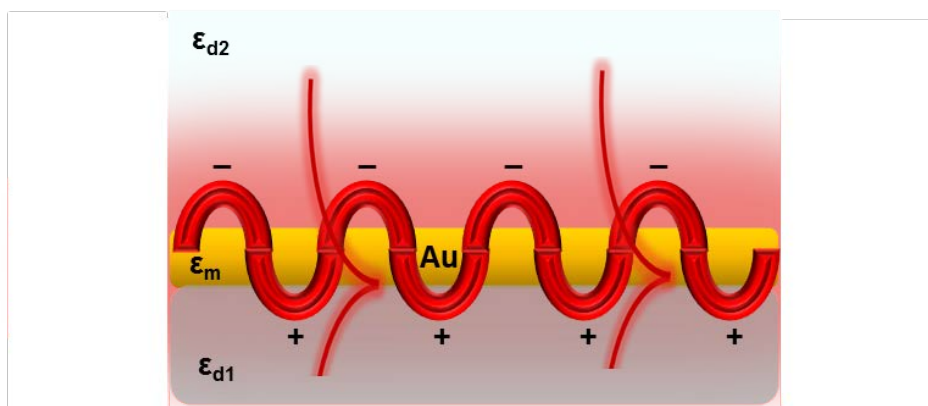
Figure 1.3 Longitudinal collective oscillations of the conduction electrons for the generation of surface plasmons, and the exponential decay of the evanescent wave into the external medium.

The evanescent wave sensors, which include SPR sensors, are mainly based on the propagation of light due to total internal reflection (TIR) according to Snell's law:

$$n_1 \sin \theta_1 = n_2 \sin \theta_2 \qquad (1.1)$$

where θ_1 is the angle of incidence, θ_2 the angle of refraction, and n_1 and n_2 the refractive index of the bottom dielectric and the top dielectric/metal, respectively. The Snell's law describes that light will propagate on TIR if $n_2 > n_1$, and under a critical angle θ_c. At the critical angle θ_c the angle of refraction θ_2 is equals to 90°. Thus, the critical angle can be expressed as:

$$\theta_c = sin^{-1}\left(\frac{n_2}{n_1}\right) \qquad (1.2)$$

Under TIR condition an evanescent field is generated at the interface between the different refractive index materials and extends into the sample. The intensity, I_z, of the evanescent field at position z can be expressed as:

$$I_z = I_0 e^{-z/d} \qquad (1.3)$$

where I_0 is the maximum intensity of the evanescent field at the interface between the materials (z = 0), and d is the penetration depth. I_0 is related to the intensity of the incident beam by a complex function of incident angle and polarization.

In particular, the surface plasmon resonances in thin metal films are limited to transverse-magnetic (TM) modes (the magnetic vector is perpendicular to the direction of propagation of the wave and parallel to the plane of the interface) and it is characterized by an evanescent field distribution and its propagation vector[24] as in the following equation

$$k_x^{SPR} = \frac{2\pi}{\lambda} \sqrt{\frac{\varepsilon_m \varepsilon_{d2}}{\varepsilon_m + \varepsilon_{d2}}} \qquad (1.4)$$

In this equation, ε_m and ε_d are the dielectric constants corresponding to the metal and the dielectric, respectively, while k_0 represents the wave vector of light in vacuum. To satisfy these conditions, the real part of the metal's dielectric constant at certain wavelengths must be negative, that is, $Re[\varepsilon_m] < 0$, and $Re[\varepsilon_d] < -Re[\varepsilon_d]$. These conditions are satisfied by a wide amount of metals (Al, Au, Ag, Cu, Cr, and Pt) in the wavelength range from 400 to 800 nm. Nevertheless, normally gold is mainly used due to its optical properties in the visible to near infrared light spectrum[23,24] simplifying the instrumentation for the surface plasmon resonance generation, it possess an excellent chemical resistance, and there are well-known surface biofunctionalization methods (i.e. thiol-gold chemistry). Besides, due to the relatively low imaginary part of the dielectric constant of gold and silver, losses caused by plasmonic damping are strongly suppressed when compared with other plasmonic materials[25]. Even though it is possible to fulfil the excitation of the plasmonic wave with these metals, there is a specific metallic layer thickness associated with the configuration and the excitation wavelength that allows an optimized transfer of energy from the light source to the plasmon wave. The metallic layer properties are critical; with thickness above 150 nm in some cases the layer behaves as a mirror, as consequence it is relevant to study the influence of the metallic layer thickness on the generation of the plasmonic effect under the different configuration schemes[26].

To achieve the generation of surface plasmon resonances, the light wave's vector parallel to the interface must match the propagation vector of the surface plasmons:

$$k_x^{SPR} = \frac{2\pi}{\lambda} \sqrt{\varepsilon_d} \sin \theta = k_x^{ligth} \qquad (1.5)$$

Generally, due to the SPR propagation vector being considerably larger than the number of light waves in the dielectric, surface plasmons cannot be excited by direct illumination. In order to overcome this fact, several techniques can be

employed to enhance the wavevector of the incoming light by means of prism coupling, waveguide coupling and grating coupling methods[27-29] (Figure 1.4).
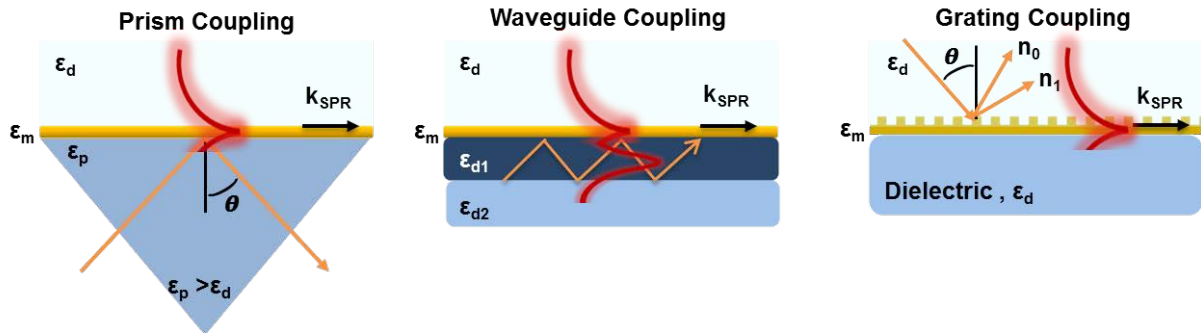
Figure 1.4 SPR coupling methods; from left to right: prism-coupled Kretschmann configuration, waveguide coupling and grating coupling.

The prism coupling method in a Kretschmann configuration (Figure 1.3 right) is the most common method used for optical excitation of surface plasmons. In a Kretschmann configuration, light passes through a high RI prism (ε_p) and is TIR at the prism base, generating an evanescent wave which penetrates the metal film[27]. The generated evanescent wave propagates along the interface with a certain propagation vector which can be adjusted by matching that of the SPR in two ways: by changing the angle of incidence of a monochromatic light, or by changing the wavelength of light at a fixed incident angle.

In Kretschmann configuration the TIR occurs when the magnitude of the parallel wavevector of the evanescent wave, κ_x, is the same as the magnitude of the wavevector of the surface plasmon, κ_{SPR}:

$$k_{SPR} = \frac{2\pi}{\lambda} \sqrt{\frac{n_d^2 n_m^2}{n_d^2 + n_m^2}} = k_x = \frac{2\pi}{\lambda} n_p \sin\theta \qquad (1.6)$$

where λ is the wavelength of incident light, n_d is the refractive index of the sensing medium, n_m is the refractive index of the metal, n_p is the refractive index of the prism, and θ is the incident angle. For this configuration the resonant or critical angle θ_c is given by:

$$\theta_c = \sin^{-1}\left(\frac{1}{n_p}\sqrt{\frac{n_d^2 n_m^2}{n_d^2 + n_m^2}}\right) \qquad (1.7)$$

From this last expression, we can observe that the critical angle increases linearly with the increasing RI of the sensing media. The evanescent field generated by the plasmon resonances extends into the sensing medium; the penetration depth into the sample medium, d_{SPR} is given by the following expression:

$$d_{SPR} = \text{Im}\left[\frac{\lambda}{4\pi n_d}(\varepsilon_m + n_c^2)^{1/2}\right] \qquad (1.8)$$

where Im is the image of the function and ε_m the dielectric constant of the metal. Depending on the configuration, this penetration depth is between ≈ 100 to 500 nm in the visible range of light[27].

Similarly, excitation can be achieved by using optical waveguides. The light is guided by an optical waveguide by TIR and, when it propagates to the region where is located the thin metal layer, it evanescently penetrates through the metal layer exciting plasmons at its external interface[28] (Figure 1.4 center).

Finally, excitation via grating couplers is based on the diffraction of the light wave. Wood was the first to observe SPR excitation by grating coupling. In grating-based SPR configuration, an optical wave is made incident on a periodically modulated surface of a rectangular metallic grating under an angle of incidence θ and in the plane of incidence perpendicular to the grating grooves. At the surface of the metal grating, the incident optical wave is partially reflected and partially split to a series of diffracted waves (diffraction orders), which are either evanescent or propagating back into the dielectric[29] (Figure 1.4 right). The component of the diffracted wavevector k_{SPR} for the m order of the diffracted monochromatic light parallel to the interface can be expressed as[29-30]:

$$k_{SPR}^m = k_x n_d \sin\theta + m\frac{2\pi}{\Lambda} \qquad (1.9)$$

where m is de diffraction order, k_x is the component of the wavevector of the incident light along the grating surface, n_d is the refractive index of the sensing medium, , θ the incidence angle of light and Λ the period of the grating. The momentum conservation for an optical wave exciting the plasmonic resonances via a diffraction grating can be expressed as[31]:

$$n_d \sin \theta_R + m \frac{\lambda}{\Lambda} = \pm \sqrt{\frac{\varepsilon_m n_d^2}{\varepsilon_m + n_d^2}} \qquad (1.10)$$

where θ_R is the resonant angle of incidence, ε_m is the dielectric constant of the metal and λ is the wavelength of the incident light.

Although some studies suggest that grating coupled plasmonic sensors have a limited sensing performance compared to those based on prism couplers[30-31], they offer highly attractive features: direct coupling of the light (no bulky prism is required) and gratings can be fabricated by high-throughput techniques into plastic substrates and as a direct consequence, it can provide an avenue to low-cost plasmonic sensors[30]. These facts and the limited reports of biosensing based on plasmonic grating couplers compared to those based on prism couplers open a wide field of research, and make plasmonic sensors based on grating couplers a highly attractive candidate for highly integrated plasmonic sensors of low cost.

As mentioned before, the refractometric plasmonic sensing concept is based on the detection of the local RI changes that take place near the surface of the metal-dielectric interface. When a biomolecular reaction occurs, it induces a local RI change that alters the plasmonic wavevector, and thus provides a quantitative methodology for the label-free detection of biomolecular interactions that take place close to the metal surface[32]. Hence, a plasmonic biosensor is based on the prior immobilization of specific receptor molecules on the metallic thin film surface, in which the latter acts as a transducer.

In general, a plasmonic biosensor scheme typically comprises the following components: a light source (either mono-chromatic or broadband), a plasmonic transducer (a thin metal layer) that incorporates the biomolecular recognition element on its surface, a detector (intensity- or phase-based) and a fluidic system for sample confinement at the sensing surface and for sample delivery. Figure 1.5 illustrates a typical grating coupled plasmonic biosensor scheme.
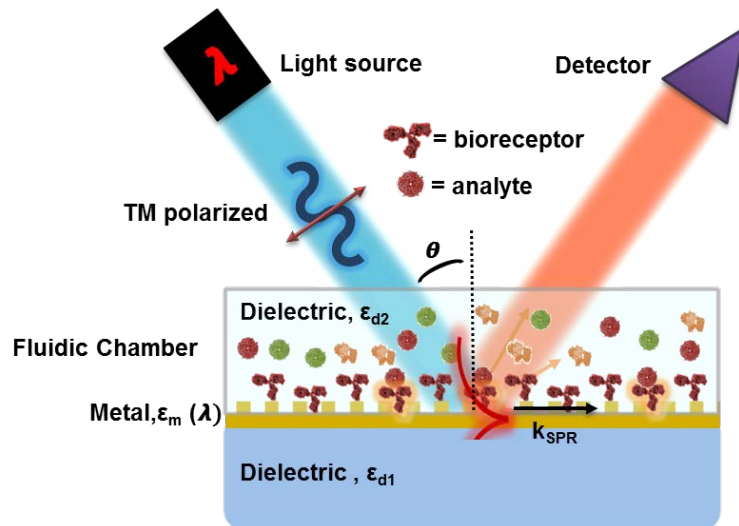
Figure 1.5 Schematics of a grating coupled SPR biosensing configuration.

As we previously described, plasmonic excitation can be achieved by either using light wavelength (λ) or angle of incidence (θ) as tuning parameters. When working with a monochromatic source (i.e. laser, or a narrow band LED), the reflected light is measured as a function of θ. At a certain critical angle, the reflected intensity exhibits a strong decrease, until a minimum value is reached[32,33]. Commonly, for this configuration, the changes in the plasmon resonances are detected by fixing θ at the position where the slope of the resonance curve is maximized, after which the intensity changes of the reflected light are monitored as a function of time.

On the other hand, when illuminating with a broadband light source (i.e. halogen or white lamps) at a fixed θ, detection is performed by the spectral analysis of the reflected light. The reflectivity spectrum shows a minimum dip located at λ_{SPR}, which is subjected to spectral displacements induced by the changes of RI in the

surface of the sensing area, and it can be tracked as a function of time. Working in either two of the schemes, biochemical interactions can be directly monitored in real time, allowing the evaluation of the affinity and kinetic studies in a simple, rapid and label-free manner (see Figure 1.6).
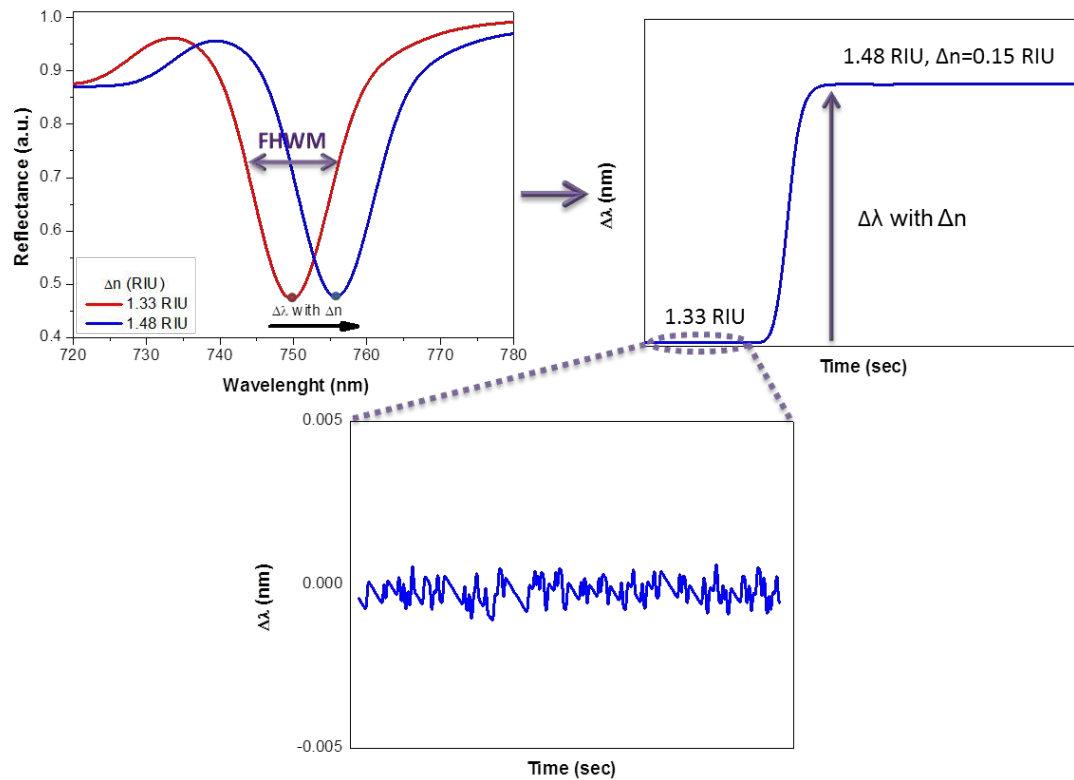
Figure 1.6 Representative SPR curve for a λ interrogated SPR sensor, together with their corresponding real-time tracking of curve displacements via the monitoring of shifts of the resonance wavelength, λ_{SPR}. The insert shows the noise level of a SPR sensorgram estimated by the monitoring of the baseline over the time.

The performance of a plasmonic sensor is mainly evaluated through their capability to detect changes in the monitored quantity (the refractive index), which ultimately determines the sensitivity (*S*) of the sensor. As both sensing schemes (θ and λ) are generally characterized by a peak-shaped response, *n* can be defined as the shift of the peak position λ_{SPR} upon dielectric changes in the environment, this shift will be either the wavelength position λ_{SPR} or the angle position θ_{SPR} of the resonance depending on the detection scheme. Therefore, the sensitivity a plasmonic sensor (*S*) can be expressed as the variation of (λ or θ)$_{SPR}$ per RI (n) unit change:

$$S = \frac{\Delta\lambda,\theta_{SPR}}{\Delta n} \qquad (1.11)$$

A second factor affecting the sensing performance is its resolving precision to detect changes of the monitored quantity. This parameter is typically represented by the full width at half maximum (FWHM) of the resonance peak (FWHM is the width of a spectrum curve measured between those points on the *y*-axis which are half the maximum amplitude): a sharp peak facilitates the registration of a peak shift and vice versa.

Therefore, when considering the performance of a sensor, it is necessary to evaluate both sensitivity and peak width. From the relation of these two parameters, the figure of merit (FOM) is defined as:

$$FOM = \frac{\delta}{FWHM} \qquad (1.12)$$

FOM correlates both quantities (the sensitivity and the FWHM) and can be used to quantify the general performance of a sensor. It also allows the comparison of the sensor with their counterparts. Finally, the limit of detection (LOD) is the lowest RI change likely to be reliably distinguished from the baseline noise and at which detection is feasible and is defined as:

$$LOD = \frac{3\sigma}{S} \qquad (1.13)$$

where σ is the standard deviation of the baseline over the time in a sensorgram in nm and *S* the sensitivity of the plasmonic sensor expressed in nm·RIU^{-1}.

1.1.3 Plasmonics in metallic nanostructured materials

Meanwhile plasmonic waves propagate through the continuous metallic film at a dielectric interface, localized surface plasmons are confined excitations of the conduction electrons of metallic nanostructures coupled to the electromagnetic field.

These modes arise naturally from the light scattering of sub-wavelength conductive nanostructures in an oscillating electromagnetic field[34]. The edges of the nanostructures exert an effective restoring force on the driven electrons, so that a resonance can arise, leading to field amplification in the near-field zone outside the nanostructure. This resonance is called Localized Surface Plasmon[34]. Another consequence of the edged surface is that plasmon resonances can be excited by direct light illumination, in contrast to conventional SPR (see Figure 1.7).
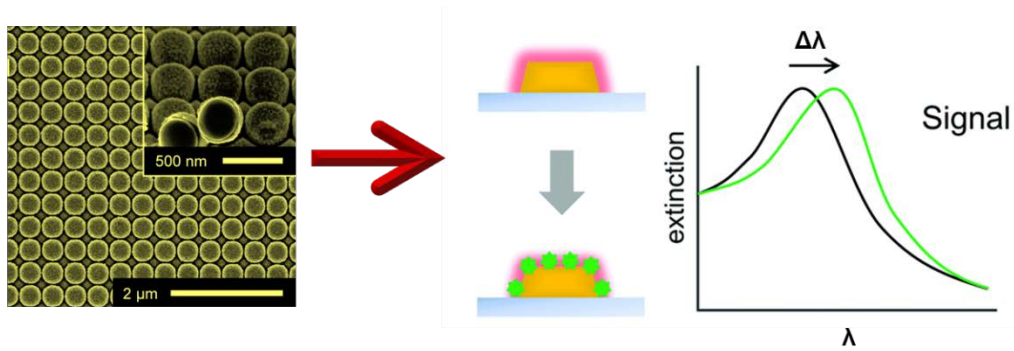
Figure 1.7 Plasmonic nanostructured materials. Gold nanodomes and the detection principle based on extinction wavelength shift.

The strong scatter and absorption present in metallic nanostructures is correlated with the resonant field enhancement due to a resonance of the polarizability[35]. This phenomenon is related with the following expression, which represents the (complex) polarizability of a small sphere of sub-wavelength diameter.

$$\alpha = 4\pi r^3 \frac{\varepsilon - \varepsilon_m}{\varepsilon + 2\varepsilon_m} \qquad (1.14)$$

Where α is the polarizability, r is the radius of the sphere, ε de dielectric function of the metal and ε_m the dielectric function of the surrounding media. From this expression it is evident that the polarizability has a resonant enhancement with a minimum value of |ε + 2εm|, which simplifies for a small Im [ε] to[35]:

$$\mathrm{Re}[\varepsilon(\omega)] = -2\varepsilon_m \qquad (1.15)$$

The relationship (1.15) is called the Fröhlich condition and the associated mode, the dipole surface plasmon of a metal nanoparticle; it expresses the strong dependence of the resonance frequency on the dielectric environment. The resonance red-shifts as ε_m increases and it explains why metallic nanostructures represent ideal platforms for refractometric optical sensing[36,37].

Analogous to SPR, LSPR is therefore exploited in biosensing applications, as the wavelength is highly dependent on the surrounding media[38]. The binding on the surface of the metallic nanostructures results in a refractive index change, causing a shift in the extinction peak wavelength, λ_{max}. This shift in λ_{max} is given by the following equation[39]:

$$\Delta\lambda_{max} \cong S\Delta n \left[1 - \exp(-\frac{2d}{l_d})\right] \qquad (1.16)$$

where S is the sensitivity, Δn is the change in the refractive index, d is the effective adsorbate layer thickness, and l_d is the electromagnetic field decay length. The extinction can be maximized by optimizing the nanostructure structural characteristics (i.e. metal type, size, shape, and structure orientation).

Conventional SPR sensors have proven effectiveness in the monitorization and characterization of biomolecular interactions with a sensitivity that usually ranges between 10^{-5} and 10^{-7} refractive index units[39] (RIU). In LSPR sensors, when using conventional nanostructures such as nanospheres, nanorods, or nanodisks, the sensitivity is in the same average range or even lower[40] (usually between 10^{-4} and 10^{-6} RIUs). Whereas in terms of bulk sensitivity SPR clearly outperforms LSPR, a significantly better surface sensitivity can be theoretically obtained in LSPR[40,41]. From a general point of view, although some works have dealt with this[41,42] there is still a lack of convincing studies which confirm whether LSPR is superior to SPR in terms of surface sensing performance.

The main difference in sensing performance is correlated with the following: in traditional propagated plasmonic biosensors, the evanescent decay expands several

tens of nanometers into the medium resulting in high sensitivity to bulk refractive index changes. In contrast, in LSPR, the electromagnetic field is highly confined close to the surface, with an average sensitive area that expands a few nanometers away from the surfaces[43-46] (see Figure 1.8).
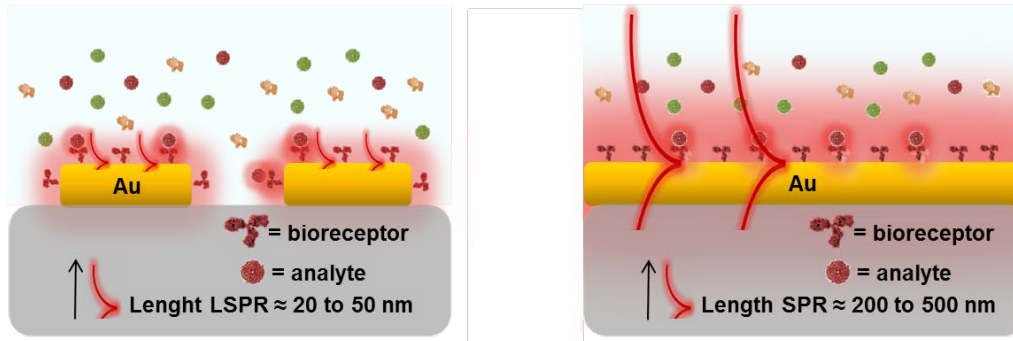
Figure 1.8 Representation of the differences in the evanescent decay length between a conventional SPR biosensor (right) and a LSPR biosensor (left).

As mention before, no bulky coupling methods are required in metallic nanostructures to generate LSPR: transmission, reflection and dark-field microscopy configurations are mainly used for detection[43] (see Figure 1.9). This last aspect expands the possibilities of nanoplasmonic devices as highly integrated biosensor devices[43]. However, the claimed enhanced sensitivity of nanoplasmonic devices has not been fully achieved yet and there is, in fact, some controversy regarding the real improvement that LSPR can provide in this regard compared with conventional SPR. Although the electromagnetic field is highly confined to the surface on LSPR sensors, other important factors correlated with their biosensing capabilities are the amount of bioreceptors that can be anchored to the nanostructures and the mass transport. The set of all these aspects makes similar the sensitivity between a SPR and a LSPR biosensor[43-45].
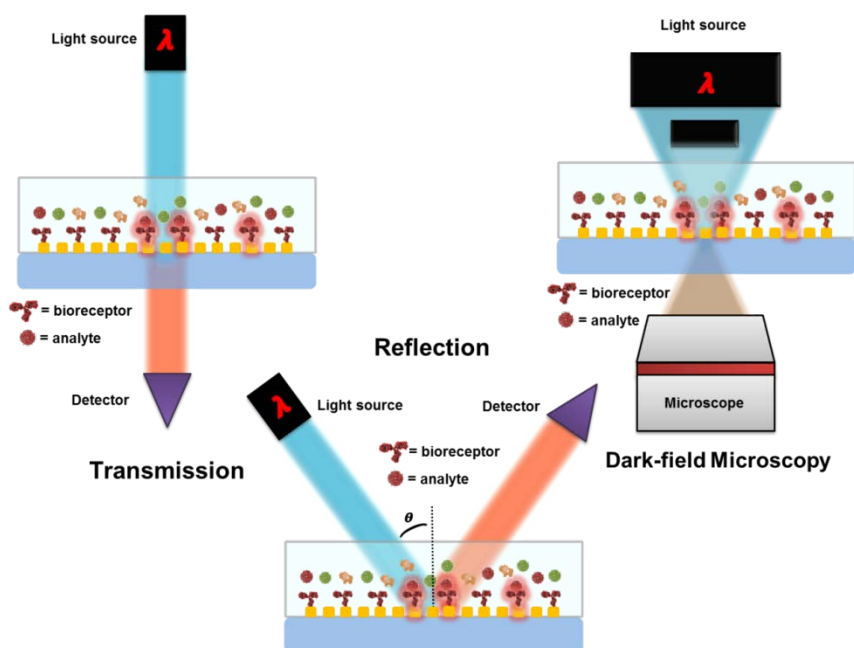
Figure 1.9 Schemes representing the most common configurations for nanoplasmonic sensing. From left to right: transmission, reflection and dark-field scattering microscopy.

The size of the biomolecules (receptors and target analyte), the thickness of the bioactive layer and the decay length of the evanescent field of the nanostructures[46] are therefore factors that are contributing to the final surface sensitivity. Furthermore, the EM field confinement makes LSPR less susceptible to bulk changes occurring in the media such as temperature fluctuations and more sensitive to smaller targets at lower concentrations. Sensitivity can be significantly enhanced if appropriate nanostructures are designed, exploiting geometries or arrangements that promote different resonance modes (i.e. surface enhanced Raman[47], fano-like[48] and cavity mode[49] resonances) and also promoting the interaction in those areas of the nanostructure with enhanced EM field[50]. Minimizing the influence of the substrate and assuring efficient coverage of the nanostructure to get optimal detection are crucial aspects to be resolved, whereas the effect of mass transport, concentration, affinity constants and microfluidics, should also definitely be taken into account.

1.1.4 Functional biorecognition layer

Many biomolecules can be used as bioreceptors, such as antibodies[52], nucleic acids[53], and aptamers[54], among others. Logically, the choice of the receptor biomolecule is strongly correlated with the foreseen application, thereby requiring high specificity for the selected target molecule. To achieve this end, several surface biofunctionalization strategies exist, among them direct immobilization strategies via physical absorption or covalent linking[55], and indirect immobilization approaches, such as non-covalent molecule binding to a previously deposited active layer, or physical entrapment of biomolecules in polymer layers and protein-protein binding[56] can be highlighted[56-57]. The indirect approaches try to minimize the direct contact of the biorecognition element with the sensor surface, to decrease desorption of the biomolecules and to increase the amount of molecular binding events by proper orientation of the bioreceptors (for example, when using antibodies). A representation of different surface modification protocols are summarized in Figure 1.10.
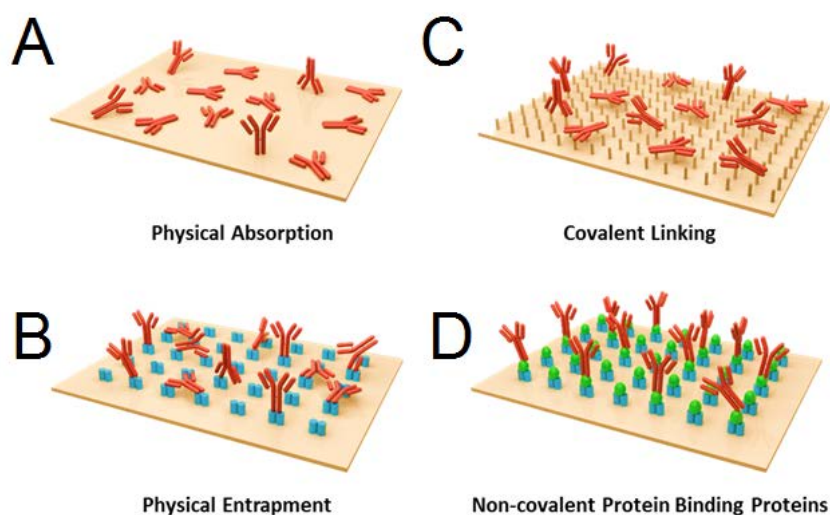
Figure 1.10 Schematic representation of different types of biofunctionalization processes: (A)physical adsorption, (B) physical entrapment in a polymer matrix, (C) covalent binding to a self-assembled monolayer (SAM) and (D) non-covalent molecule binding to a previously deposited active layer. Reprinted with permission from[56] 2016 Elsevier.

Physical adsorption is the simplest strategy to attach the bioreceptor to the sensor surface; it takes advantage of intermolecular forces like electrostatic,

hydrophobic and polar interactions[58] (Figure 1.10A). Although it is widely employed, physical adsorption suffers from two important drawbacks when dealing with biosensors: changes in the pH or buffer composition can lead to easily desorption of the biomolecules, and the uncontrolled interaction of the biomolecules with the surface can cause loss of affinity for the analyte[59].

Entrapment in polymers like dextran or polyaniline creates a uniform matrix allowing the inclusion of the bioreceptor as guest molecules in a single step without any modification of the receptor ensuring its biological activity[60] (Figure 1.10B). However, this technique can present important diffusion and mass transport problems of the analyte toward the entrapped bioreceptor[61,62].

Due to the above-described disadvantages, self- assembled monolayers (SAM) are an attractive strategy for the covalent immobilization of the biomolecules (Figure 1.10C). SAMs are amphiphilic molecules that self-organize onto the sensor surface creating a tight and high ordered matrix[63]. They possess an external functional group that can be activated to link molecules covalently. This procedure can offer significate benefits in the stability of the immobilization and the possibility to control the bioreceptor packing density by using lateral spacers[64-66]. To enhance the yield of the immobilization using SAMs it is important to optimize different factor that affect the efficiency of the attachment to the surface (i.e. pH, concentration, ionic strength, between others)[53].

However, the choice of the most suitable biofunctionalization strategy mainly depends on the application and the receptor characteristics. When enzymes or antibodies are employed as biorecognition elements, for example, the site-specific interaction with the target molecule might require an oriented immobilization to avoid the modification of the binding sites[53,67]. To this end, other functionalization strategies can surpass this challenge such as the ones using site-directed affinity proteins[67,68] (Figure 1.10D). Although these approaches offer site-specific functionalization, they also exhibit some drawbacks like the chemical modification of native biomolecules or the need of multi-step procedures [53,69].

Finally, it is desirable that the recognition biolayer is able to suppress non-specific adsorptions while maintaining its specificity and selectivity; these are the main factors for an excellent biosensor performance[69]. Minimizing the nonspecific adsorption is a major challenge for the application to real clinical scenarios[70,71]. Between the different strategies to reduce the non-specific adsorption of matrix components we can mention the following: the block of the surface with proteins[71] or polymers[72], the addition of surfactants[73] or other agents to the assay buffer and the dilution of the sample to minimize the background signal. However, each application requires particular strategies and conditions to reduce non-specific adsorption for conducting a label-free analysis. As consequence in the last years there has been a wide research in the development and optimization of functionalization strategies that can improve the detection selectivity while minimizing the nonspecific adsorptions at the same time.

.

1.1.5 State-of-the-art in Lab-on-a-Chip nanoplasmonic biosensors

As described previously, there are two main highlights of nanoplasmonic biosensors for the development of integrated LOC platforms: a high potential for integration and miniaturization possible thanks to the absence of bulky coupling methods, and a high potential to improve the sensing performance by the design of nanostructures that promote different photonic phenomena. The design and fabrication of a wide variety of nanostructures has become a fundamental field of research in constant growth. There have been intensive efforts to achieve fabrication process for high-performance nanoplasmonics substrates with innovative designs, which can be incorporated in cost effective biosensor platforms[34]. These fabrication processes can be classified mainly into two methods: top-down[74] and bottom-up[75].

Bottom-up methods are based mainly on chemical synthesis of nanoparticles[76] or colloidal lithography[77,78] and they fulfill some of the above commented aspects with fast, inexpensive and large-area-production. However, there are still challenges to improve their reproducibility and precision[79] compared with traditional top-down electron beam or focus ion beam lithographic[80,81] methods

in which material is removed to produce the nanostructures with a highly controlled shape and dimensions. In the last few years new nanofabrication processes have emerged and have the possibility of using flexible substrates. Between them: nanostencil lithography[82] (Figure 1.9A) based on shadow-masked pattering of the nanostructure, laser interference lithography[83] (Figure 1.9B), where an interference pattern is recorded in a photoresist material or nanoimprint lithography[84] (Figure 1.9C), that creates nanopatterns by mechanical deformation of imprint resist. All of them are processes that can achieve simple, scalable and cost effective fabrication methods.
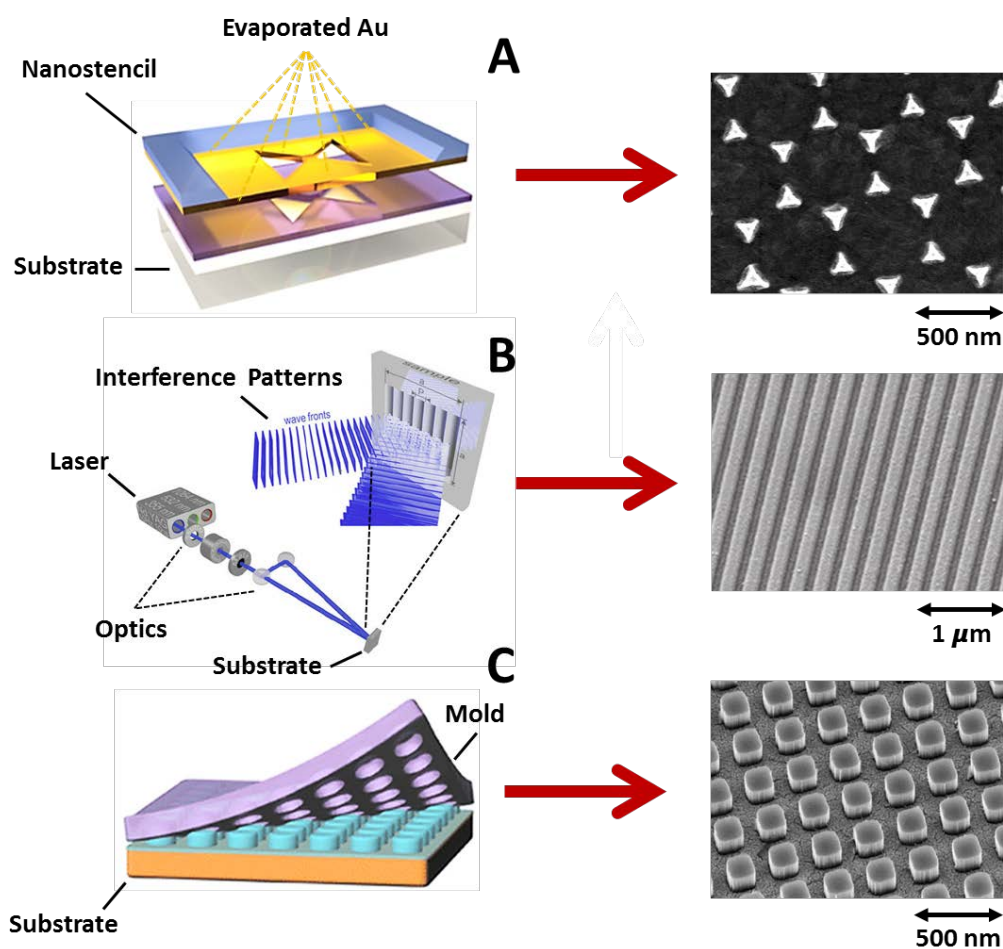

Figure 1.11 Some novel fabrication methods for scale production of nanoplasmonic substrates: (A) nanostencil lithography, (B) laser interference lithography and (C) nanoimprint lithography.

25

Some examples of recently fabricated plasmonic nanostructures using some of these processes are hybrid nanocavities[85], nanopillars[86], or nanoslits[87]. They show extremely high sensitivity performance (8066, 1010 and 926 nm RIU^{-1}, respectively, with Figures of Merit of 179, 108 and 252 RIU^{-1}) that even exceed the theoretically predicted upper limit for conventional SPR sensors, leading to wavelength shifts in some cases large enough to produce color differences noticeable by the naked eye for very small refractive index changes. Fully taking advantage of their potential will ultimately depend on the appropriate surface functionalization[88,89]. Although the number of examples applying nanoplasmonic biosensors for concrete bioanalytical applications is steadily increasing, advances in surface functionalization still shows slow progress. The main drawbacks that slow down the final goal of the widely use of biosensor devices outside the laboratory environment are: the achievement of fully integrated and self-operative device, with complete integration in a compact autonomous platform and technological transfer, with validated applications in real environments[35,44].

Integration and high throughput analysis are both essential requisites to succeed in developing relevant biosensor platforms. In nanoplasmonic biosensors the merger of multiplexed analysis with an all-integrated platform is scarcely reported. Microfluidics is in this sense an indispensable module to provide simultaneous analysis and assure low sample and reagent consumption[90]. Appropriate dimensions in microfluidic headers can enhance the diffusive mixing and as a consequence, the speed and accuracy of reactions. Performance improvements like reduced measurement times, improved sensitivity, higher selectivity and parallelism can be obtained with the integration of an appropriate microfluidic system[91].

In terms of reaching multiplexed measurements, the main progress in the last few years has been based on the use of imaging techniques, where a CMOS or CCD camera register the intensity distribution in a wide area for multiple sensing spots[92,93]. The intensity changes due to a biomolecular binding event are then detected with digital image processing algorithms. These imaging systems are, however, still limited in terms of sensitivity, as a result of the narrow wavelength response and the low quantum efficiency of conventional cameras[94]. A recent

example is a simultaneous multiplexed LSPR imaging system[95] (Figure 1.10A) with a high level of integration, low size and simple instrumentation, using gold nanoislands as sensors created by simple thermal annealing of gold films. The use of a wide emission spectrum white light-emitting diode (LED) and a camera detector allows analyzing a large area of collected images in their different chromatic components in a red-green-blue (RGB) space color. The portable palm-size setup incorporates a simple two-channel microfluidic module for real-time evaluations In fact, the authors were able to directly detect low molecular weight compounds (as tobramycin, MW=467 Da) using specific aptamers as bioreceptors, reaching a LOD of 0.5 µM (0.2 µg·mL^{-1}) in buffer. Filtered undiluted serum analysis was attempted at the expense of sacrificing the LOD. This platform is a good example, although it is still at a proof-of-concept stage and shows moderate sensitivities, of simple, cost-effective, integrated, nanoplasmonic based biosensor device.
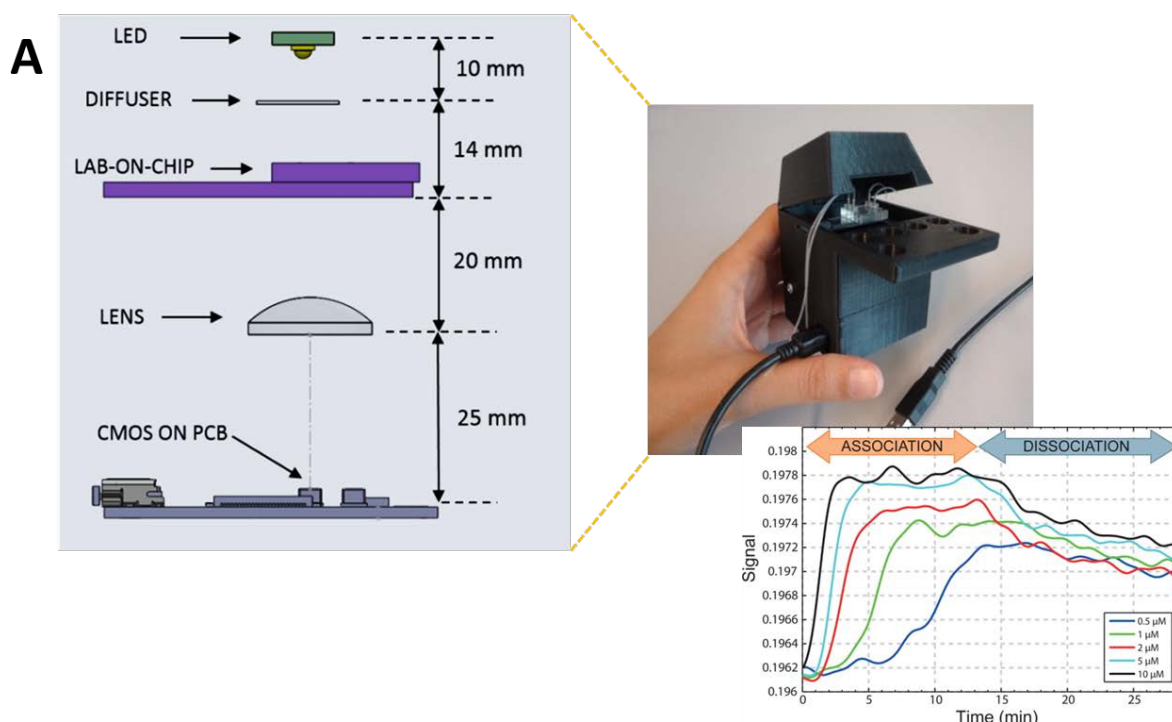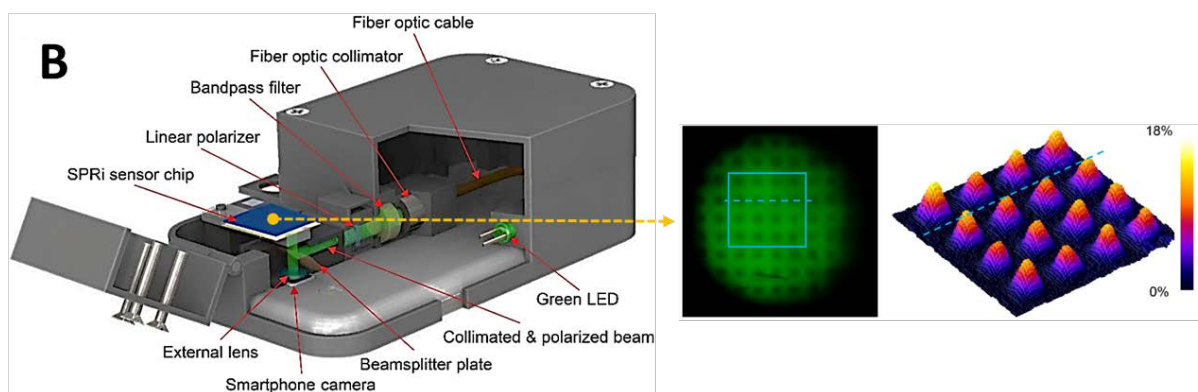
Figure 1.12 Examples of nanoplasmonic based integrated biosensor devices. (A) Picture of a complete custom made nanoplasmonic biosensor platform, including digital rendering of the components, their relative distances and dimensions, and a plot of the kinetics association and dissociation of tobramycin for the different concentrations tested. Reprinted with permission from[95] 2015 American Chemical Society. (B) Digital rendering of a complete smartphone-based nanoplasmonic biosensor platform, including the microarray imaging of sensing spots and a 3D representation of intensity difference image. Reprinted with permission from[97] 2017 Elsevier.

Finally, the migration of integrated versions of biosensor platforms to current smartphones, with their advanced imaging and communication capabilities, represents a powerful approach for the achievement of affordable LOC-based nanoplasmonic biosensors[96]. The high performance cameras, processing power, data acquisition and constant upgraded software of existing smartphones make them an attractive complement for multiplexed biosensor devices. Either auxiliary disposable or reusable modules, which incorporate optics, transducer and microfluidics where the biointeractions take place, can be coupled to the camera. Using custom acquisition software, the monitoring of signals can be extracted. Cellphone based technology has been recently applied for a silver nanoslits-based nanoplasmonic biosensor on the back of a smartphone[97] (Figure 1.10B), a green LED flash as light source and the camera to capture the images which are processed by a specifically developed application to obtain relative intensity. All the functionalities are integrated in the platform: flow cell, optics, illumination system, detection system and software. Based on the detection of mouse IgG using a microarray format as a proof-of-concept biosensing, the authors show that the system performance is comparable to a conventional SPR instrument achieving a

LOD near 4.1×10^{-5} RIU and demonstrating that this cost-effective, palm-size version can provide interesting features and represents an attractive and affordable alternative for many on-field applications.

In conclusion, nanoplasmonic biosensors are part of a wide research field with many unmet challenges necessary for the development of highly integrated and portable devices. Microfluidics that provide multiplexed capability, an adequate miniaturization and robustness, handling simplicity, reliability and competitive affordability are desirable requisites that should be included in the design, without negatively affecting the sensitivity and reproducibility standards required in clinical analysis. Nanoplasmonics biosensor technology can play a prominent role in this regard, since sensitivity levels and miniaturization are realistically achievable goals. The fabrication of novel structures that can offer enhanced performance is continuously evolving and in this regard, there is an increasing trend of using scalable fabrication methods that are compatible with the use of flexible materials like polymers as supporting substrates, which may reduce the final cost.

Biosensing feasibility seems to be leaving the proof-of-concept stage and a growing number of targets have already been detected in real samples which demonstrate the versatility of the technology[34,53]. However, there are pending challenges that still slow down the path towards commercialization, mainly related to the difficulties in the integration of all the components into a single portable platform. Moreover, there is still a long road ahead for this emerging technology to be fully adapted like conventional SPR, especially in the improvement of microfluidics and biosensing performance. Nevertheless, nanoplasmonic biosensors possess all the features necessary to become outstanding analytical tools.

Considering the challenges and the state-of-the-art in the development of Lab-on-a-chip nanoplasmonic biosensor platforms previously mentioned, in this doctoral thesis we focus on the development of a novel plasmonic biosensor based on industrially produced Blu-ray optical discs as a simple and cost-effective substrate containing nano-slits to generate the plasmon resonance phenomena[98,99] by coating them with different metallic layers on a nanometric scale. The final scope is to

integrate the sensors in a lab-on-a-chip (LOC) platform for the real-time and simultaneous detection of different biomarkers in human fluids.

To achieve the scope, it is first necessary to perform the computation of finite-difference time-domain (FDTD) optical simulations to analyze the plasmon resonance generation in the nanostructured substrates by coating them with different metallic layers on a nanometric scale and at different incident angles of light. It is also necessary to develop a fabrication scheme to obtain the plasmonic sensors using Blu-ray discs and to analyze their batch to batch reproducibility.

Once a simple and reproducible plasmonic sensor chip is achieved, it is necessary to develop and fabricate the microfluidic counterpart and the optical readout system to get a compact and high performance biosensing platform, and finally, to develop proof-of-concepts to evaluate the final performance as a biosensor.

Chapter 2. Simulation and Fabrication of Nanostructured Plasmonic sensors

This chapter includes first a theoretical analysis using FDTD simulations of the optical behavior of the Blu-ray disc-based plasmonic nanostructures modelling parameters as the thicknesses of the gold metallic layer and the incident angles under a reflectance detection scheme. Once the optimal designs were selected, the fabrication was developed and the sensor structurally evaluated. Finally, it is discussed the development, fabrication, and optimization of the microfluidics packing for the plasmonic sensor chip using two polymers: polydimethylsiloxane (PDMS) and cyclic olefin copolymer (COC).

2.1 Fundamentals of Plasmonics in optical discs

2.1.1 Plasmonics in Blu-ray discs

Optical discs like CDs, DVDs and Blu-ray discs (BD) are disk drives for digital information storage that uses laser light within the visible to near infrared (NIR) spectrum as part of the process of reading or writing data. For this process of reading/writing the system requires a semiconductor laser, a lens for focusing the laser beam, and photodiodes for detecting the light reflected from the disc's surface. The disc's surface if full of concentric tracks where the information is readed/writed, an optical disk recorder encodes (also known as burning) data onto the disc's surface by selectively heating parts of an organic dye layer with a laser. This heating process creates marks that can be read like the pits and lands on pressed discs.

The dimensions of the marks and tracks, and the wavelength of the reading/writing laser depend mainly in the type of optical disc: CD-type discs have a track pitch (separation between tracks/period) of 1.6 μm and require a 780 nm NIR laser, DVD-type discs have a track pitch of 740 nm and require a red laser (650 nm), finally Blu-ray discs have a track pitch of only 320 nm and require a violet laser (405 nm). As consequence of the dimensions of the track pitch, a Blu-ray disc can encode

a larger amount of information (up to 25 Gigabytes (GB)) compared to the other technologies (DVD up to 4.7 GB, and CD up to 700 Megabytes, respectively). Figure 2.1 shows a summary of the different conventional optical discs and some of their physical parameters.
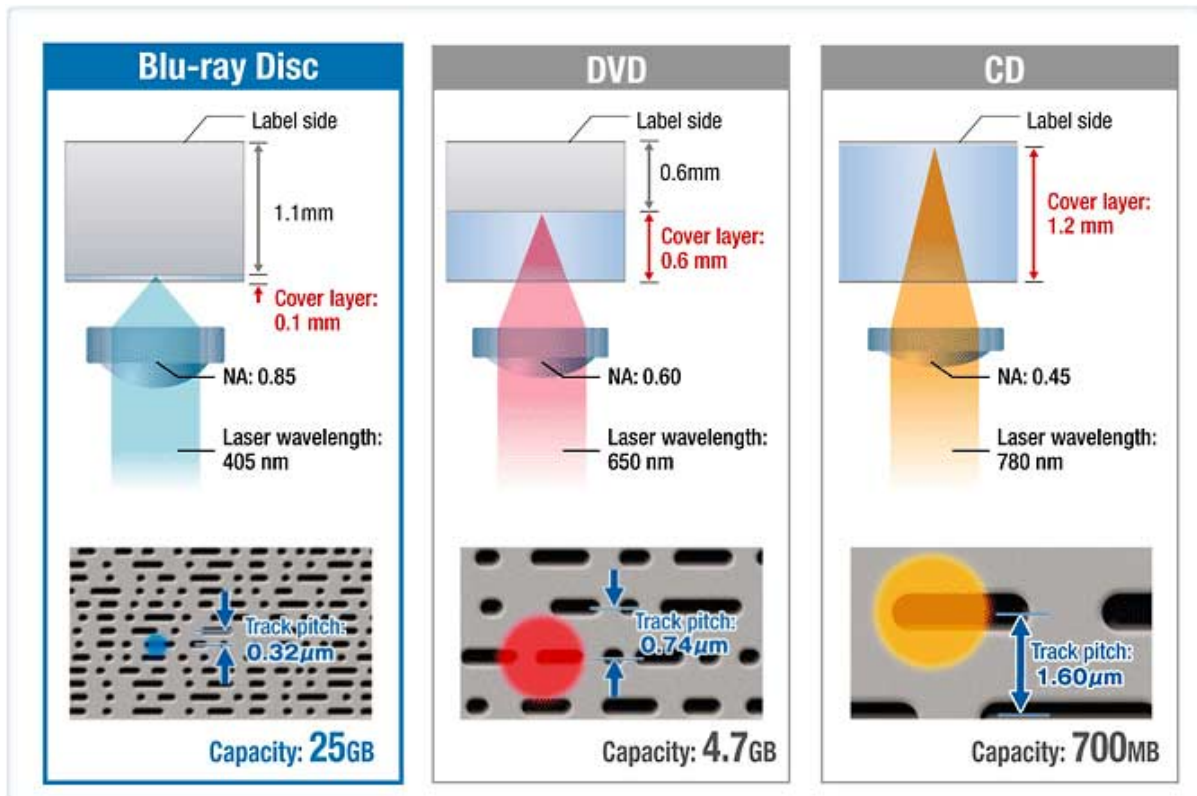
Figure 2.1 Schematic representation of the structure of different optical discs, including the optical and physical parameters for their operation as data storage devices.

From the above scheme and according to previous reports[99,100] it is clear that obtaining nanostructured substrates from BDs involves a simple fabrication process that only requires the removal of the thin protective layer (100 nm) to reveal the bare nanostructures, while for CDs and DVDs this procedure is more complex due to their sandwich design[97,98].

Commercially available optical discs are top-down fabricated by thermal nanoimprint, which is a fabrication process that creates nanopatterns by mechanical deformation of imprint resist and is a fabrication process with the potential for low cost and high throughput that it has been used for more than two decades[99,100]. The

fabrication of these micro and nanostructures implies the following process: The imprint polymer is heated above its glass transition temperature (~145 °C for polycarbonate) and then in the following imprint step, the stamp is pressed against the substrate at a given pressure for a specific time. The sample is cooled down below the glass transition temperature of the imprint polymer while the stamp is still in contact, then the mold is removed, and the imprinted pattern remains in the polymer layer.

Optical discs are fabricated of polycarbonate and they offer a highly patterned area (recording area) of ~100 cm^2. In particular, polycarbonate offers highly attractive properties as substrate for optical applications: polycarbonate is a durable material with high transparency in the visible region of light and possess a high glass transition temperature (~145 °C)[101]. Other advantages of polycarbonate are its high impact resistance, low moisture absorption, good machining properties, low cost, and good chemical resistance to several substances and biocompatibility[102]. However, the main advantage of polycarbonate is that due to its chemical composition it is possible to deposit on top thin metallic films without the need of adhesion layers,[103] which simplifies the fabrication process for a plasmonic sensor and might contribute to improve the final performance of the device[104].

Figure 2.2A shows a comparison of the dimensions of the micro and nano slits present in different unrecorded optical discs and Figure 2.2B shows a scheme of the physical structure of a commercial BD.
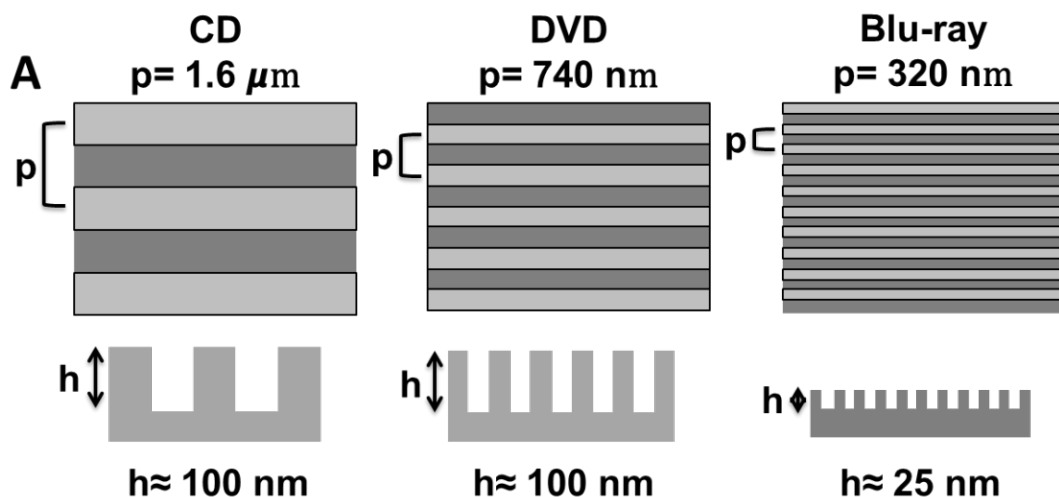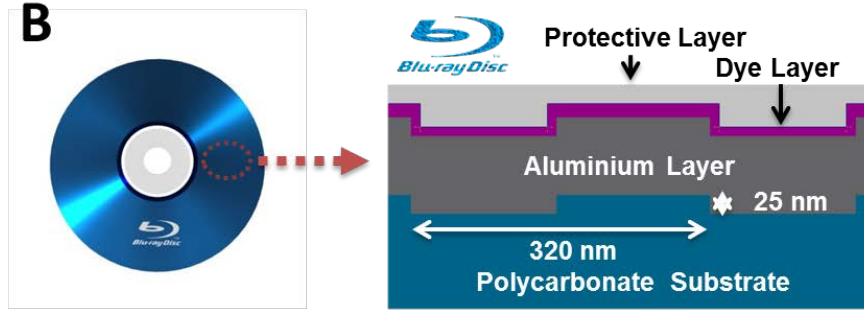
Figure 2.2 (A) Comparison of various characteristics of a recorded Compact Disc, Digital Versatile Disc, and Blu-ray Disc. Dimensions indicated are the period (p) and height (h). (B) Schematic representation of the structure of a Blu-ray optical disc.

As discussed above, plasmonic sensors based on grating couplers have been used in a lesser extent compared to the ones using prism couplers; however, gratings can be fabricated by high-throughput techniques into plastic substrates and, as a direct consequence, provide easy to fabricate and low-cost plasmonic sensors. The high order periodic structures present in BDs and the other optical discs behave like diffraction gratings (a "rainbow" of diffracted light appears when an optical disc is exposed to a broadband light) [105,106] allowing the possibility to use them as couplers to generate plasmonic effect when they are coated with a thin metallic layer[97,98].

For the generation of plasmons in grating couplers coated with a thin metallic film, the light is diffracted parallel to the interface by the grating allowing the matching between the wavevector of the diffracted light and that of the plasmonic effect in the thin metallic layer. The plasmonic effect by the grating coupling method can be described by the Bloch wave surface plasmon resonance (BW-SPR), when the Bragg condition for one-dimensional periodic metallic structure is satisfied[107]. Under oblique-angle incident light, it can be described by the following equation[107]:

$$\lambda_{SPR}(n, i, \theta) = \frac{P}{i}\left\{Re\left[\left(\frac{\varepsilon_m n^2}{\varepsilon_m + n^2}\right)^{1/2}\right] \pm \sin\theta\right\} \qquad (2.1)$$

where i is the resonant order, P is the period of the nanostructure, ε_m is the dielectric constant of the metal, n is the environmental refractive index and θ is the incident angle, respectively.

From this expression, a red-shift in the resonant wavelength is expected when the RI of the medium near the gold surface increases and with long nanostructure periods (i.e. for a plasmonic sensor based on DVD discs with a period of 740 nm it is expected a plasmonic band closer to the IR ≈900 nm, while for a plasmonic sensor based on BD with a period of 320 nm it is expected a plasmonic band in the VIS ≈600 nm). Also, for a fixed nanostructure period, the resonance wavelength can be either controlled by the metal coating employed (varying their thickness and material) or by the light incident angle.

2.1.2 Finite-Difference Time-Domain optical simulations

In order to model the plasmonic effect in the BD-based metallic nanostructures, three-dimensional FDTD simulations were performed to calculate the reflectivity of a TM polarized broadband light source in the visible range (400 to 800 nm) impinging the nanostructured substrate with different thickness to the metallic layer, for a fixed incident angle. The FDTD simulations were performed using commercial software (Lumerical Inc., FDTD solution, Canada).

The 3D model of the BD-based metallic nanostructures consisted of polycarbonate substrate (n= 1.58) with nanoslits in the surface with the same structural parameters to those present on the BD (i.e. a slit period of 320 nm, slit width of 160 nm and a height of 25 nm). 50, 75, 100 and 125 nm gold thickness layers were simulated on top of the polycarbonate substrate. These gold layer thicknesses were selected to evaluate the evolution in the sharpness of the plasmonic peak according to previous reports[97,98]. The optical constants of the polycarbonate and gold were taken from Sultanova[108] et al. (2009) and Johnson and Christy[109] (1972), respectively, in the range from 400 to 800 nm. To consider a semi-infinite diffraction grating, periodic boundary conditions were used in the x and y axis,

and a perfect matched layers (PML, an artificial absorbing layer for wave equations) approach was used in the z axis to reduce the finite-thickness "transition" reflection.

A schematic representation of the simulation geometry can be observed in Figure 2.3. The plane wave light source had an oblique light incident angle θ ranging from 30 to 70⁰; this range was selected due to optical limitations of the proposed experimental set-up. From the Lumerical® software interface, two monitors were simulated: a "Field profile" and a "Field and power monitor". The Field profile monitor was placed in the z direction (cross-section) to evaluate the electric field distribution of the plasmonic nanostructure, while the Field and power monitor was placed in the x-y direction to evaluate their reflectance spectra. A simulation region with 320 nm in x and y plane, and 200 nm in z was used to perform the simulation with a uniform mesh size of 2 nm in all axis to reduce computational requirements. H_2O was selected as the external medium (n=1.33) for the simulations.
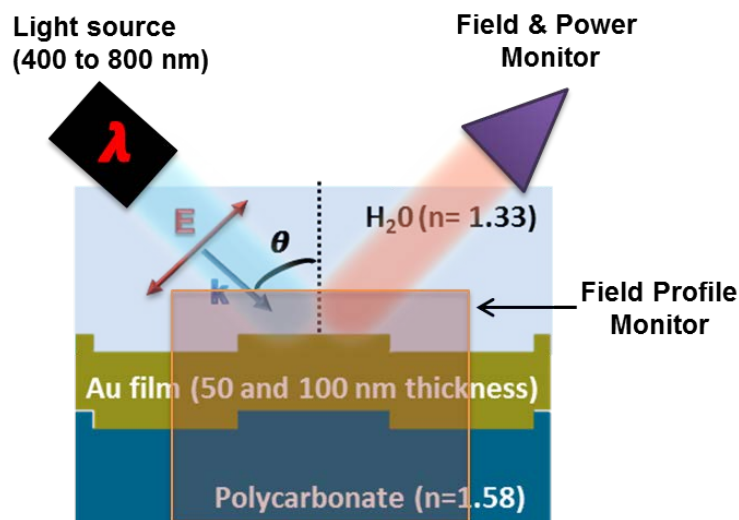
Figure 2.3 Schematic representation of the structural and optical parameters for the FDTD reflectance simulations of the BD-based metallic nanostructures.

The reflectance spectra obtained by FDTD simulations with the 50, 75, 100 and 125 nm gold metal layer thickness, respectively are shown in Figure 2.4A at a fixed incident angle of 50⁰; as can be observed there are no significant differences for a gold layer thicknesses above 100 nm. It is observed an increase in the sharpness of the peak from the 50 to 100 nm range. These lose in sharpness of the

plasmonic band for gold layer thickness below 100 nm can be correlated to a strong interaction of plasmonic waves with the polycarbonate substrate[97,107]. To confirm this possibility, we evaluate the optical filed distribution in a cross section of the nanostructure with a 50 and 100 nm gold layer thickness.
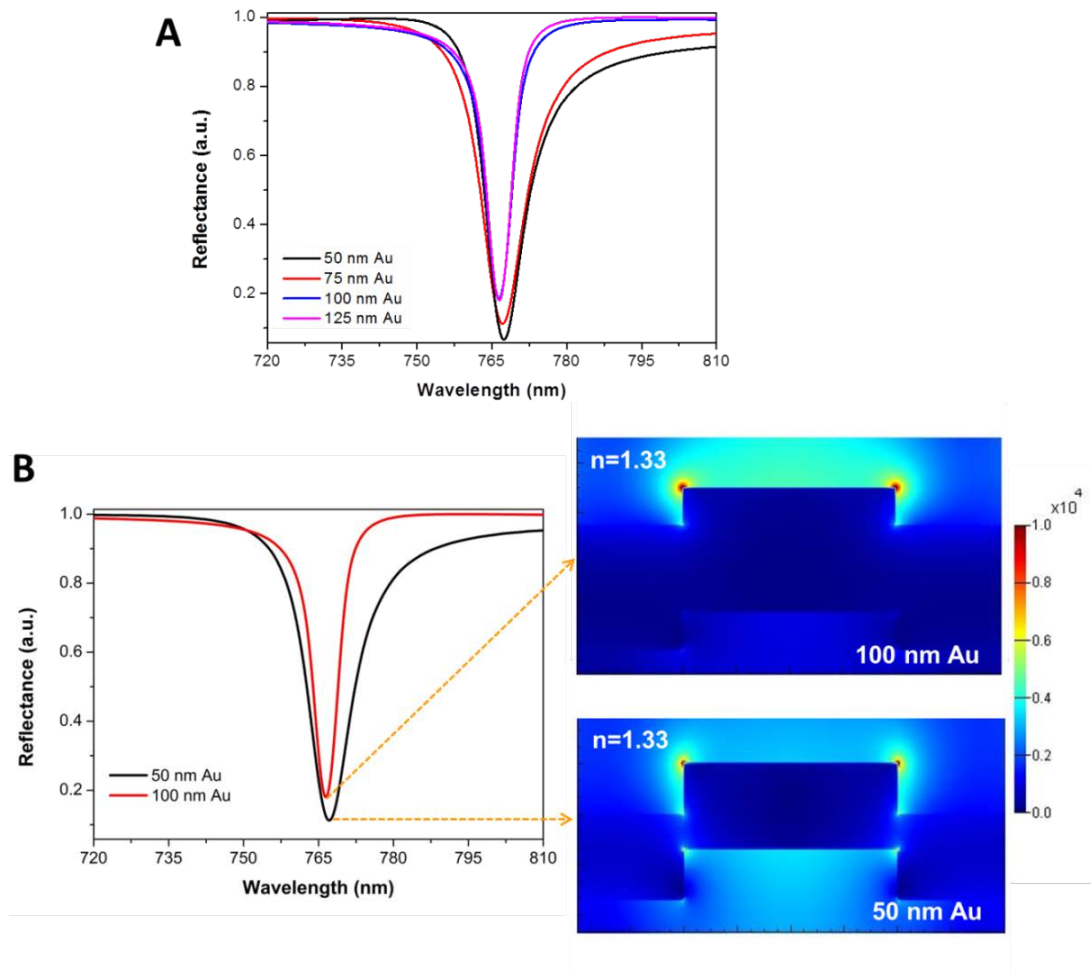
Figure 2.4 FDTD Simulations of the proposed BD-based metallic nanostructures. (A) The simulated optical reflectance spectra for the 50, 75, 100 and 125 nm gold film layers evaluated. (B) Relation between the reflectance spectra (left) and the simulated electric field distribution (right) for the two gold thickness layer evaluated.

By analyzing the optical field distributions calculated from FDTD simulations at the peak resonance wavelength (see Figure 2.4B.), we observed that there are significant differences in the electric field distributions for a gold thickness layer of 50 and 100 nm, respectively. A high interaction of plasmons with the underlying

substrate for the 50 nm gold layer can be observed, which not only decreases the intensity of the optical fields, but also decreases the decay length (the plasmon propagation length) to the sensing media. In contrast, for the 100 nm gold layer there is a significant decrease in the interaction of plasmons with the underlying substrate, which increases the intensity of the optical fields with longer decay lengths as compared with the 50 nm gold layer.

The FDTD simulations of the reflectance spectra varying the light incident angle from 30 to 70⁰ under TM-polarization for a 50 nm gold thickness layer are presented in Figure 2.5. A red-shift in the resonant wavelength with the increase of the light incident angle can be observed. This increase is in agreement with the equation that describes the plasmonic effect by the grating coupling method previously described. Additionally, a decrease in the FWHM is evident with a narrowing of the plasmonic band as the light incident angle increases.
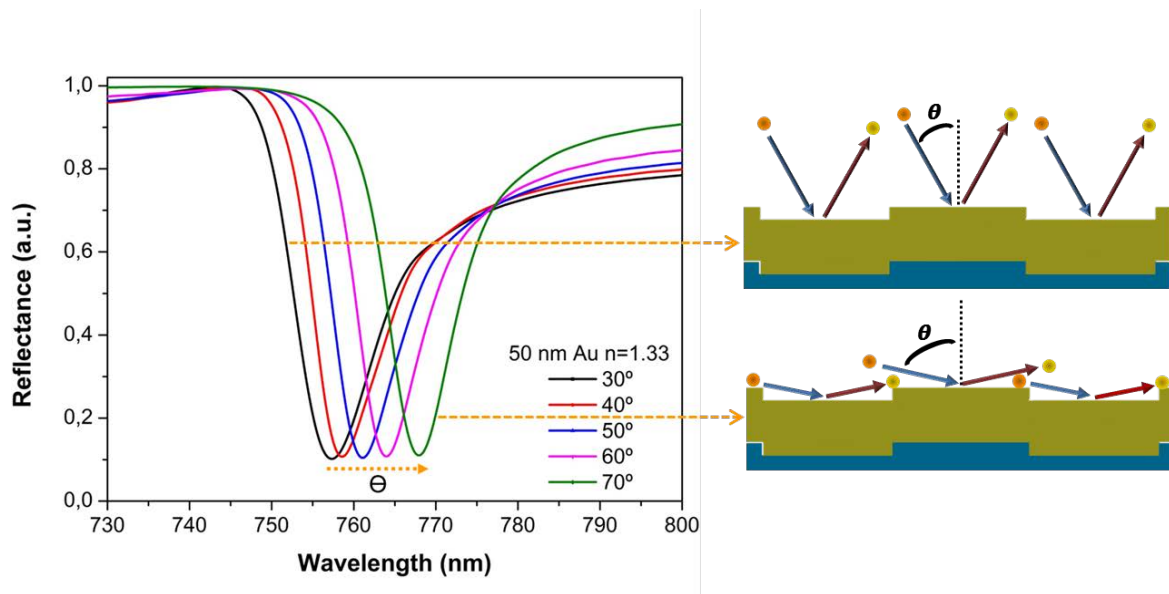
Figure 2.5 FDTD Simulations of the BD-based nanostructures with a 50 nm gold layer at different light incident angles. The simulated optical reflectance spectra under TM-polarization with a light incident angle ranging from 30 to 70⁰ (Left). Schematic representation of the variation on trapping/confinement of light with the increase in the light incident angle (right).

This effect can be correlated with the increase of the light's trapping/confinement in the plane of the array with the increase of the light incident

angle: as the light incident angle increases the photons that are scattered from one nanostructure can be collected by the neighboring nanostructures increasing the energy transfer to the metallic nanostructure instead of decaying as free-space light[110]. According to Zhou and Odom[110] (2011), the interaction between the Bloch wave surface plasmon resonance (BW-SPR) that describes the plasmonic effect by the grating coupling method and the subradiant plasmons from these confined photons at high incident angles produces narrower resonant linewidths[107,110].

2.2 Fabrication process

As previously mentioned, obtaining plasmonic sensor chips from BDs involves a simple fabrication process (See Figure 2.6); all the fabrication process starting from a recordable BD can take around 3hr, based on the coating of a metallic layer on the bare nanostructured polycarbonate substrate. First, single layer recordable BDs (TDK, T78088, Japan) were used after removal of their protective and reflective films (see Figure 2.7). The BDs were cut with a conventional computer numerical control (CNC) router (LPKF Laser & Electronics, Protomat C100/HF, Germany) to obtain individual chips (size of 1cm x 1 cm) in a concentric plane to the BDs; this process can take around 30 min per disc. In order to remove the protective and reflective layers, the chips were immersed in a hydrochloric acid solution (1 M HCl) for 120 min. Finally, the chips were cleaned by sonicating them in MilliQ water and ethanol for 1 min, and air dried.
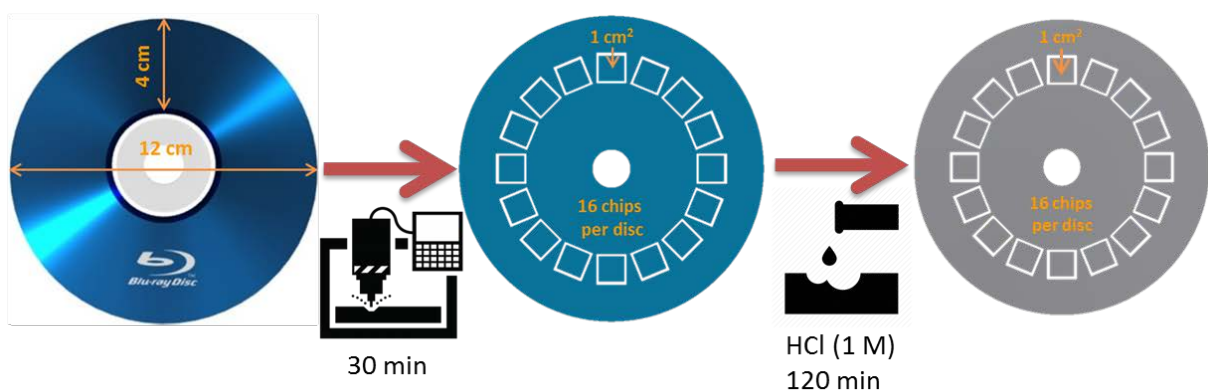
Figure 2.6 Schematics depiction of the steps for obtaining BD-based substrates. The steps can be summarized as follows: CNC cut for chip individualization and acid etching to remove the protective and reflective layers.

To evaluate the surface roughness and morphology of the bare chips, the BD-based nanostructured substrates were structurally characterized by atomic force microscopy (AFM) and scanning electron microscopy (SEM). The surface roughness and morphology of the bare chips was characterized using an AFM (Digital Instruments Inc., MM-AFM2, USA). The samples were scanned over a 2.25 µm^2 at a tip velocity of 1 µm/min at contact mode (see Figure 2.7A).

Morphological dimensions of 25 nm in height and 320 nm in period were obtained by AFM; these values are similar to those obtained in previous reports[97,98]. Additionally, a surface roughness value of only 0.21 nm (in root-mean-square (RMS)) was obtained minimizing the possibility of plasmon losses by light scattering. SEM images were obtained by coating the substrate with a 50 nm platinum film by sputtering and using a field emission scanning electron microscope (FEI Co., Quanta 650, USA) with a high voltage of 5 kV to decrease damage to the samples (see Figure 2.7B). The SEM image shows a high uniformity in the structure, array and dimensions in an extensive region of the chip. These results demonstrate that the fabrication process does not alter the morphological characteristics of the nanostructured substrate.

B
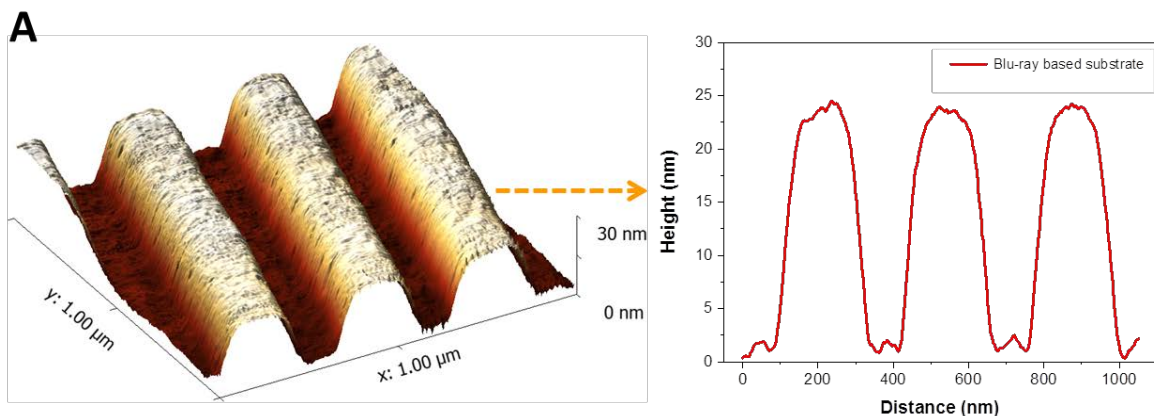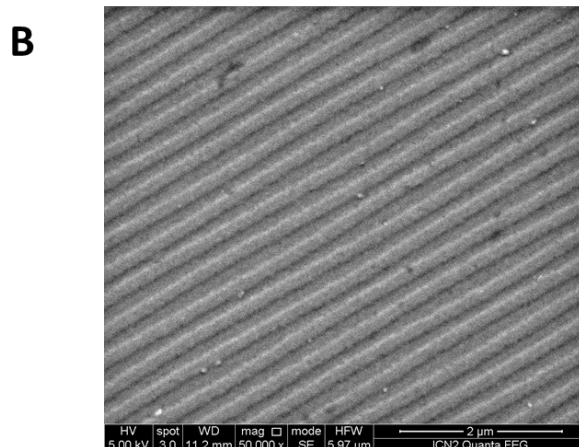
Figure 2.7 Structural characterization of the BD-based substrates. (A) AFM image (left) and profile (right) of a blank bared Blu-ray disc-based substrate. (B) SEM image of the surface.

After the chips were cleaned, gold layers of up to 100 nm thickness were deposited by an electron beam deposition system (AJA International Inc., ATC-8E Orion, USA) with a high voltage of 8kV, a chamber vacuum pressure of 1×10^{-7} Torr and a beam current of 90 mA to achieve a deposition rate around 1 Å/s. As mentioned before, no adhesion layer was required. To evaluate the adhesion of the gold film layer to the BD-based nanostructured polycarbonate substrate we performed a Scotch tape peel test[112]; this test has been previously reported in the literature to evaluate the adhesion of gold thin films[17] and gold nanostructures[18] to different substrates.

The test consists of using a strip from a conventional roll of a cellophane-baked tape that is pressed firmly onto the film to be tested. Briskly lifting the tape applies a force and removal of the film by the tape indicates that the adhesion strength of the film is poor or limited. The test was implemented using a conventional office pressure-sensitive tape and in general, no removal of the gold films was observed, independently of the gold layer thicknesses (50 and 100 nm).

2.3 Polymer microfluidic integration

2.3.1 Microfluidic design

41

Microfluidics can reduce measurement times, improve sensitivity and parallelism with low sample and reagent consumption; being an indispensable module for the development of biosensor platforms. When appropriate dimensions in microfluidics are selected, there is an enhancement of the diffusive mixing and, as a consequence, an enhancement in the speed and accuracy of reactions. However, one of the main challenges to achieve integrated sensors including microfluidics is the bonding between the sensor chip and the microfluidic chamber, mainly because of the limited compatibility between materials and, in some cases, the need to perform chemical surface modifications to bond them[112-113]. This surface modification might interfere with the sensing assay and, in general, is not reversible.

In an attempt to overcome these difficulties, we used double-sided adhesive tape as a simple, inexpensive and versatile strategy to fabricate microfluidic channels and thereby simplify the bonding for a rapid prototyping of the plasmonic biosensors[114]. The use of double-sided adhesive tapes simplifies the overall fabrication process by eliminating several conventional microfabrication steps such as photolithography, chemical etching and bonding (Figure 2.8)[114].
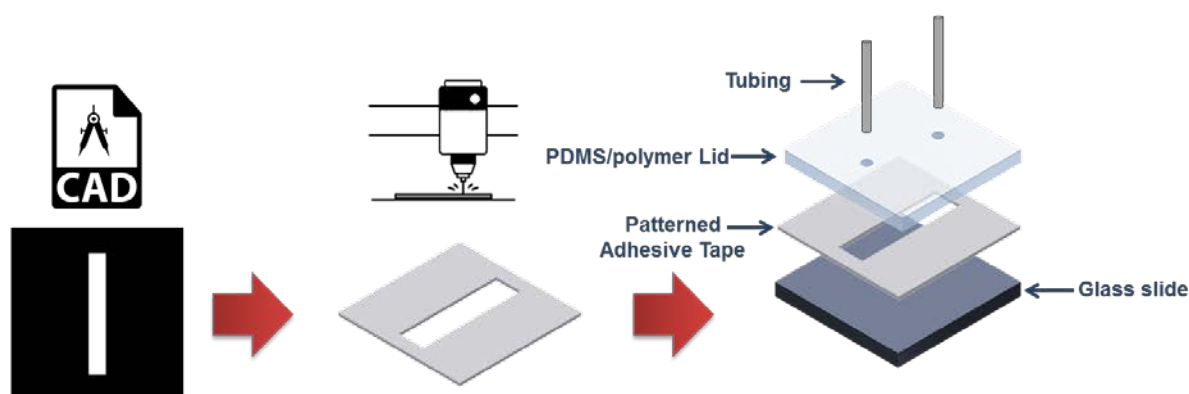
Figure 2.8 Schematic representation of the fabrication of microfluidic headers using CNC/cutting plotter patterned adhesive tape.

The microfluidic reaction chamber for the plasmonic biosensor was developed under the following design considerations: a small-volume (around 900 nL) for low sample and reagent consumption, a short path length (6 mm) and height (75 µm) to localize the target detection to the surface of the sensing area, and finally,

geometrical dimensions that fulfill laminar flow according to the governing principle around microfluidic sample management i.e. the Reynolds number (*Re*). It defines the ratio of inertial versus viscous force during flow and it can be expressed as[116,117].

$$Re = \frac{QD_h}{Av} \qquad (3.1)$$

where *Q* is the volumetric flow rate, *v* the kinematic viscosity of the fluid, *A* the cross sectional area of the microfluidic channel and D_h the hydraulic diameter, which is also correlated directly with the geometry of the microfluidic channel. The last equation can be solved to determinate *Q* to fulfill laminar flow, according to the theory for laminar flow *Re* < 1000.

Considering a rectangular channel with height of 75 µm (thickness of the selected commercial double-sided adhesive tapes for microfluidics), a channel width of 1 mm, a flow rate up to 100 µL/min, and water as the fluid carrier, we obtain a Reynolds number of ≈ 5. The maximum flow rate, up to 200 µL/min was selected considering that in plasmonic biosensing the detection online of a target is commonly done at a flow rate around 10 to 30 µL/min and in some other steps like regeneration or blocking this rate can be up to 100 µL/min[118,119].

2.3.2 PDMS and COC packaging

The microfluidic chamber of the plasmonic sensor chips was developed using two main components: a commercial double-sided adhesive tape sheet and a polymer cover. As commented before, a commercial 75 µm height double-sided adhesive tape for microfluidic devices (Microfluidic Chip Shop, GmbH., MCS-foil-008, Germany) was patterned with the microfluidic channel using a cutting plotter (Graphtec America, Inc., CE6000-40,USA). This approach is a fast, simple and highly reproducible bonding strategy without any surface pretreatment[120,121] between the plasmonic sensor chip and the flow chamber. The patterned design was developed in a CAD interface (Graphtec America, Inc., Graphtec Studio, USA) and then transferred to the cutting plotter as a vector image to be cut in the adhesive foil. Figure 2.9 depicts the software interface to cut a vector image of the microfluidic

channel to the adhesive tape. Each material to be cut had different heights and hardnesses and consequently, the speed, acceleration and blade force has to be optimized to achieve smooth cuts. These parameters were fixed by different evaluation tests and varied according to the spatial resolution of the microfluidic channels.
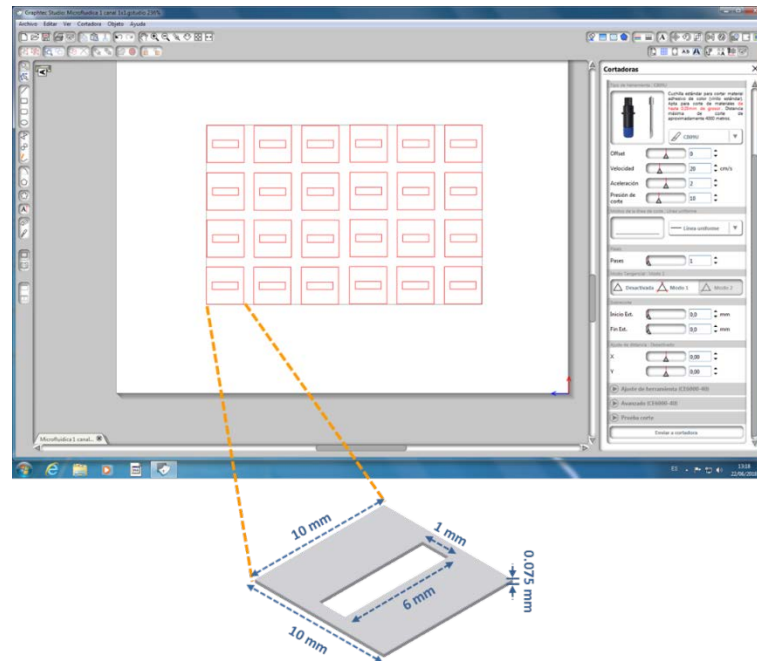
Figure 2.9 Software interface to cut a CAD designed microfluidic channel using a vector image in Graphtec Studio (Graphtec America, Inc., USA).

To build the lid that includes the connection ports for tubings, two well-known polymers in microfluidics were evaluated: PDMS and COC. PDMS is an attractive material for microfluidics due to its high transparency in the visible range of light, high biocompatibility, high chemical resistance and deformability providing a simple fluidic connection[123]. Also PDMS is sufficiently versatile to fit their dimensions by modifying the mold (length and width) or the resin volume employed (thickness) during the fabrication.

To fabricate the PDMS lid, the curing agent and the prepolymer (DOW Corning Co., Sylgard 184, USA) were thoroughly mixed in a volume ratio of 1:10

respectively, followed by degassing the mixture for 20 min. The degassed PDMS mixture was gently poured into a custom polycarbonate mold with the desired dimensions of the lid (height: 1 mm, width and length: 10mm). Then, the PDMS was heat cured at 80º C for 120 min on a hot-plate (KW-4AH, Chemat Technology Inc, USA). The cured PDMS was then removed from the mold and punched with a biopsy punch to generate the tubing connection holes. Finally, all the parts were bonded and the Teflon tubings connected (Adtech, HW30, England). Figure 2.10 depicts the fabrication steps for the packing of the plasmonic sensor using a PDMS lid.
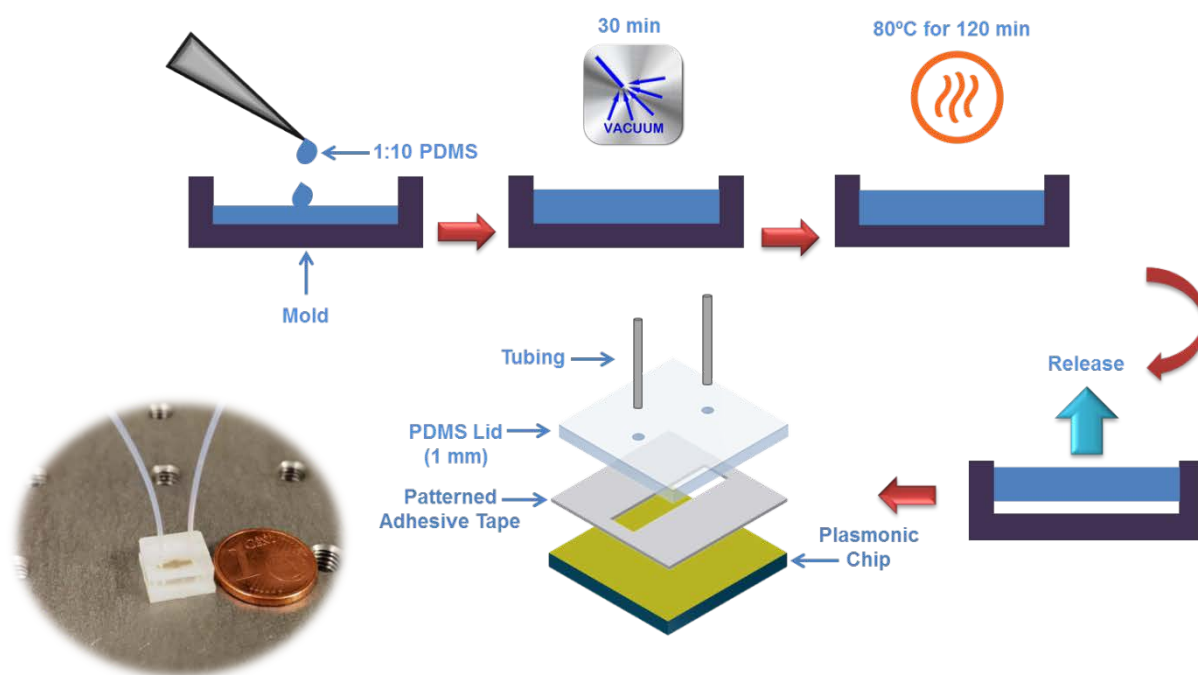
Figure 2.10 Steps for the fabrication process of the PDMS lid and photography of the PDMS lid based packing of the plasmonic sensor chip.

On the other hand, COC is a class of polymer with interesting properties as its superior optical transmission, biocompatibility and high chemical resistance. This class of material also has a low moisture absorption rate, a high water barrier and heat resistance [123,124]. Additionally, it possesses a higher surface energy compared to PDMS which can influence the bonding strength of the packed sensor. Individual COC lids (1 cm^2 and 1mm thickness) were obtained (see Figure 2.11) by cutting a COC foil (Microfluidic Chip Shop, GmbH., Zeonor 10-0710-0657-1.0-02, Germany) with a conventional computer numerical control (CNC) router (LPKF Laser &

Electronics, Protomat C100/HF, Germany). Then, Teflon tubings were connected and bonded to the lid using cyanoacrylate instant adhesive (Henkel AG & Co., Loctite 414, Germany).
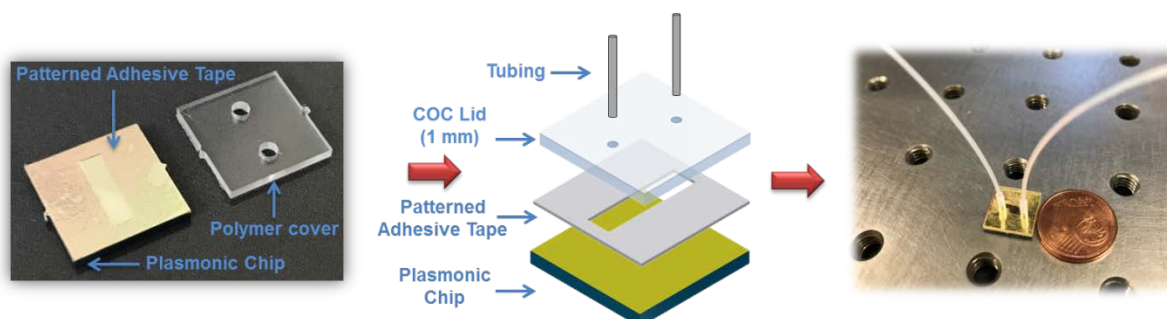
Figure 2.11 Steps for the packing process using a COC lid and photography of the COC lid based packing of the plasmonic sensor.

The performance of the PDMS and COC bonding to the plasmonic sensor was evaluated using a simple microfluidic circuit: by flowing PBS buffer over the packed chips using a syringe pump (New Era, NE-1000, USA) and gradually increasing the flow rate up to 100 µL/min to observe the presence of leaks. Three packed sensors with each of the packing strategies were evaluated. Lateral fluid leaks were observed for the PDMS packing at flow rates around 70 µL/min; meanwhile, COC packing was able to achieve flow rates above 100 µL/min without any leaks. According to these results, the COC packing strategy was selected due to its simplicity and superior bonding strength compared with PDMS.

Finally, Figure 2.12 summarizes the simple fabrication and packing steps to develop plasmonic biosensors with the proposed BD-based nanostructures.
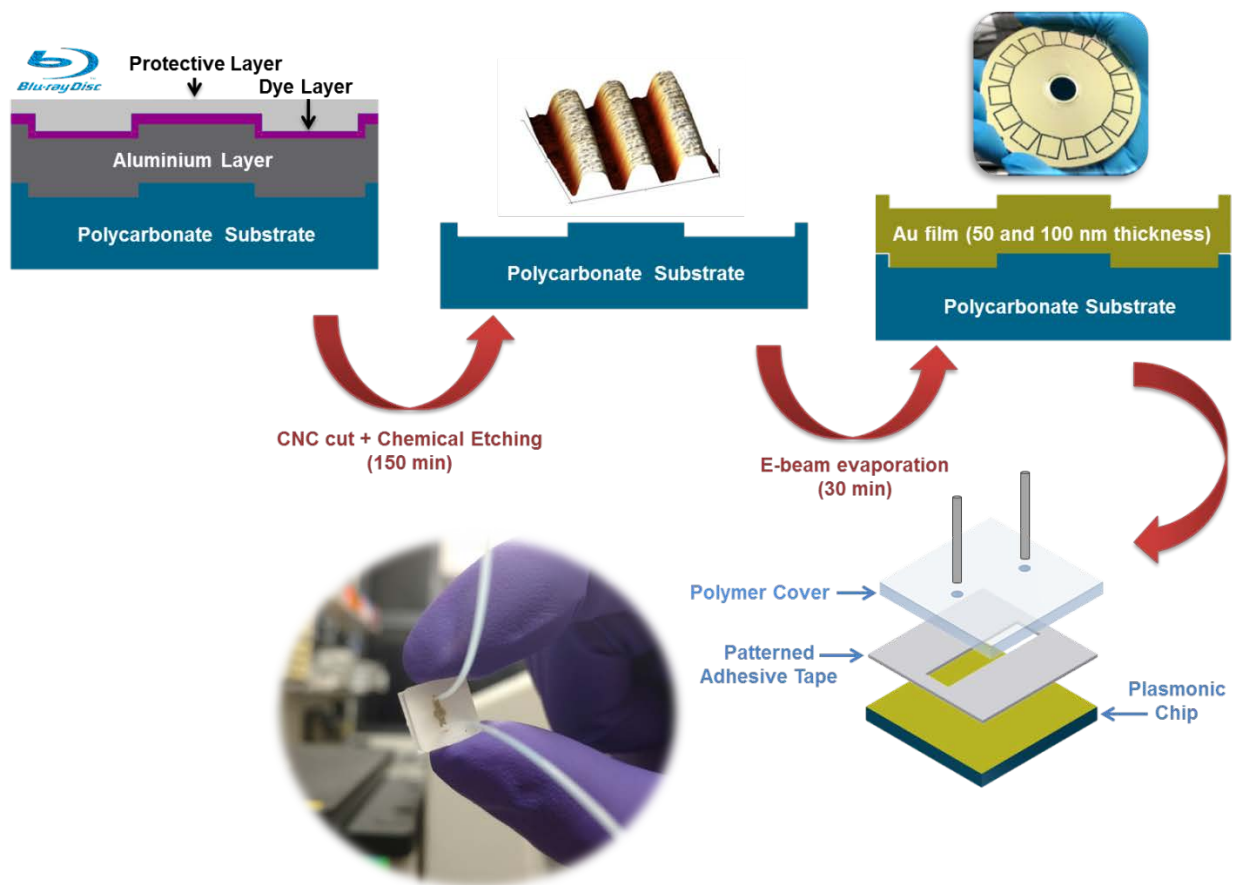
Figure 2.12 Scheme summarizing the main steps of the fabrication and packing process of the proposed plasmonic sensor based on commercial BDs.

Chapter 3. Biosensing Characterization of Nanostructured Plasmonic Biosensors

This chapter discusses the biosensing characterization of the proposed BDs based plasmonic sensor. First, we describe the two experimental set-ups for the optical characterization: one with a variable light incidence angle and one with a fixed light incidence angle. This is followed by the optical and sensing characterization of the plasmonic sensors at different light incident angles (30 to 70⁰). Once the light incident angle with the highest sensing performance was selected, the experimental set-up was characterized to determine their noise level and the limit of detection (LOD) was calculated. Finally, we evaluated the batch to batch reproducibility of the sensor and we evaluated the biosensing capability of the new nanostructured plasmonic sensors.

3.1 Optical characterization

3.1.1 Variable angle reflectance set up

According to the FDTD simulations presented in Chapter 2, a variable angle (30 to 70⁰) reflectance experimental set-up was devised for laboratory use. A scheme and a front-view photograph of the proposed set-up are shown in Figure 3.1.

For the experimental set-up, a custom platform was developed. On this platform, the set of an optical rail, a dual axis linear stage and a rotational stage provide 4 degrees of freedom system for sensor´s movement (xyz and θ). A set of two arms include the optical paths for collimation and collection of the light with a variable angle incident light. The combination of all optical components mounted on the left arm assures the excitation of the TM plasmonic mode with a collimated broadband light source. To this end, the halogen light source (wavelength region between 360 to 2400 nm and approximately 9 mW output, HL-2000-HP Ocean Optics, US) is fiber-coupled to a multi-mode fiber with a small core (Thorlabs, Ø200 µm and 0.22 NA M92L01, Germany) to decrease the size of the resulting light spot

and subsequently collimated with a fiber collimator (Thorlabs, F220SMA-B, Germany) mounted inside a cage. Finally, the collimated light beam is polarized (TM) with a VIS polarizer (Thorlabs, LPVIS050, Germany). The reflected light is collected by a fiber collimator (Thorlabs, F230SMA-B, Germany), that is attached to a cage. Booth arms are mounted in manual rotation stages with a 2º resolution (Thorlabs, RP01, Germany) to fix the incidence and collection angles. Spectral analysis is carried out with a compact Charge-Coupled Device (CCD) spectrometer with a spectral resolution of 0.5 nm and spectral range from 500 to 900 nm (Ocean Optics, Flame-T spectrometer, USA). Once the signal acquisition is optimized, all manually adjustable components can be blocked to increase the robustness of the measurements, and to avoid problems related to misalignment.
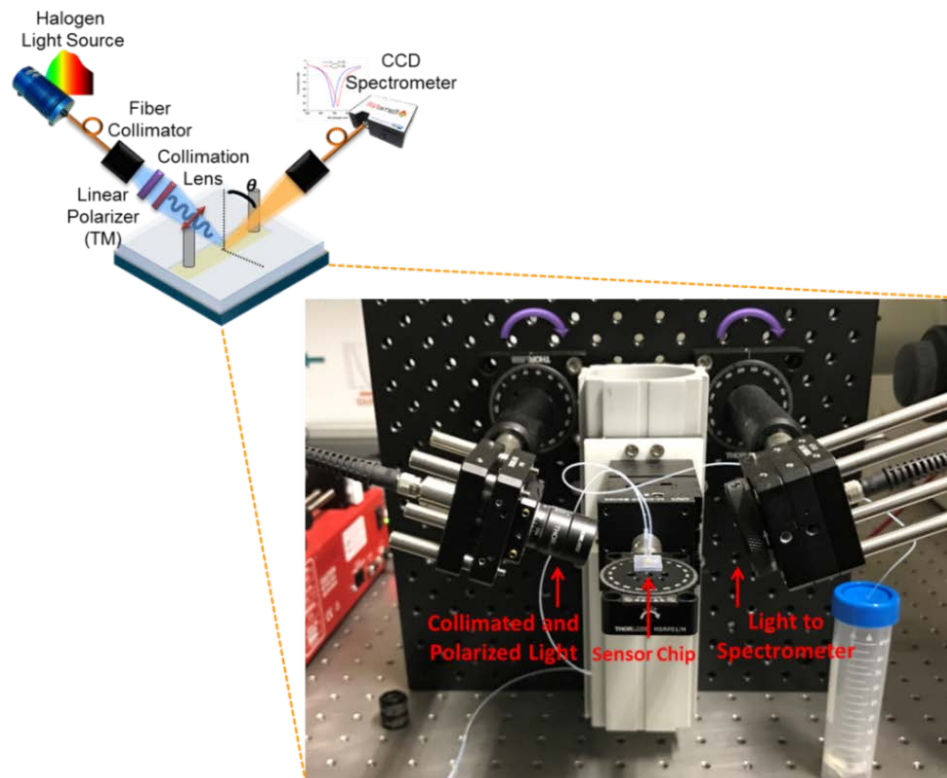
Figure 3.1 Schematic representation of the variable angle set-up for the optical characterization. The insert shows a front-view photograph of the experimental system.

The optical characterization of the plasmonic biosensor was performed under reflectance measurements. Reflection spectra were collected in air (n=1.00) and water (n=1.33). Figure 3.2 shows the reflectance spectra for 50 nm (A) and 100 nm

(B) gold thicknesses. A shift of λ_{SPR} to higher wavelengths up to 120 nm is observed as the incidence angle increases in good agreement with the equation 2.1 that describes the plasmonic effect by the grating coupling method and in agreement with the FDTD simulations. Also, in both cases narrower resonant linewidths (FWHM up to 15 nm for the 50 nm Au layer and 12 nm for the 100 nm Au layer at 70º reflectance angle) are observed, with an evident decrease in the FWHM. This last, in good agreement with the FDTD simulations and with the increase of the light trapping/confinement in the metallic nanostructures with high incident angles of light in periodic nanostructures proposed by Zhou and Odom[110] (2011). As can be observed in Figure 3.2C, there is a good agreement between the simulated and the experimental reflectance spectra, with a narrower resonant linewidth for 100 nm gold thickness film (FWHM up to 8 nm simulated and 12 nm experimental) compared with the 50 nm gold film (FWHM up to 10 nm simulated and 15 nm experimental).
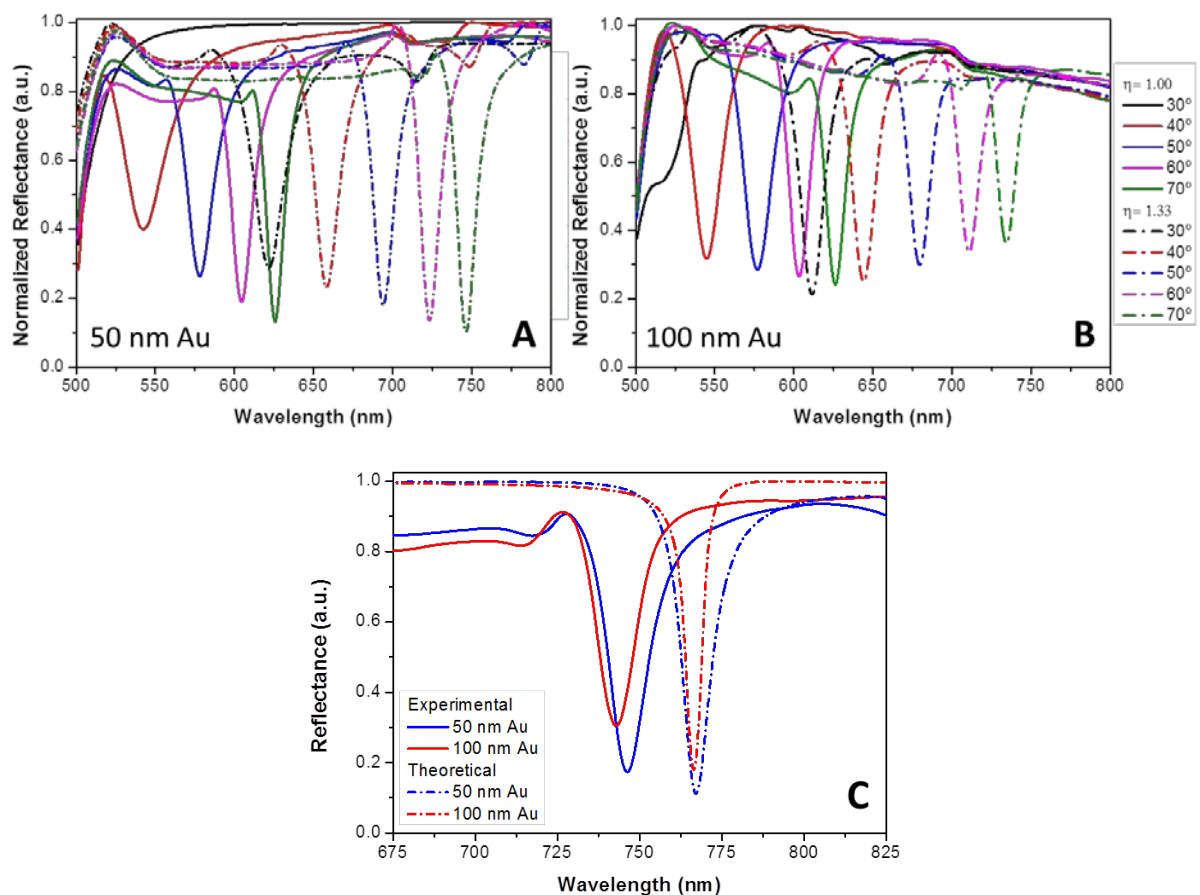
Figure 3.2 Optical Characterization of the plasmonic chips. Variation of the reflectance spectra in air (n=1.00) and water (n=1.33) with 50 nm (A) and 100 nm (B) gold layer

thickness varying the oblique light incidence angle. (C) Evaluated and simulated optical reflectance spectra under TM-polarization with a light incident angle of 70⁰ for the two plasmonic sensors in water (n=1.33).

3.1.2 Sensing performance varying the incidence angle

The effect of the angle of the incident light and the thickness of the metal layer on the sensing performance of the sensors was studied by evaluating aqueous solutions with different RI. The solutions were injected using a microfluidic system consisting of a syringe pump (New Era, NE-1000, USA), with adjustable pumping speed guaranteeing a constant liquid flow, and a manually operated injection valve (Valco Instruments Co. Inc., Cheminert C22-3186, USA). Figure 3.3 shows a schematic representation of the experimental set-up including the graphical of the custom made software employed.
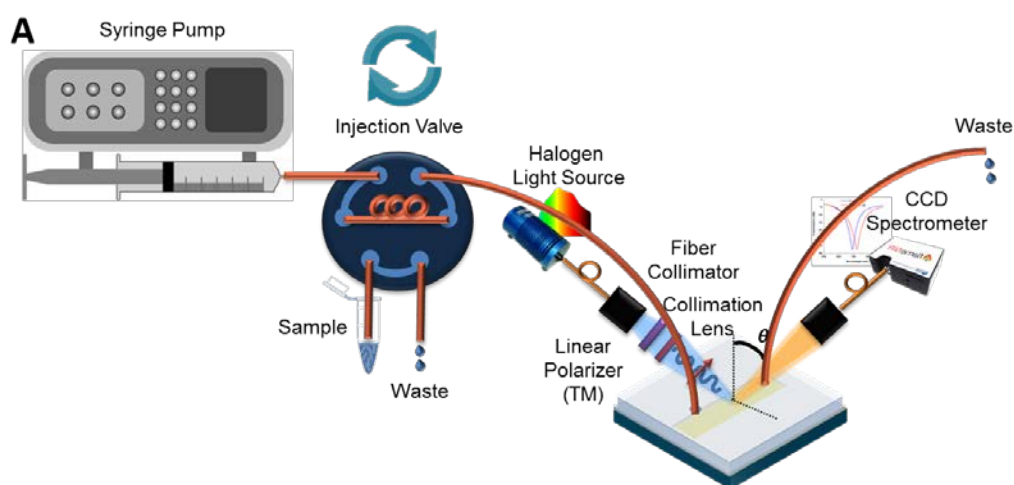
B
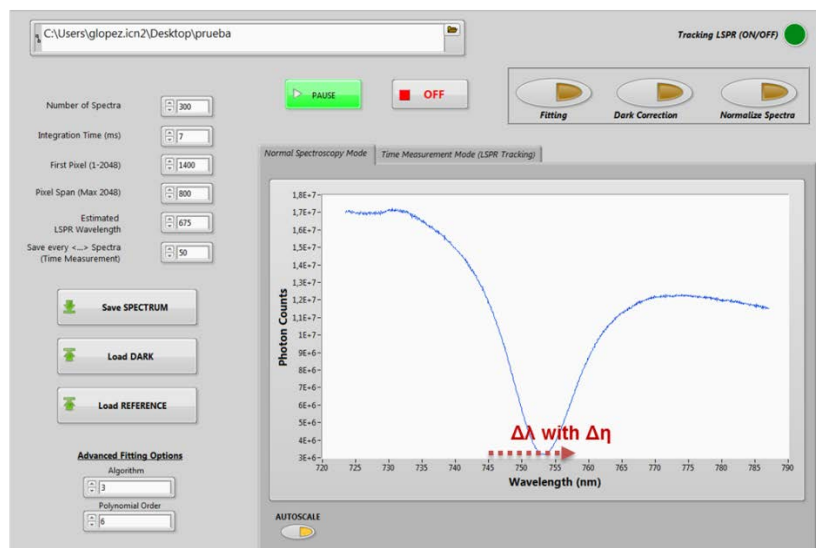
Figure 3.3 (A) Representation of the experimental set-up for the evaluation of the sensing performance, including the microfluidic system. (B) Custom made software interface to monitor real-time changes in the RI of the sensing media.

The real-time changes in the resonance peak position (λ_{SPP}) via polynomial fit were tracked by using custom made virtual instrumentation software (National Instruments, Labview, USA). The software acquires 300 reflectivity spectra with an integration time of 3 ms to maximize the signal from the CCD spectrometer; these acquisition parameters were fixed to obtain optimum signal to noise (S/N) ratio without significantly increasing the data acquisition time. Later, the spectra are averaged and the resonance peak position is estimated via polynomial fit. The fit parameters (algorithm and polynomial order) were fixed and may vary depending mainly on the FWHM of the plasmonic resonance.

The refractive index sensitivity *S* and FWHM of the sensor as a function of the incidence angle were extracted and the FOM estimated using solutions of glycerol in water (ranging from 4.2 mM to 136 mM, equivalent to a range of refractive indexes between 1.3334 and 1.3463 RIU). The results are summarized in Figure 3.4.
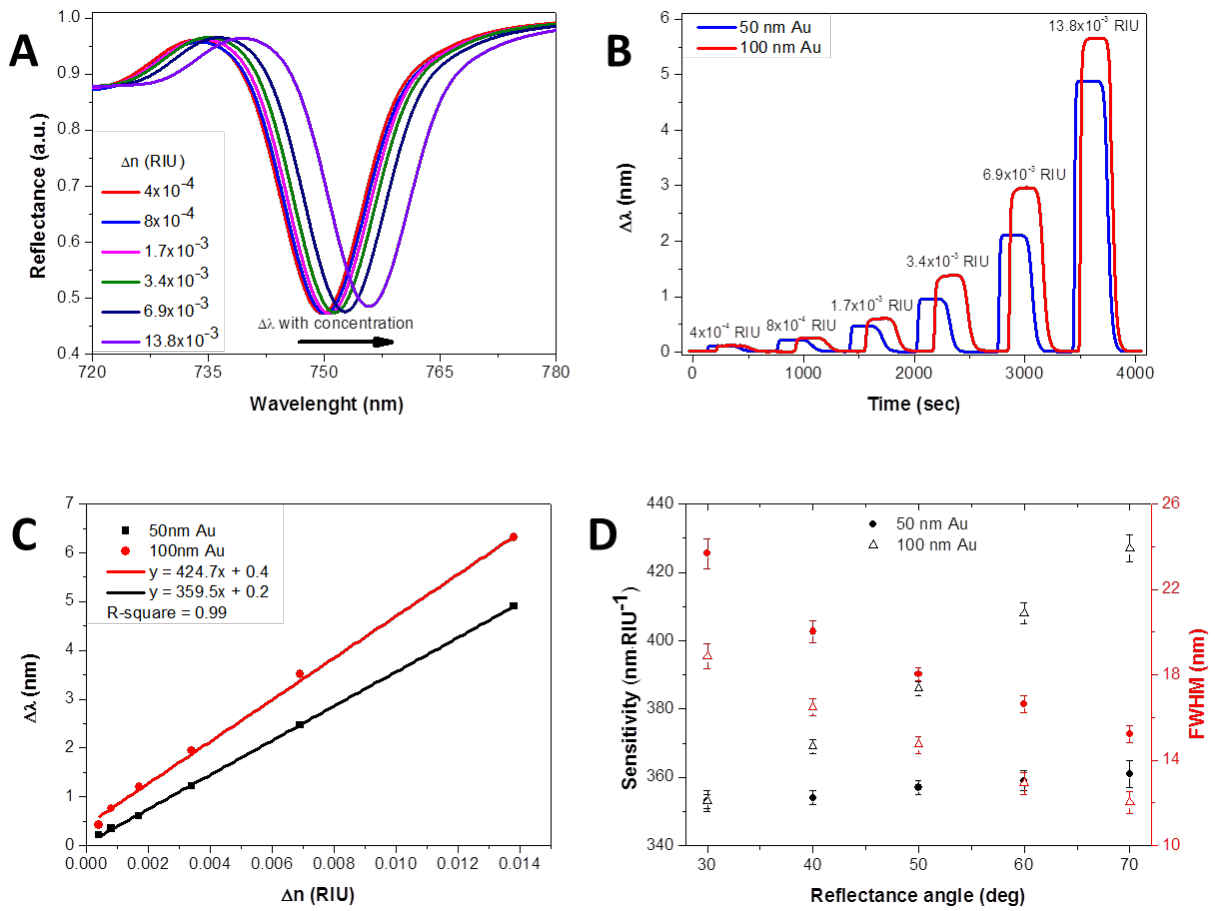
Figure 3.4 Sensing performance evaluation of the plasmonic sensors. (A) Variation of the reflectance spectra of a nanostructured plasmonic chip with a 100 nm gold layer thickness for different solutions of glycerol at an incident angle of 70⁰. (B) Real-time sensograms of different solutions of glycerol for the two gold thicknesses. (C) Calibration curves and sensitivity determination for the two gold thicknesses at an incidence angle of 70⁰. (D) Variation of the sensitivity (black) and FWHM linewidth (red) as function of the angle of the incidence for the two gold thicknesses.

These acquisition parameters were considered appropriate to obtain optimum signal to noise (S/N) ratios without significantly increasing the data acquisition time. In agreement with the theory, a shift of λ_{SPR} to higher wavelengths up to 6 nm is observed as the refractive index of the medium increases (see Figure 3.4A). The real-time sensograms (see Figure 3.4B) and the calibration curves (see Figure 3.4C) show an enhancement in the sensing performance for the 100 nm gold layer sensor compared to the 50 nm gold layer sensor (by approximately 20% improvement in sensitivity). As can be observed in Figure 3.9d and as summarized in Table 1, a

higher incident angle promotes an increase in sensitivity and a decrease in FWHM for both thicknesses, as summarized in Table 1. Maximum bulk sensitivity and minimum FWHM values were obtained at 70° incident angle of light. Sensitivity values of $\approx$ 425 nm·RIU^{-1} and 360 nm·RIU^{-1} with FWHM values of 12 nm and 15 nm were achieved for 100 nm and 50 nm gold layer thicknesses, respectively, giving as result a FOM of up to 35 nm^{-1} for the 100 nm gold thickness layer. The achieved FOM for the 100 nm gold layer sensor represent an improvement up to 58% compared to the FOM obtained for the 50 nm gold layer sensor (15 nm^{-1}), demonstrating the superior sensing performance of the 100 nm gold layer sensor.

Table 1. Variation of the sensitivity and FWHM for the 50 and 100 nm gold thickness layer sensors with the change in light incident angle.

Incident Angle θ	Sens. (nm·RIU^{-1})	FWHM (nm)	Sens. (nm·RIU^{-1})	FWHM (nm)
	50 nm Au		100 nm Au	
30º	352	24	348	19
40º	353	21	374	17
50º	356	18	392	16
60º	357	17	416	14
70º	360	15	425	12

The superior sensing performance of the 100 nm gold sensor compared to the 50 nm gold sensor could be correlated to the fact that as we analyze in Chapter 2, for the 100 nm gold layer there is a significant decrease in the interaction of plasmons with the underlying substrate, which increases the intensity of the optical fields with longer decay lengths as compared with the 50 nm gold layer. It is well known, that the decay length of the evanescent field can influence the sensitivity of the sensor[107].

3.1.3 Fixed angle reflectance experimental set up

Once the incident angle was selected and fixed, a miniaturized system was devised for the development of a potential portable device. For the miniaturized

system, a custom made triangular aluminum platform (50 mm x 35 mm) and a chip holder (40 mm x 15 mm) were designed with CAD software (Autodesk, Inc., Inventor, USA) as depicted in figure 3.5, with lateral sides designed at an angle of 70⁰.

On the designed fixed angle platform, rails are attached for the mounting of the optical components necessary for the TM mode excitation and the collection of the reflected light. These optical rails are attached perpendicular to the lateral sides of the aluminum base platform, thereby assuring incoming and outgoing optical paths at an angle of 70⁰. The combination of all optical components mounted on the left of the base platform assures the excitation of the TM plasmonic mode with a collimated broadband halogen light source. All the optical components (lens, fibers…etc.) were the same as those used for the variable angle experimental set-up previously described in section 3.2.2 and are mounted on a portable 75 mm x 75 mm breadboard, illustrating the portability and the small size of the system.
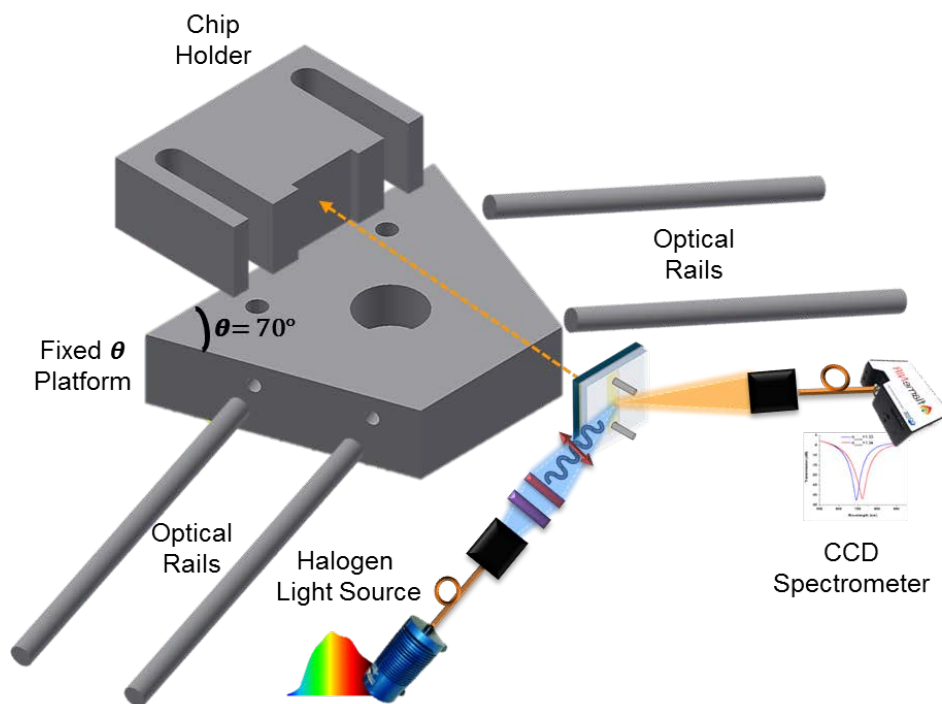
Figure 3.5 Schematic representation of the fixed angle reflectance experimental set-up. It shows the custom made 70⁰ fixed angle platform and chip holder designed to achieve a miniaturized system for extensive laboratory use.

The nanostructured plasmonic sensor chips are clamped in a grove (10 mm x 10 mm) that provides precise centering of the sample. Top-view and front-view photographs of this system are shown in Figure 3.6.
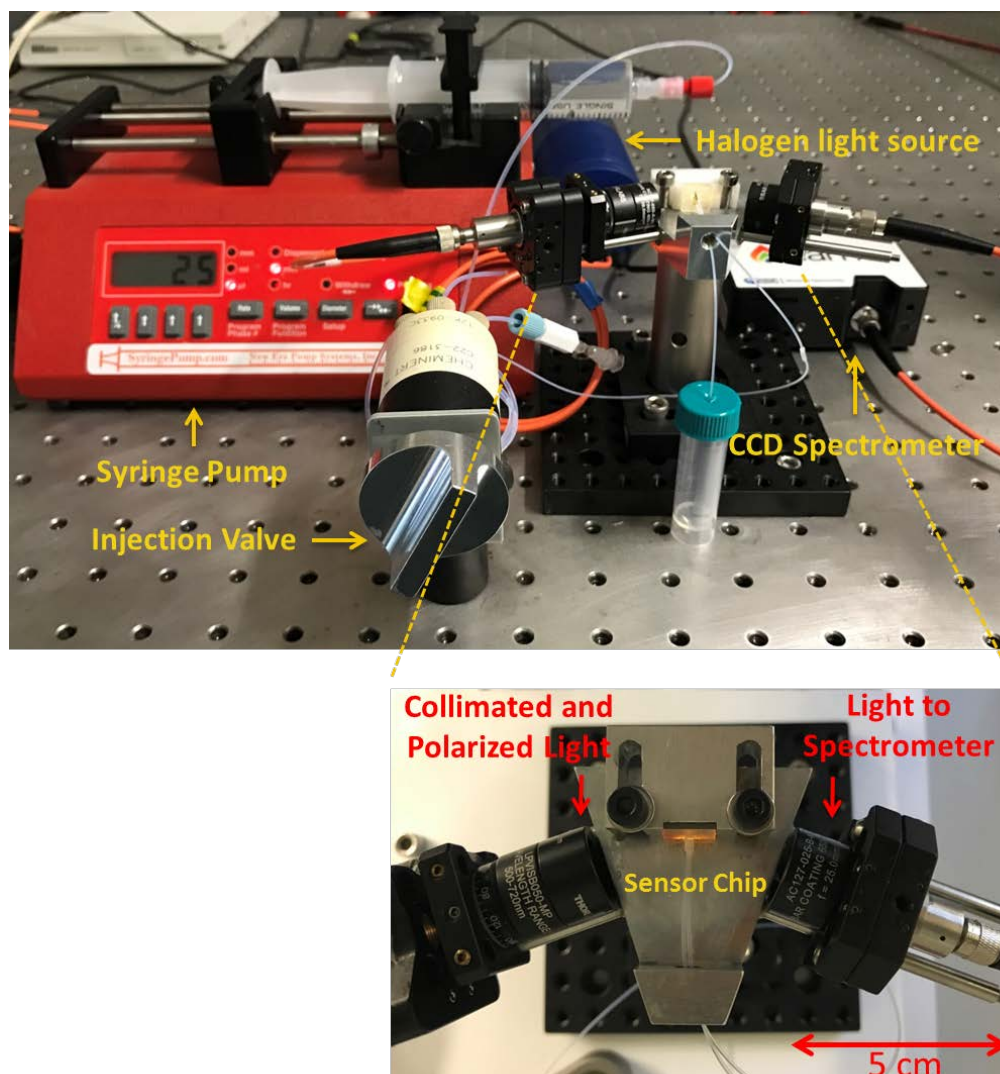
Figure 3.6 Top-view and front-view photographs of the miniaturized system.

3.1.4 Batch to batch reproducibility evaluation

The reproducibility of the batch to batch fabrication is one of the main requisites in achieving high-throughput nanostructured-based plasmonic biosensors, crucial for offering a reliable biosensor device. The reproducibility of the fabrication process was assessed by recording and analysing the reflectance spectra of nine

sensors with a gold thickness layer of 100 nm from different fabrication batches. The plasmonic sensor chips were clamped to the custom-made optical platform with fixed angle to perform reflectance measurements. The spectra were collected under room conditions using the air as sensing media.

The resultant reflectance spectra for the nine sampled sensors are presented in Figure 3.7. From the measurements a mean resonant wavelength λ_{SPR}, of 635.3 nm with a standard deviation of only 0.6 nm between the samples was obtained, and for the FWHM a mean value of 10.1 nm with a standard deviation of 0.9 nm. The insert in Figure 2.10 shows a very low dispersion in both parameters for the nine samples. Overall, both the high-throughput fabrication process of Blu-ray discs at industrial scale, which is completely established, and the simple steps necessary to obtain the plasmonic sensors (only cleaning and gold evaporation steps) contribute to the achievement of highly reproducible plasmonic sensors from batch to batch.
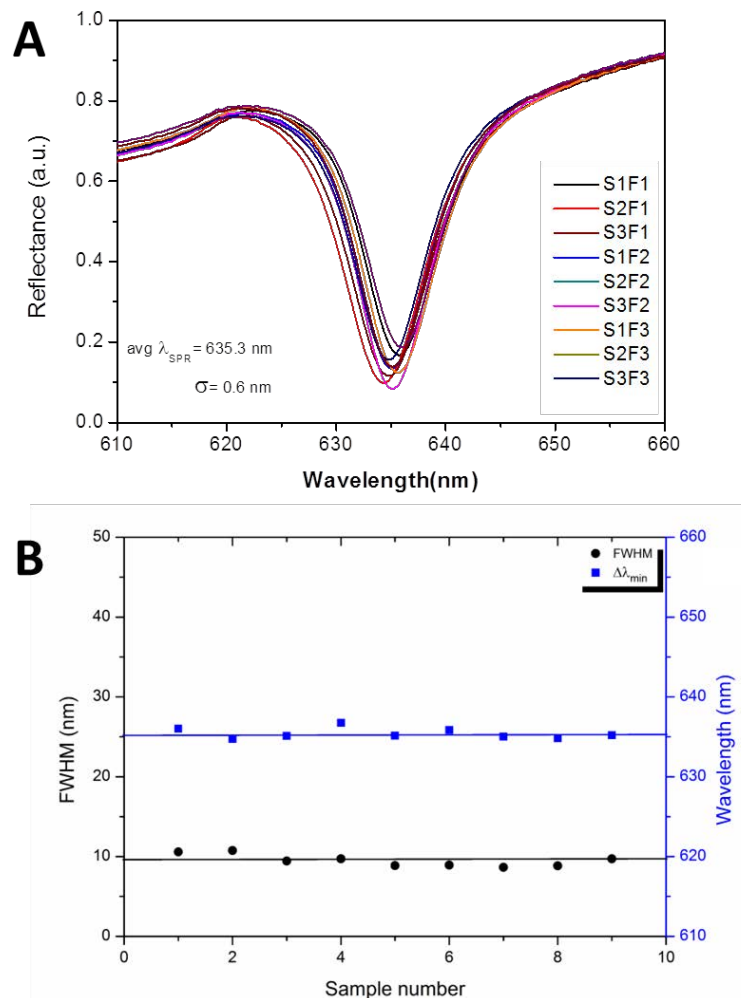
Figure 3.7 Reproducibility evaluation of the fabrication process. (A) Reflectance spectra under TM-polarized light with a fixed incident angle of 70° in air (n=1.00) for nine different sensors with 100 nm gold thickness layer obtained in three different fabrication batches. (B) Resonant wavelengths and FHWM bandwidths of the nine sensor chips mean values of 635.3 ± 0.6 nm and 10.1 ± 0.9 nm were obtained, respectively.

3.1.5 Noise analysis and Limit of Detection

To perform the estimation of the LOD of the plasmonic sensor, the noise level of the experimental system under the real-time measurement of the baseline was quantified. A plasmonic sensor chip was rinsed with MilliQ water and ethanol and then air dried. Later, the sensor was packed, clamped to the miniaturized platform and connected to the microfluidic system. Finally, MilliQ water (n=1.33) was flowed at a flow rate of 20 μL/min, which is an average flow rate commonly used in our lab for biosensing experiments. The real-time changes in the resonance peak position (λ_{SPP}) of the base line were tracked from a polynomial fit of 300 consecutive spectra with a CCD integration time of 3 ms.
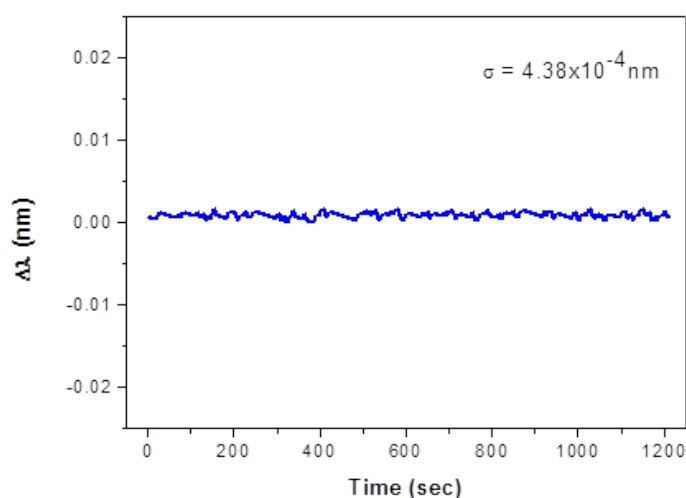
Figure 3.8 Noise level estimation from the baseline sensor response.

A noise standard deviation of 4.38 $\times 10^{-4}$ nm (see Figure 3.8) was achieved for the normalized base line, which is considered the noise level of the system. Considering a sensitivity value of 425 nm·RIU^{-1} for the nanostructure-based plasmonic sensor and 3-times the noise standard deviation 1.31×10^{-3} nm, we were

able to achieve a LOD in the range of **3.08x10⁻⁶ RIU** for the plasmonic sensor placed in the miniaturized system.

The achieved LOD is near one order or magnitude better than some previously reported engineered nanoslit-based sensors measured under normal light incidence transmittance, for example by Lee[86] et al. (2015) obtained a LOD of 3.74 × 10⁻⁵ RIU. Overall, the sensing performance of our device is enough competitive and comparable to the current state of the art in SPR sensors[34,43], in addition to offering a simple and reproducible fabrication process.

3.2 Proof-of-concept of label-free biosensing

3.2.1 Design of the biosensing assay methodology

The potential of the developed nanostructured plasmonic sensor chip for biosensing applications was assessed with a direct assay based on the detection of specific autoantibodies against GTF2b (general transcription factor IIB) protein, a suspected Tumor Associated Antigen (TAA) related to colorectal cancer[126]. TAAs are overexpressed proteins associated with malignant growth. The detection of the TAAs is highly interesting for early cancer detection[127]. However, these TAAs become even more relevant since some cancers have demonstrated to be immunogenic, so that they can stimulate the immunoresponse, triggering the generation of specific autoantibodies by the human immunosystem[128].

Therefore, the detection in a patient's blood sample of the generated autoantibodies against these TAAs is even more remarkable as they can be detected at higher concentrations and at very early stages of the disease compared with TAAs[129]. Most common methodologies used for autoantibodies determination are enzyme-linked immunosorbent assay (ELISA) or protein microarrays, which provide qualitative or semi-quantitative results, based on relative signals compared with reference populations[130] As a consequence, there is potential for a precise quantification from a diagnostic and a therapy follow-up perspective. Considering these facts, we have developed as a proof-of-concept, an immunoassay based on the detection of autoantibodies.

The proposed biofunctionalization of the sensor surface for the antibody detection is based on the covalent coupling of the GTF2b protein to an alkanethiol SAM and the subsequent antibody detection. To achieve this, an alkanethiol SAM is formed in the surface of the sensor, then carboxylate groups are activated for the latter immobilization of the GTF2b protein and, finally, the carboxylate groups that did not react are blocked with ethanolamine. Then the target is flowed over the surface and after a stable signal is achieved, the surface is regenerated (usually with an acid/basic solution for a high pH contrast) to unbind the target molecules and to reuse the biofunctionalized surface to perform more bioassays. Figure 3.13 shows the schematic representation of the proposed biofunctionalization methodology and a scheme of a biosensing assay.
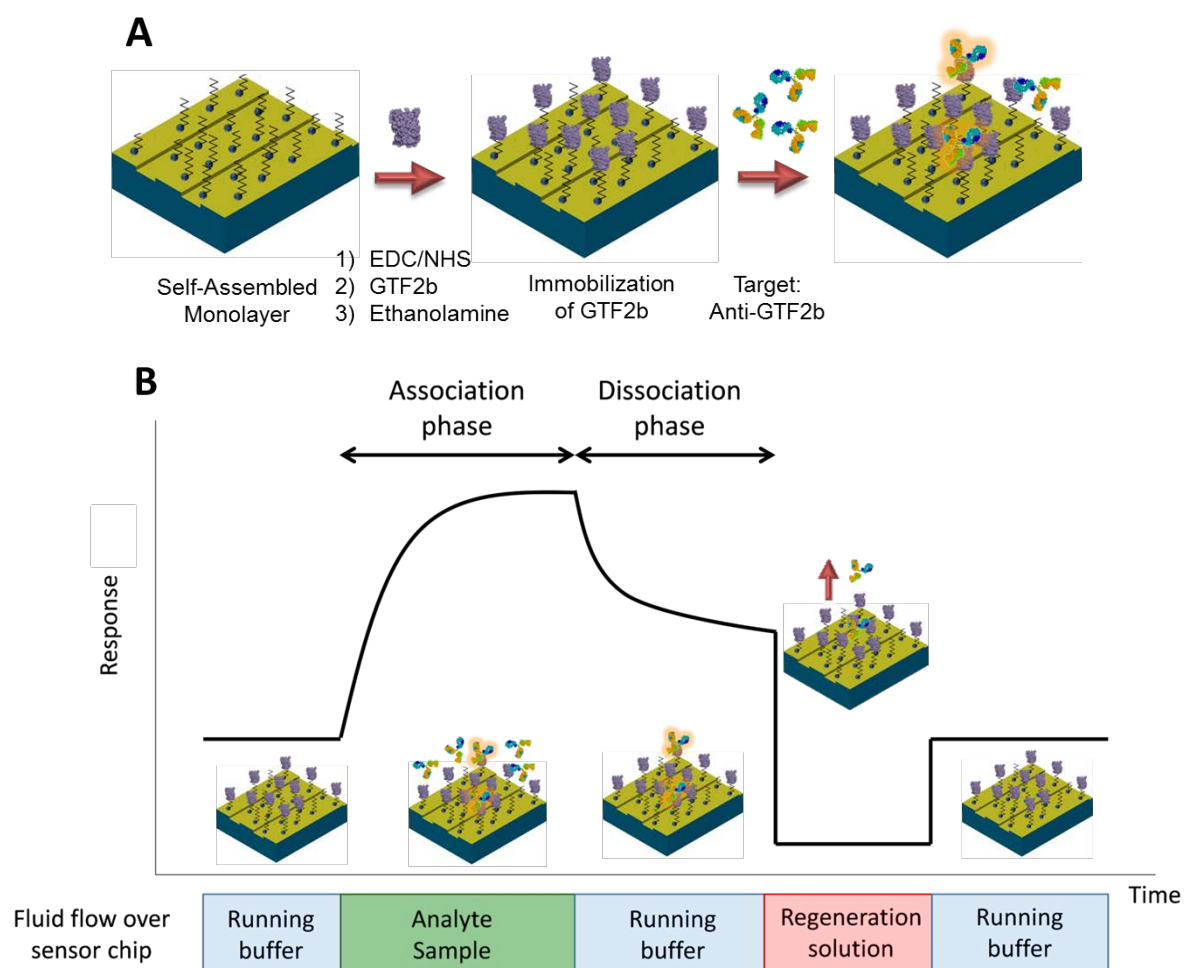
Figure 3.9 (A) Schematic representation of the TAA biofunctionalization methodology based on covalent coupling to an alkanethiol SAM and subsequent antibody detection. (B) Scheme of a biosensing assay including the required steps.

61

The materials and methods for the biofunctionalization methodology were as follows: alkanethiol for self-assembled monolayer (SAM) formation (16-mercaptohexadecanoic acid, MHDA), (1-ethyl-4 (3-dimethylaminopropyl) carbodiimide hydrochloride (EDC) and N-hydroxysulfosuccinimide (s-NHS) for carboxylic groups activation, ethanolamine and Tween 20 were acquired from Sigma–Aldrich (Germany). Poly(L-lysine)-graft-poly (ethylene glycol) co-polymer (PLL-PEG, MW~70000 g mol^{-1}) was purchased from SuSoS AG (Switzerland). Commercial serum was obtained from Sigma–Aldrich (Germany). Antibody anti-GTF2b was purchased from Santa Cruz Biotechnology (USA). GTF2b protein was provided by Protein Alternatives (Spain).

The sensor chips (100 nm thickness gold layer) were cleaned and activated for SAM formation by performing consecutive 1 min sonication cycles in ethanol and MilliQ water, drying with N_2 stream and finally by placing them in a UV/O_3 generator (BioForce Nanoscience, USA) for 30 min to activate the surface to promote the S–Au bonds with alkanethiols. An alkanethiol SAM with reactive carboxylic groups was obtained by coating the sensor chip with 500 μM MHDA in ethanol overnight at room temperature according to previous reports[119]. Then, the surface was rinsed with ethanol to remove residual alkanethiols and dried with a N_2 stream. Prior to biofunctionalization, the chip was bonded to the microfluidics and placed in the optical platform.

According to previous reports[119], the immobilization of the GTF2b protein was performed *in situ*, and was continuously monitored in real time. For the activation of the carboxylic groups, a solution of 0.2 M EDC/0.05 M s-NHS in 2-(N-morpholino) ethanesulfonic acid (MES) buffer (100 mM pH 5.5) was injected and flowed over the SAM monolayer at 20 μL/min (using H_2O as running buffer). Subsequently, a 50 μg/ml GTF2b protein solution in phosphate buffered saline (PBS) buffer (10 mM pH 7.4) was injected and flowed at 5 μL/min. Finally, a blocking solution (ethanolamine, 1M pH 8.5) was injected for 2 min at 25 μL/min.

After *in situ* immobilization of the GTF2b protein (see Figure 3.10A, PBST 0.5% (PBS 10mM pH 7.5 +0.5% Tween 20) was established as a running buffer to

improve the stability of the biolayer. For optimization and assessment studies, different concentrations of the specific antibody diluted in PBST 0.5% were flowed over the functionalized surface at 25 µL/min. Data points were collected after signal stabilization with a polynomial fit of 300 consecutive spectra and a CCD integration time of 3 ms. Regeneration of the surface was achieved by injecting a short pulse of 20 mM NaOH for 2 min at 65 µL/min to release the anti-GTF2b and preserve the biolayer.

The detection of the specific antibody associated with this protein shows a good dose-response relation for different concentrations of the antibody (see Figure 3.10B). The negative control (1 µg/mL of BSA protein) resulted in no background ($\Delta\lambda_{SPR}$=0) (see Fig. 3.10B, wine), which confirms the lack of nonspecific binding onto the biofunctionalized surface. Given the excellent S/N ratio obtained with the setup and the processing software, we were able to achieve a LOD of only 3.4 ng/mL (22.6 pM) and a limit of quantification (LOQ) of 11.4 ng/mL (75.6 pM), respectively (see the calibration curves in Figure 3.10C which were fitted to a one-site specific binding model. LOD and LOQ were calculated as the concentrations corresponding to the blank signal plus three and ten times it is SD, respectively). Although the serological concentration levels of colon rectal cancer autoantibodies have not been fully established, as most research mainly focus on their identification, it cannot be obviated the usefulness of knowing this concentration from a perspective of early diagnosis of this disease.

The obtained values (LOD= 3.4 ng/mL) are slightly better (near 3-times better LOD) than the ones previously obtained (LOD= 10 ng/mL) for the same assay but with gold nanodisks as the substrate using an optical setup under prism-coupled TIR (total internal reflection) measurements[119]. Whereas gold nanodisks offer excellent properties, this new approach provides an even faster and highly reproducible fabrication method and minimizes the optical setup complexity as the use of prism as a light coupling method is unnecessary.
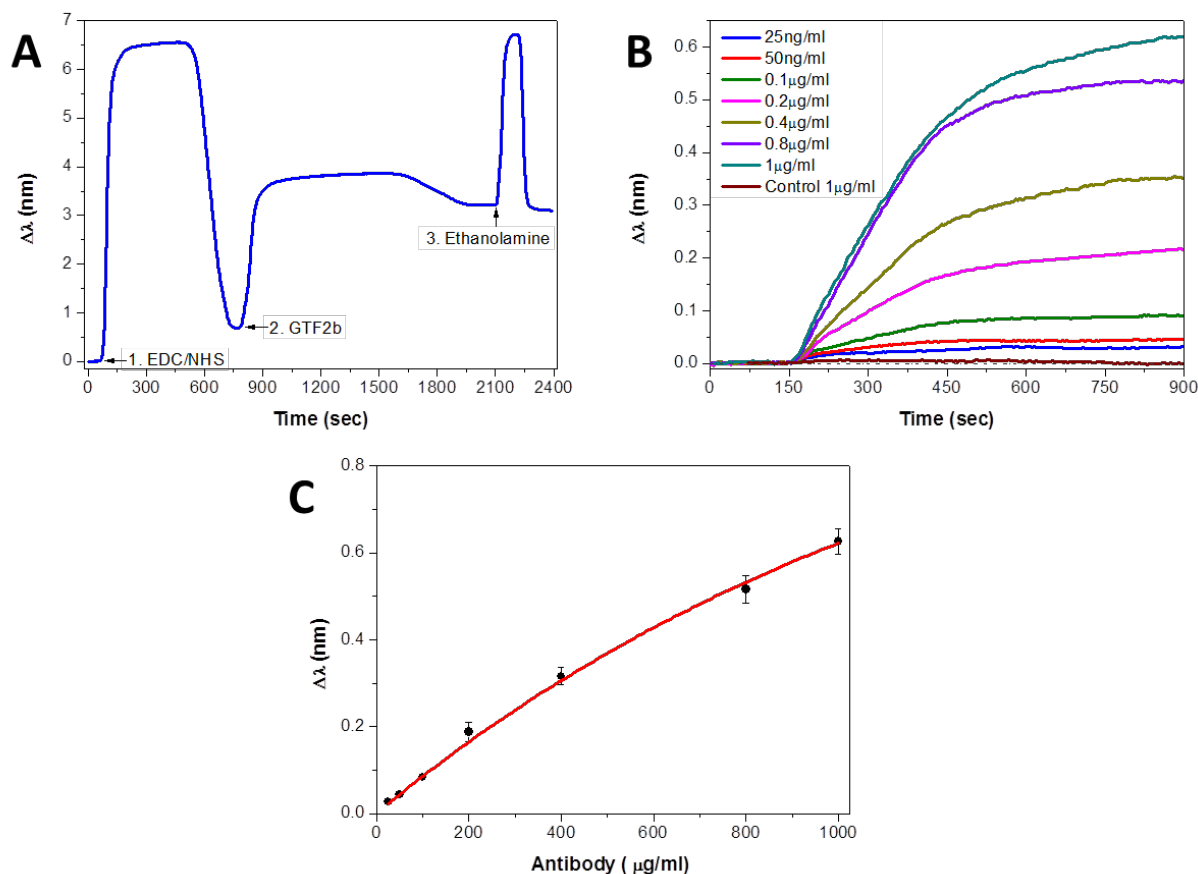
Figure 3.10 (A) Real-time sensograms showing the covalent immobilization of the protein GTF2b: activation of carboxylic SAM layer with EDC/NHS, attachment of the protein and blocking of unreacted groups; (B) sensograms showing the detection of the specific antibody at different concentrations (from 0.025 to 1 µg/mL) and control experiment; (C) calibration curve for the detection of the anti-GTF2b.

In order to also preliminary assess the feasibility of measuring biological samples; an additional blocking step was employed (see Figure 3.11A) based on the addition of a PLL-PEG solution, a well-known compound able to minimize nonspecific adsorptions in complex media[52]. A PLL-PEG solution (0.25 mg/mL) in HEPES buffer (10 mM, pH 7.0) was flowed over the functionalized surface at 25 µL/min for 20 min. Once the surface was blocked, a known concentration of the specific antibody (800 ng/mL) was flowed to evaluate the effect of the PLL-PEG in the detection of the antibody. As can be seen in the green and magenta lines in Figure 3.15b, a similar shift occurs before and after blocking, being around 0.5 nm in both cases with no significant changes in biosensing response. A significant change

in biosensing response is related with the blocking step, mainly due to an over block of the surface which can highly reduce the active binding sites and as consequence highly reduce the biosensor response.
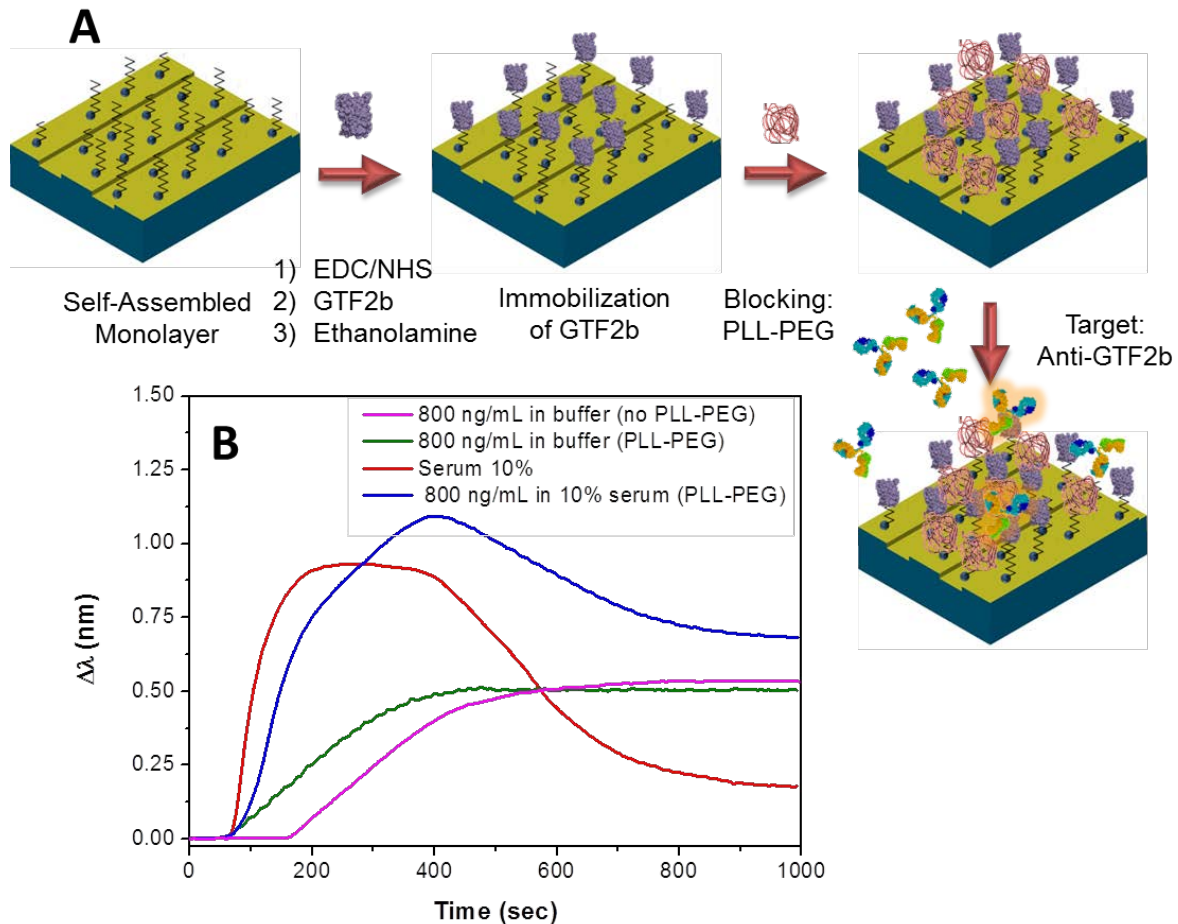
Figure 3.11 (A) Schematic representation of the TAA biofunctionalization methodology including the additional blocking step and subsequent antibody detection. (B) Effect of the PLL-PEG blocking step in the detection: green and magenta lines show the detection of antibody (800 ng/mL) without and with PLL-PEG layer, respectively; red line shows the nonspecific binding of 10% diluted serum; blue line shows the detection of antibody (800 ng/mL) in 10% diluted serum.

Finally, as a proof-of-concept to test the biosensor and the bioassay under a complex media with clinical relevance, diluted serum was evaluated; 10% serum and 10% serum (800 ng/mL) spiked with the specific antibody were flowed. Although the blocking did not completely remove the binding of serum components resulting in a shift around 0.2 nm for 10% serum (see Figure 3.11B, red line), it did not affect the

target detection in the buffer: when measuring in diluted serum (blue line in figure 3.11B) a total signal of approximately 0.7 nm was observed corresponding to the contribution of both the serum ($\Delta\lambda$ around 0.2 nm) and the specific target binding ($\Delta\lambda$ around 0.5 nm).

Chapter 4. Multiplexed Biosensing Platform

This chapter discusses the development of a multiplexed label-free biosensor based on the nanostructured plasmonic sensors. First, we describe the design, fabrication and optimization of a four-channel microfluidic header. Later we describe the sensing characterization of multi-channel plasmonic biosensors by evaluating the noise level and the limit of detection. Finally, two biosensing assays were performed: 1) a four-channel biofunctionalization was made to detect the presence of a protein biomarker, in order to evaluate the inter-channel biosensing performance and reproducibility, and 2) a selective channel biofunctionalization was performed to detect the presence of two protein biomarkers, in order to evaluate the feasibility to perform multiplexed biosensing as a proof-of-concept. The Interleukin-6 (IL6) and the C-reactive (CRP) proteins, valuable biomarkers related to inflammation and infection processes, were evaluated.

4.1 Biosensor packing and optical characterization

4.1.1 Multiplexed microfluidic integration

Based on our previous design for a single microfluidic channel, we developed a four channel design to perform parallel biosensing in multiple channels. To develop the multichannel microfluidic path, we used designs to minimize and simplify microfluidic instrumentation. A simple method to analyze a microfluidic network is by using the analogy between a hydraulic and an electrical circuit. This concept can be applied considering that the pressure drop in a microchannel is analogous to the voltage drop in a conductor, the flow rate to the current and hydraulic and electrical resistance[131,132].

Considering this analogy of an electrical design, the same flow rate in all the microfluidic channels is required to keep mass transfer homogenous between them, and, as a consequence, to minimize their variance in the biosensing response. Figure 4.1 shows the electrical equivalent diagram for a four channel symmetrical

microfluidic path for homogenous flow division between the channels. To achieve a homogenous flow the following expression must be fulfilled:

$$I = I_1 + I_2 + I_3 + I_4 \qquad (4.1)$$

where I represent the flow rate provided by the syringe pump and $I_{1...4}$ represents the flow rate in each channel. From this expression, considering Ohms law for a parallel circuit, resistance $R_{1...4}$ should be equal between all the channels. To fulfill a homogeneous resistance between the microfluidic channels, symmetry between them is required including tubing dimensions, path length, etc[133]. To achieve such symmetry, we evaluate in a first step the use of a commercial microfluidic splitter
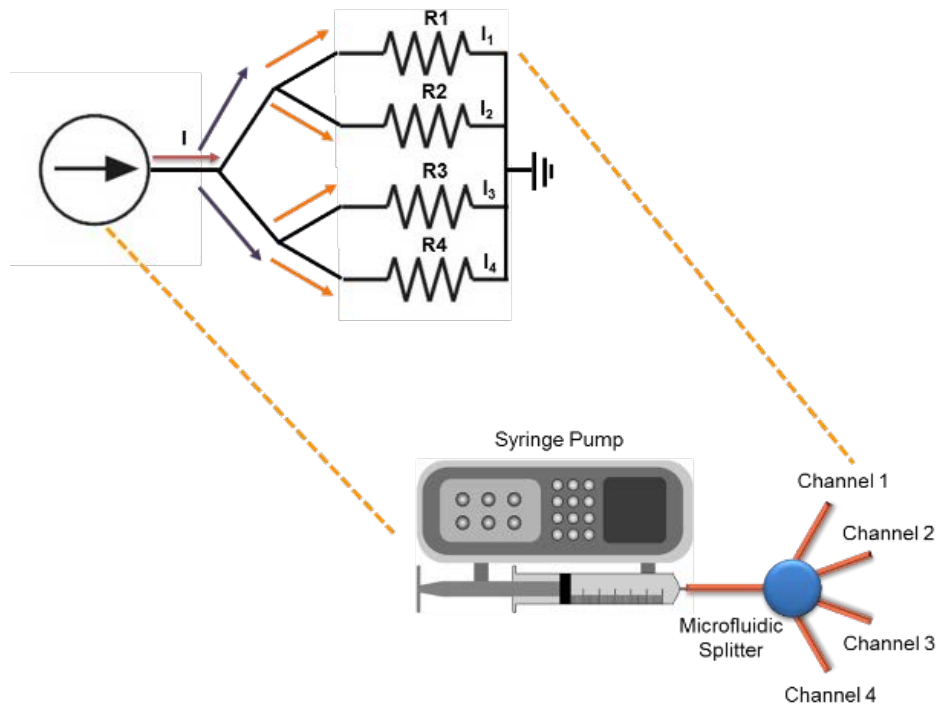
Figure 4.1 Representation of the electrical equivalent diagram for a four channel microfluidic path with homogenous flow division between the channels.

The commercial microfluidic splitter (Darwin Microfluidics, KM9, France) has 9 ports: 1-inlet and 8-outlets, from which only 4-outlets were enabled. The four channels plasmonic sensor chip was designed to have 4-inlet to 4-outlers and the dimensions of the microfluidic channels were the same as those used with the one channel design in order to achieve a highly compact four channel sensor chip with

dimensions of only 1cm width x 2cm length. The packing scheme using COC for the four channel sensor was similar to that previously described in section 3.1.2 for a single channel sensor: a commercial double-sided adhesive tape for microfluidics (Microfluidic Chip Shop, GmbH., MCS-foil-008, Germany) was patterned with the microfluidic channels using a cutting plotter (Graphtec America, Inc., CE6000-40, USA). Individual COC lids (2 cm^2 and 1mm thickness) were obtained by cutting a COC foil (Microfluidic Chip Shop, GmbH., Zeonor 10-0710-0657-1.0-02, Germany) with a conventional computer numerical control (CNC) router (LPKF Laser & Electronics, Protomat C100/HF, Germany), and Teflon/peek tubing was connected and bonded to the lid using cyanoacrylate instant adhesive (Henkel AG & Co., Loctite 414, Germany).

Figure 4.2 shows the experimental set-up employed to evaluate the performance of the commercial microfluidic splitter. A commercial 9 port microfluidic splitter (Darwin Microfluidics, KM9, France) and a plasmonic chip with a 4-inlet to 4-outlers design were connected to a microfluidic system consisting of a syringe pump (New Era, NE-1000, USA) and a manually operated injection valve (Valco Instruments Co. Inc., Cheminert C22-3186, USA). Milli-Q water was flowed over the system at a flow rate of 100 µl/min (for a 25 µl/min flow rate per channel). To estimate the flow rate in each channel the individual waste per channel was collected and later weighted to estimate the flow rate per channel considering the definition of density according to the following expression:

$$D = m/v \qquad (4.2)$$

where D is the density of the liquid (1 gr/mL for water), m the weight and v the volume.

After estimating the flow rate in each channel, we found significant differences between the channels with a variance between them of over 20%. Moreover, the ports of the commercial microfluidic splitter tended to frequently interrupt the flow in one or more channels. These issues can be correlated to variations in the fluidic resistance between the channels with differences in the length, position and the fit between the tubes.
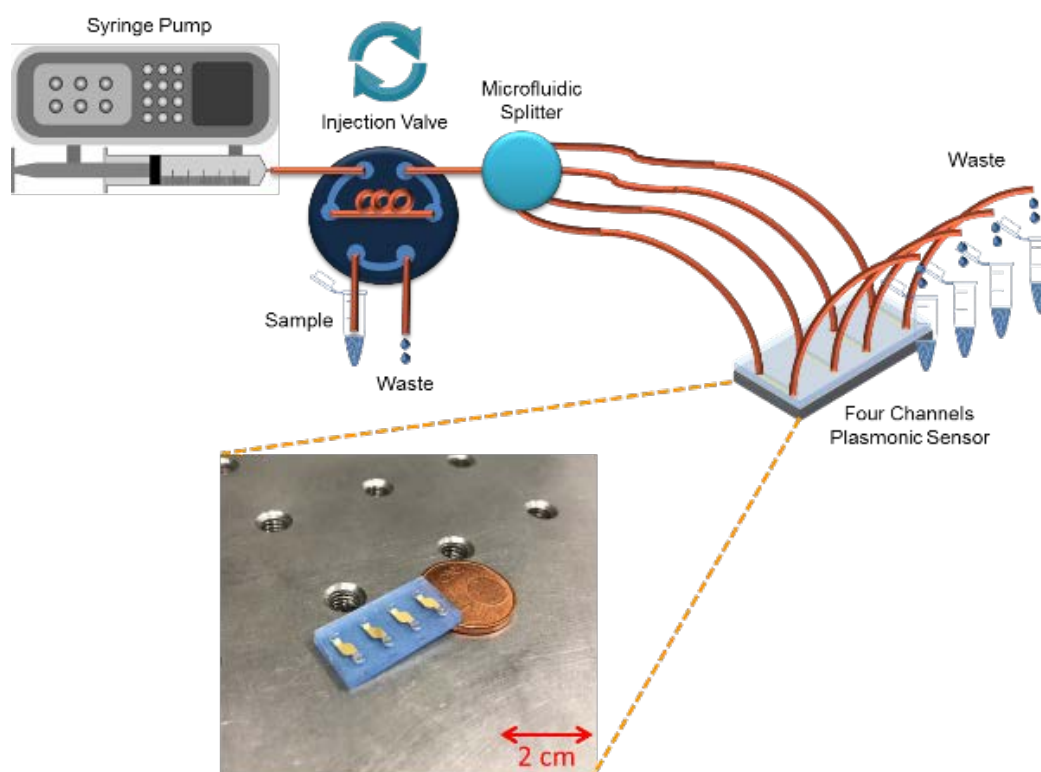
Figure 4.2 Experimental microfluidic set-up for the multichannel plasmonic sensing evaluation using a commercial microfluidic splitter. The insert shows the four channels packed plasmonic sensor chip used for the experiments.

Considering these results, we decided to design a flow splitter on-chip with the aim of simplifying the microfluidic circuit and minimizing potential differences in flow resistance between the channels. Two different designs were devised: a 1-inlet to 4-outlets design that could allow performing *in situ* and *ex situ* biofunctionalization for each channel, and a 1-inlet to 1-outlet design to simplify the implementation but that would require *ex situ* biofunctionalization for multiplexed biosensing assays. The designs are shown in Figure 4.3 and as can be observed, the design is symmetrical in order to allow a homogenous flow distribution across all the channels.
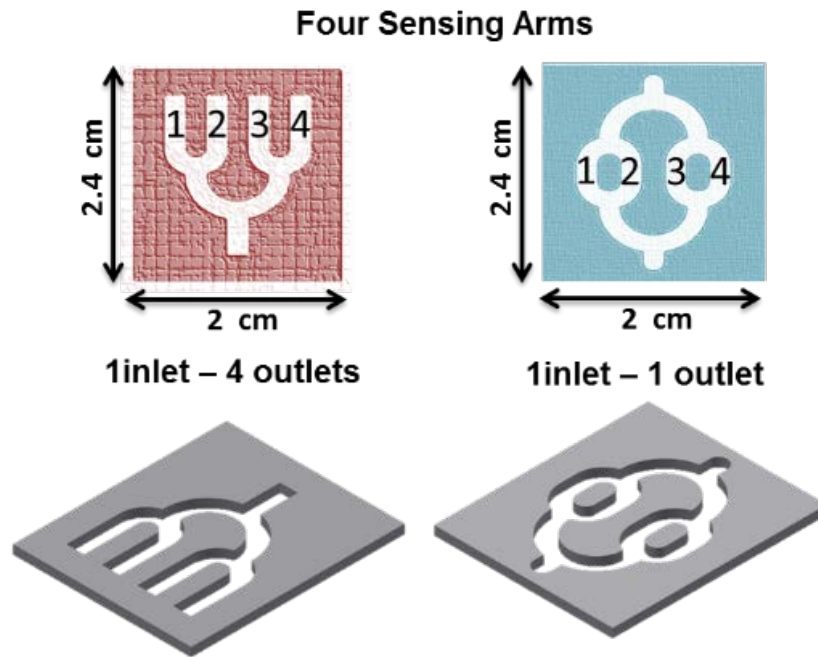
Figure 4.3 Representation of the two microfluidic designs to perform a four-channel multiplexed biosensor. A 1-inlet to 1-outlet design (right) and a 1-inlet to 4-outlets design (left).

The packing scheme using COC is the same as that previously described in section 2.3.2 for a single channel biosensor with just two changes: the microfluidic path length was longer compared with the previous design and as consequence the dimensions of the plasmonic sensor chip and the COC lids increased to an area of 4.8 cm^2. Figure 4.4 shows a schematic representation and photographs of the packed 4-channel sensor. Later, the 1-inlet to 4-outlets on-chip splitter sensor was connected to the microfluidic system for evaluation with the same described protocol used for the 4-inlets to 4-outlets sensor chip.

In contrast to the commercial microfluidic splitter, no significant difference in the flow rate was observed between the channels for the 1-inlet to 4-outlets design, with a variance between them on average of around 5% and no interruptions in the flow were observed between the channels .This low variance in flow rate and the lack of flow interruptions in the microfluidic channels is related to a decreased resistance difference between the channels mainly due to the high symmetry between them and the reduced connections that could increase their resistance.
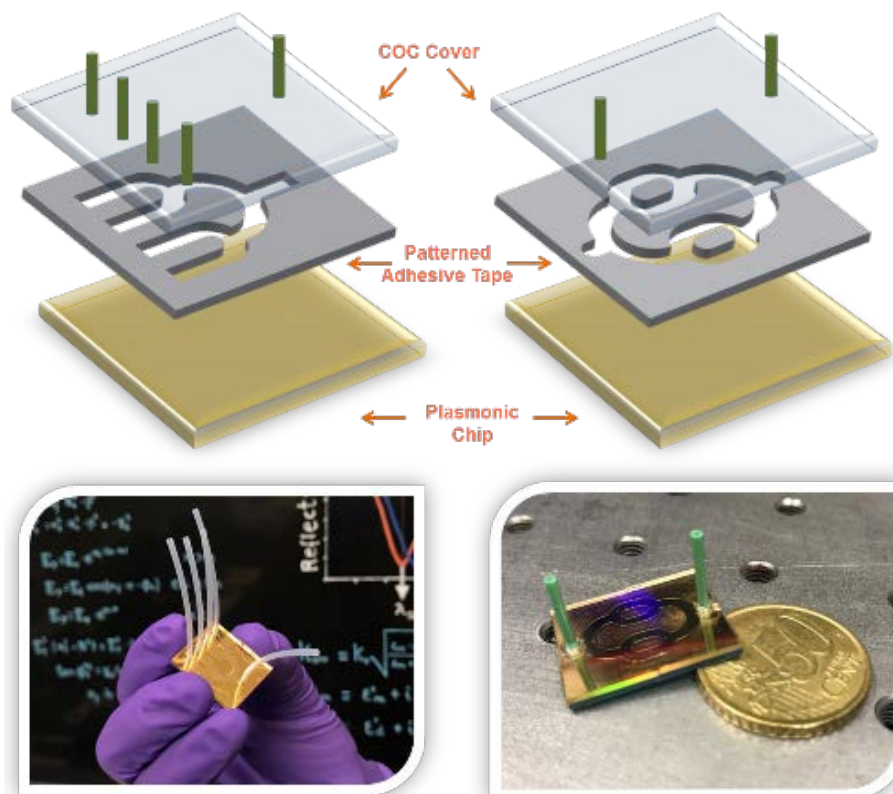
Figure 4.4 Schematic representation and photographs of the 4-channel packed sensor with the two microfluidic designs to perform a four-channel multiplexed biosensor. A 1-inlet to 1-outlet design (right) and a 1-inlet to 4-outlets design (left).

4.1.2 Sensing performance

The experimental system for the evaluation of the multiplexed biosensor was based on a spatial multiplexing: we sensed sequentially each one of the sensing channels by using a motorized linear stage. Each set of measurements in the four channels was plotted as a group and not in space time.

For the system, an aluminum platform and a Teflon chip holder were designed and fabricated, as depicted in figure 4.5A, the aluminum platform had lateral sides designed at an angle of 70º. On this platform, the optical rails were attached for the mounting of the optical components necessary for the TM mode excitation and the collection of the reflected light. These optical rails were attached perpendicular to the

lateral sides of the aluminum base platform, thereby assuring incoming and outgoing optical paths at an angle of 70⁰.

As previously described in sections 3.1.1 and 3.1.3, the combination of all optical components mounted in one side of the base platform assures the excitation of the TM mode with a collimated broadband halogen light source. All the optical components (lens, fibers…etc.), were the same used for the 70⁰ miniaturized experimental set up previously described in 3.1.3. But in contrast to the previous set up, the aluminum platform was attached to a motorized linear stage (Thorlabs, Z825B, Germany) to control spatially the detection zone (X axis movement). The plasmonic sensor chips were clamped to a custom made Teflon chip holder with a grove that provided precise centering. The microfluidic tubes were connected to the corresponding port in the injection valve that ensures proper in- and outflow of samples in the system.
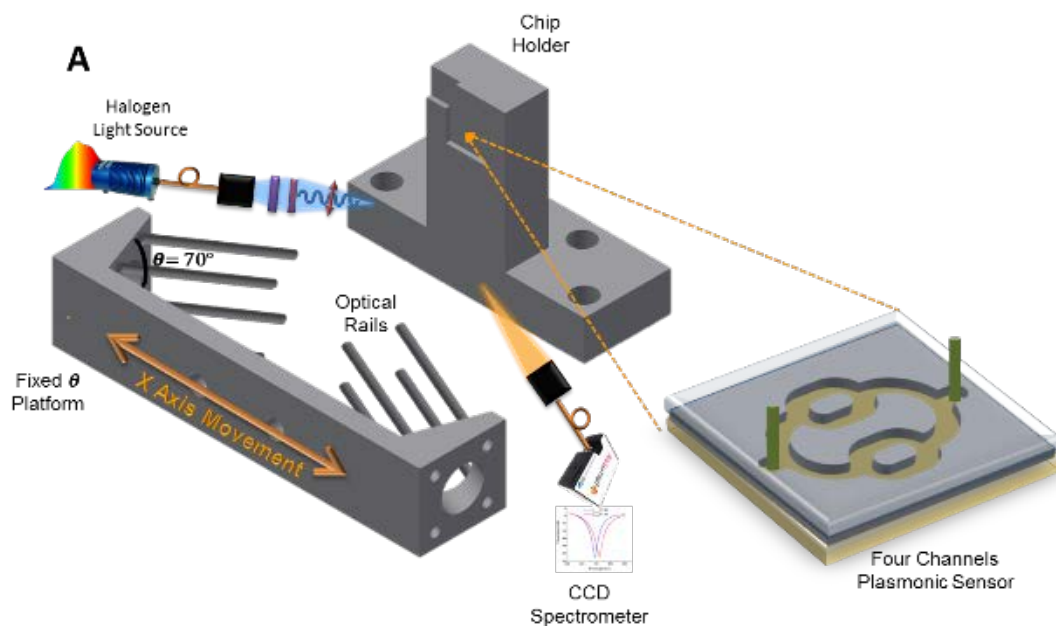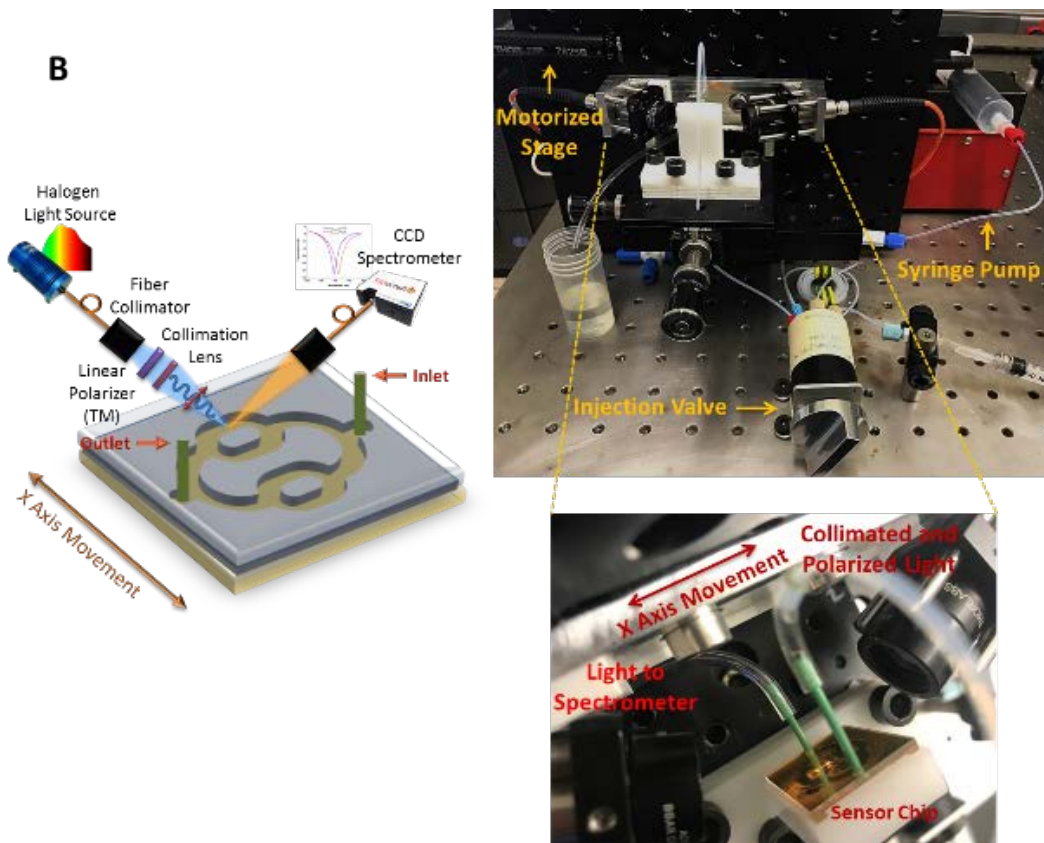
Figure 4.5 Spatial multiplexed experimental set-up. (A) Custom made 70⁰ fixed angle platform and sensor chip holder. (B) Front-view and top-view photographs of the experimental system (right), and schematic representation of the spatial multiplexed experimental set-up (left).

The effect of the microfluidic channels design on the sensing performance was studied by evaluating aqueous solutions of chlorhydric acid with different RI. They were connected to the microfluidic system consisting of a syringe pump, with adjustable pumping speed to guarantee a constant liquid flow, and a manually operated injection valve. Reflectivity spectra were acquired every 3 ms and 300 consecutive spectra were measured and averaged to provide the final spectrum.

The spatial control of the motorized linear stage and the real-time changes in the resonance peak position (λ_{SPR}) *via* polynomial fit were tracked for each sensing channel by using custom made virtual instrumentation software (National Instruments, Labview, USA) (Figure 4.6). The software additionally allows fixing of the spectra acquisition parameters (i.e. number of spectra, integration time,

wavelength, etc.) and the control of the motorized linear stage (i.e. number of channels, interchannel distance, start position, etc.).
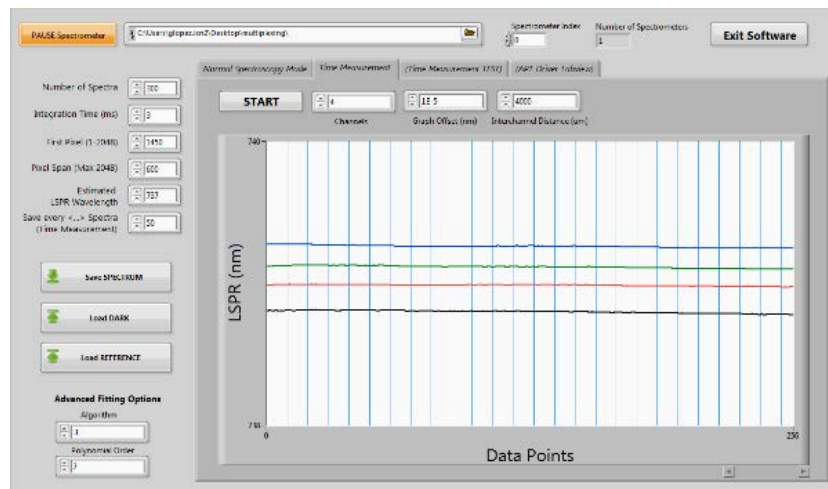
Figure 4.6 Custom made software interface to control spatially the motorized linear stage and the monitor real-time changes in the RI of the sensing media for the four-channel plasmonic sensors.

Figure 4.7 shows the plasmonic response to different solutions of chlorhydric acid in water (ranging from a Δn between 3×10^{-4} and 3.1×10^{-3} RIU). As it is shown in Figure 4.7 (left) the one-input to four-output design was prone to flow variations between the channels with a noticeable delay in the channels (Figure 4.7 left, red line). In contrast, the one-input to one-output design (Figure 4.7 right) had a homogenous flow between the channels with a minimum delay time between the channels. This behavior is correlated with the fact that the one-input to four-output design is prone to differences in fluidic resistance due to the increased number of exits (each exit has a different fluidic resistance, different lengths and angles in the tubing that can be correlated with this difference between channels). In contrast the one-input to one-output design has only one single input and one single output which minimize differences in fluidic resistance between the channels and ultimately simplifies the microfluidic circuit and the packing of the sensor.
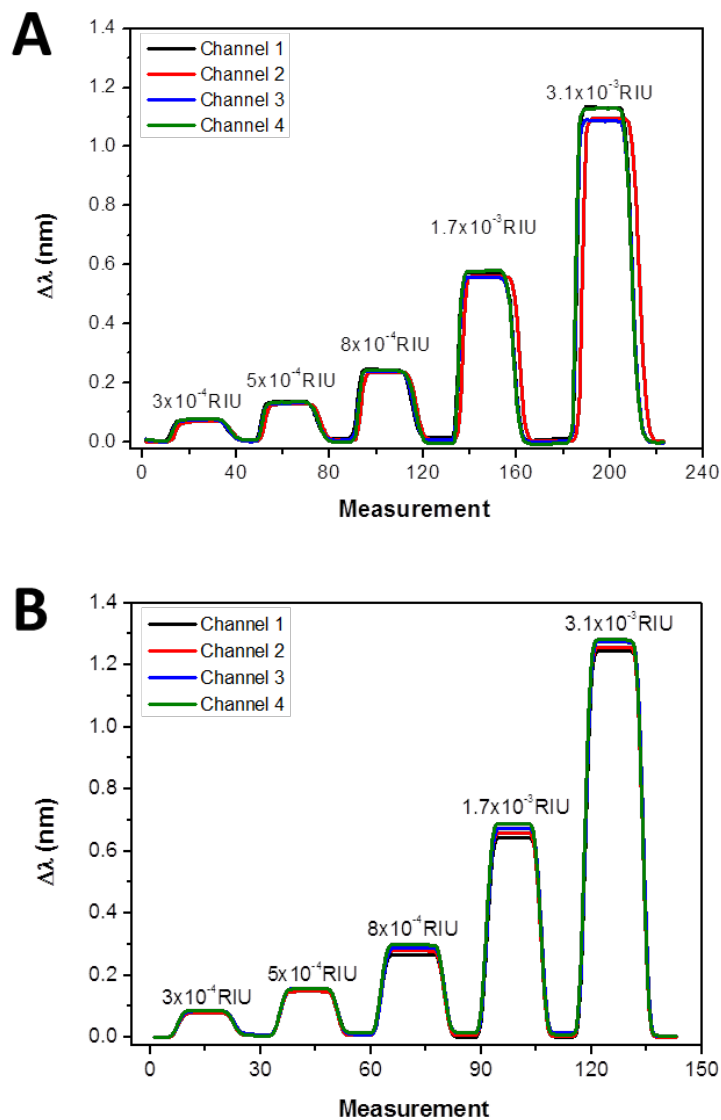
Figure 4.7 Two multichannel microfluidic designs and their fluidic/sensing response. (A) One-input to four-outputs. (B) One-input to one-output.

Table 2 shows a summary of the study of the coefficient of variation between the channels for the one-input to one-output design. The average coefficient of variation between the sensing channels is around 5.9% in the refractive index range evaluated. The average RI sensitivity from the four channels is 424 nm·RIU^{-1} with a standard deviation of only 5 nm·RIU^{-1} between them (see Figure 4.8). These results show the possibility of achieving high sensing reproducibility with a homogenous flow between the microfluidic channels.

Table 2. Variation response between the channels.

Δn (RIU)	Δλ$_1$ (nm)	Δλ$_2$ (nm)	Δλ$_3$ (nm)	Δλ$_4$ (nm)	Avg (nm)	SD (nm)	CV (%)
3 x 10^{-4}	0.081	0.079	0.085	0.086	0.083	0.003	10.5
5 x 10^{-4}	0.151	0.148	0.158	0.157	0.153	0.005	7.3
8 x 10^{-3}	0.266	0.279	0.287	0.299	0.282	0.014	4.8
1.7 x 10^{-3}	0.642	0.658	0.673	0.689	0.665	0.021	3.2
3.1 x 10^{-3}	1.342	1.355	1.373	1.381	1.362	0.017	3.8
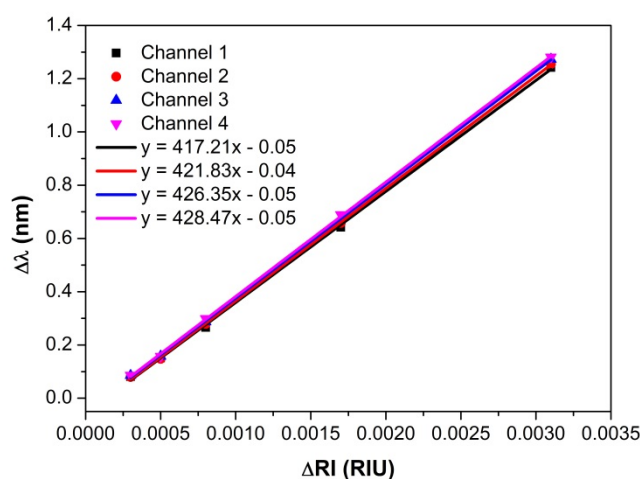
Fig. 4.8 Calibration curves and sensitivity determination for the four channel sensor with the one-input to one-output fluidic design.

4.1.3 Multichannel noise analysis and Limit of Detection estimation

Finally, the LOD of the spatial multiplexed sensor was calculated. As previously described in section 3.1.5, the estimation is done by quantifying the noise level of the system under real-time measurement conditions. A packed multichannel biosensor was clamped to the system setup and connected to the microfluidic system. Later, MilliQ water was flowed at a flow rate of 80 µL/min (20 µL/min flow per channel) for 2-3 hrs.

As seen in Figure 4.9, an average noise standard deviation of 1.09×10^{-3} nm was achieved for all the channels; this value is considered as the noise level of the system. Considering an average sensitivity value of $424\text{nm}\cdot\text{RIU}^{-1}$ for the nanoplasmonic sensor and 3-times the noise standard deviation (3.27×10^{-3} nm) we were able to achieve a LOD in the range of **7.52×10^{-6} RIU** for the spatial multiplexed plasmonic sensor.
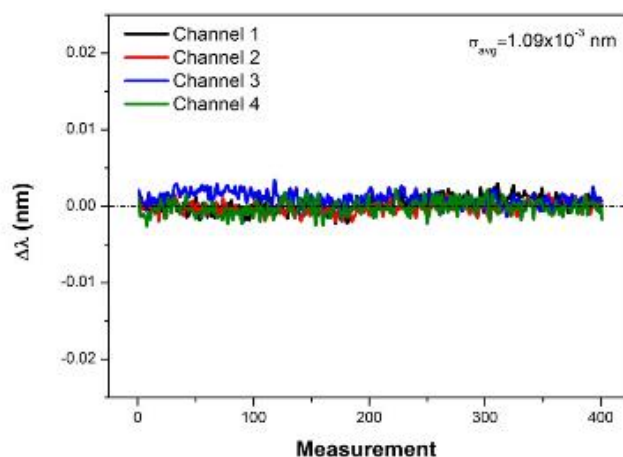
Figure 4.9 Noise level under real-time measurement conditions for the spatial multiplexed system.

The LOD was slightly worse compared to the single channel plasmonic sensor in the miniaturized set-up. The difference in the LOD between the spatial multiplexed and the single channel setup was mainly due to the mechanical noise from the motorized linear stage. To reduce the mechanical noise, it would be necessary to design a one-piece holder to minimize mobile parts and to employ a high precision motorized linear stage. Overall, the sensing performance of the multiplexed sensor is comparable to the current state of the art in SPR sensor[34,43], besides offering a fast and simple fabrication and integration approach.

4.2 Analysis of the C-Reactive protein biomarker

In order to evaluate the multiplexed biosensing capability of the multichannel sensor, we employed the sensor for the direct evaluation of the C-reactive protein

(CRP) biomarker in order to compare the reproducibility between channels. The CRP protein is a well-known and valuable biomarker related to inflammation and infection processes[134,135].

Sepsis is recognized as a systemic inflammatory response due to infection, and it is one of the leading causes of death in critically ill patients[9]. CRP has demonstrated usefulness in identifying patients with sepsis in those who present a systemic inflammatory response[136,137]. The most common method to measure the CRP level is based on ELISA immunoassays, a well-established method, but a time consuming one that requires specialized personnel in a laboratory environment [138-140]. As a consequence, a fast method without the need of specialized personnel in a laboratory environment for the quantification of CRP is highly attractive from a diagnostic and a therapy follow-up perspective. Figure 4.10 summarizes the schematic representation of the proposed immunoassay for CRP biomarker detection, which is similar to that previously described in section 3.2.1 for the anti-GTF2b detection.

1) EDC/NHS
2) Anti-CRP
3) Ethanolamine

Immobilization of Anti-CRP

Target: CRP
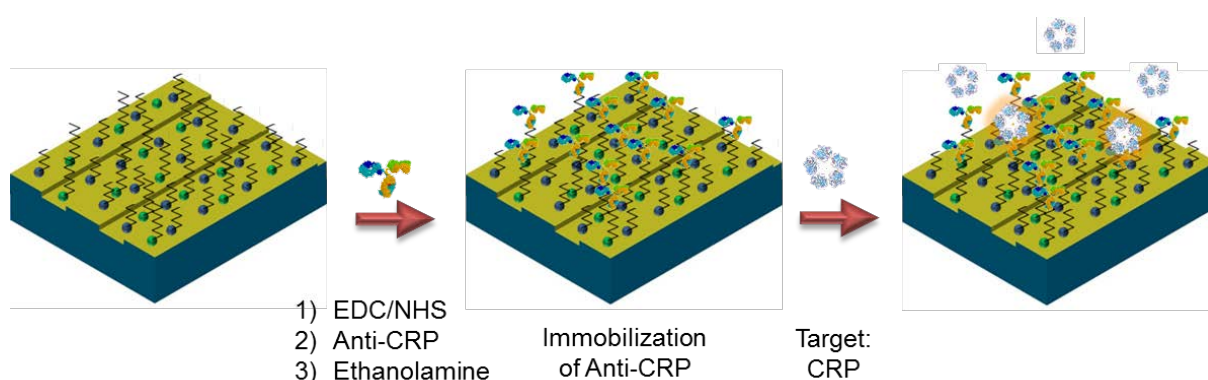
Figure 4.10 Schematic representation of the Anti-CRP antibody immobilization and subsequent protein biomarker detection.

The biofunctionalization of the sensor surface for the protein detection is based on the covalent coupling of the Anti-CRP antibody to a mixed alkanethiol SAM and the subsequent protein detection. The mixed alkanethiol SAM consist of a mixture of 16-mercaptohexadecanoic acid (MHDA) and 11-mercaptoundecanol (MUOH) in a molar ratio 1:5. This specific mixed SAM has been previously evaluated in our group for antibody immobilization, resulting in minimum steric hindrance

effects (occurs when the large size of groups within a molecule prevents chemical reactions that are observed in related molecules with smaller groups), and, therefore, enhancing the target detection[52].

To achieve this, the sensor chips (4.8cm^2 and 100 nm thickness gold layer) were cleaned and activated for surface functionalization by performing consecutive 1 min sonication cycles in ethanol and MilliQ water, drying with N2 stream and finally by placing them in a UV/O3 generator (BioForce Nanoscience, USA) for 20 min. Then a mixed alkanethiol SAM with reactive carboxylic groups was obtained by coating the sensor chips with 1 mM MHDA/MUOH (1:5 ratio) from Sigma–Aldrich (Germany) in ethanol overnight at room temperature. Later, the surface was then rinsed with ethanol and dried with a N$_2$ stream. Prior to the biofunctionalization step, the sensor chips were bonded to the microfluidics and placed in the optical set-up.

The immobilization of the specific monoclonal antibody for CRP was performed *in situ*, and was continuously monitored in real time (see Figure 4.11A). For the activation of the carboxylic groups, a solution of 0.2 M carbodiimide hydrochloride (EDC, Sigma–Aldrich, Germany) /0.05 M N-hydroxysulfosuccinimide (s-NHS, Sigma–Aldrich, Germany) in MES buffer (100 mM pH 5.5) was injected and flowed over the mixed SAM monolayer at 80 μL/min (using H$_2$O as running buffer). Subsequently, a 50 μg/mL anti-CRP (AntibodyBcn, Spain) solution in MES buffer (100 mM pH 5.5) was injected and flowed at 40 μL/min. Finally, a blocking solution (ethanolamine, Sigma–Aldrich, Germany, 1M pH 8.5) was injected for 2 min at 100 μL/min. After immobilization, PBS (10 mM pH 7.5) was settled as a running buffer. For optimization and assessment studies, different concentrations of CRP protein (BBI Solutions, UK) diluted in PBS were flowed over the functionalized surface at 80 μL/min. Regeneration of the biosurface was achieved by injecting 5 mM HCl at 80 μL/min for 2 min. Calibration curves were fitted to a one-site specific binding model. LOD and LOQ (Limit of quantification) were calculated as the concentration corresponding to the blank signal plus three and ten times its standard deviation (SD), respectively.

The detection of CRP at different concentrations (from 100 to 1000 ng/mL) shows a good dose-response and good reproducibility between the channels (see

Figure 4.11B and C). We were able to achieve a LOD of 4.9 ± 0.2 ng/mL (39.2 ± 1.6 pM), and a LOQ of 17.2 ± 0.7 ng/mL (137.8 ± 5.6 pM) respectively (see the calibration curves in Figure 4.8d). The average standard deviation and the corresponding coefficient of variation between the sensing channels for the present bioassay is up to ± 0.2 ng/mL and 4.2%, respectively, in the CRP concentration range evaluated. These results show the possibility of achieving high biosensing reproducibility between the channels. The achieved values are attractive and usefulness for a perspective or early diagnosis of diseases and follow-up care considering that in healthy adults, the normal concentrations of CRP varies between 0.8 µg/mL to 3.0 µg/mL, and when there is pathological disease, the CRP level can rise 10,000-fold up to 500 µg/mL[138,139]. Even more, the achieved LOD is 4-times better than those previously reported by our group using a single-channel nanodisk based plasmonic biosensor (22 ng/mL)[52] showing that the present biosensor is a potential candidate for multichannel biosensing platforms.
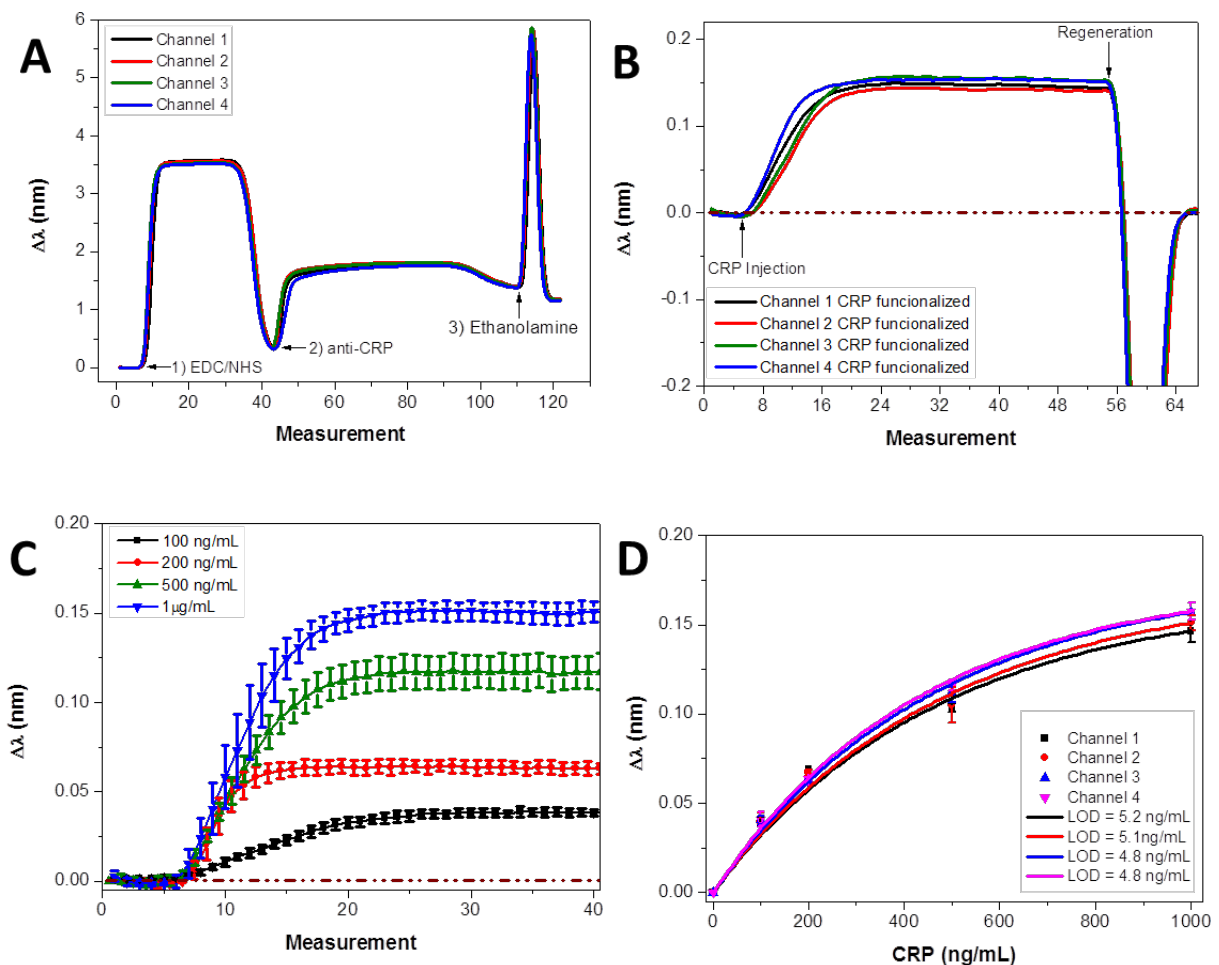
Figure 4.11 Biosensing experiments with the spatial multiplexed biosensor. (a) Real-time sensograms showing the three steps involved in the covalent immobilization of the anti-CRP in the four-channels: (1) activation of carboxylic SAM layer with EDC/NHS, (2) attachment of the antibody and (3) blocking of unreacted active carboxylic groups with an ethanolamine solution. (b) Sensogram obtained for the detection of the target CPR protein at a concentration of 1000 ng/mL in PBS buffer and the subsequent regeneration step. (c) Sensograms showing the detection of the target CRP protein at different concentrations (from 100 to 1000 ng/mL) in PBS. (d) Calibration curve for CRP detection for the spatial multiplexed biosensor. The error bars indicate the standard deviation (SD) from two measurements.

4.2.1 Detection of C reactive protein in urine

Although the clinical quantification of CRP is mainly done in serum samples, there are some reports that suggest that the detection and quantification of CRP in urine can be usefulness for the detection of sepsis and other diseases in humans and animals[140,141]. For that reason, the viability of measuring CRP in undiluted urine was assessed with these multichannel sensors. In this case, as previously described in section 3.2.1 for the detection of GTF2b protein in 10% diluted serum, an additional blocking step with a solution of PLL-PEG (0.5 mg/mL) was added to the biofunctionalization protocol in order to minimize non-specific adsorptions from components present in the urine media.

In a first step, undiluted urine was flowed in order to determine the absence of binding of urine components with the proposed blocking step. As can be observed in Figure 4.12A, the injection of undiluted urine resulted in no background signal ($\Delta\lambda_{SPR}$=0) (see Fig. 4.12A, green), which confirmed the lack of nonspecific binding onto the biofunctionalized and blocked surface. Finally, the same CRP concentrations used for the immunoassay in PBS were spiked in undiluted urine and flowed over the sensor. The regeneration of the biosurface was achieved by injecting 5 mM HCl at 120 µL/min for 2 min.

Sensograms for different CRP concentrations are summarized in Figure 4.12A and the resulting calibration curve (see Figure 4.12B) for CRP in urine showed comparable sensitivity to the one obtained in standard buffer conditions.

The achieved LOD in undiluted urine was 5.3 ± 0.7 ng/mL (42.4 ± 5.6 pM); which is close to the value reached in PBS (LOD= 4.9 ± 0.2 ng/mL). Overall, these results reflect the promising performance of this kind of easy-to-fabricate multiplexed plasmonic sensor and its potential for use in low cost competitive analytical devices for biosensing applications in complex media like undiluted urine.
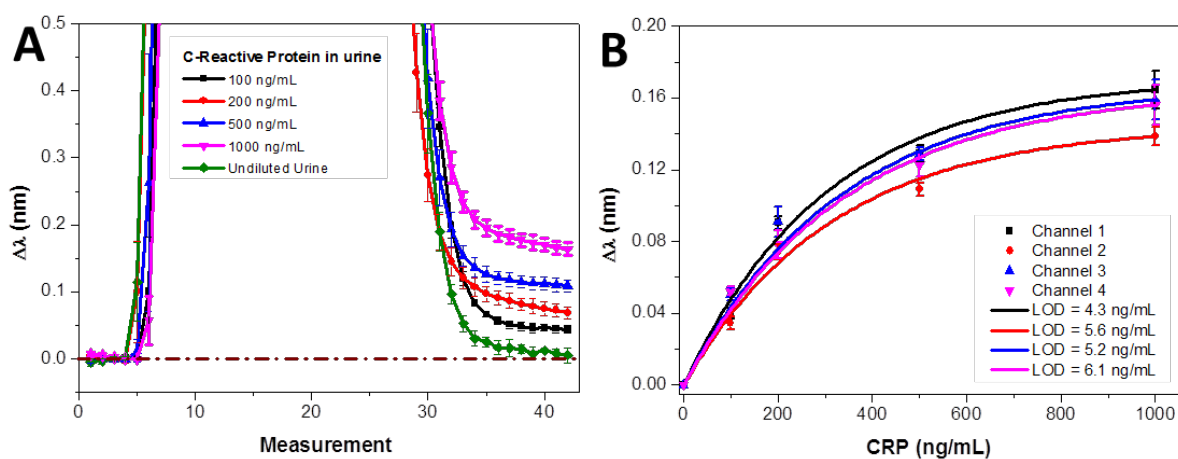
Figure 4.12 Biosensing experiments in undiluted urine for the multiplexed sensor. (b) Sensograms showing the detection of the target CRP protein at different concentrations (from 100 to 1000 ng/mL) in undiluted urine and a negative control of 250 µg/mL BSA in undiluted urine. (c) CRP calibration curves in undiluted urine for the spatial multiplexed biosensor.

4.3 Analysis of the IL-6 protein biomarker

In order to achieve a parallel and multiplexed biosensing assay, we evaluated with a direct assay the presence of the IL6 protein biomarker in a first step to later demonstrate the feasibility of detecting in parallel IL6 and CRP biomarkers under the same bioassay. The IL6 is an interleukin that acts as pro-inflammatory cytokine[141]. It is secreted by T cells and macrophages to stimulate immune response, e.g. during

infection and after trauma, especially burns or other tissue damage leading to inflammation[142]. Similar to CRP, IL-6 is a valuable biomarker associated with inflammation and infection processes[143]; high IL6 levels are correlated with several diseases that range from cancer to sepsis[144,145]; during some diseases, their level can reach up to 305 ng/mL[146]. As in the case of CRP, the most common method to measure IL6 levels is based on ELISA immunoassays with their known disadvantages described before in section 4.2. A method with high specificity and selectivity for the quantification of IL6 and CRP biomarkers is highly attractive from a diagnostic and a therapy follow-up perspective.

The materials and methods for the biofunctionalization methodology were similar to those used for the CRP evaluation. The IL6 and the monoclonal anti-IL6 were purchased from Fitzgerald (USA) and Thermo Scientific (USA), respectively. A concentration of 20 µg/mL anti-IL6 solution in MES buffer (100 mM pH 5.5) was injected and flowed as in the immobilization protocol.

Au nanostructured surfaces were modified by forming a mixed SAM with carboxylic acid, which was further activated and reacted with the specific antibody for IL6. The immobilization was monitored in real time, as can be seen in Figure 4.13A. The detection of IL6 at different concentrations in PBS (from 100 to 1000 ng/mL) shows a good dose-response (see Figure 4.13B). We were able to achieve a LOD of 9.7 ± 0.3 ng/mL (461.9 ± 14.3 pM), and a LOQ of 33.9 ± 0.9 ng/mL (1.6 ± 0.1 nM) respectively (see the calibration curves in Figure 4.13c) with a coefficient of variation between the sensing channels below 4%. While these results show the possibility of achieving high biosensing reproducibility between the channels using two different biomarkers (CRP and IL6), the achieved LOD was in the same order to those reported previously (5.7 ng/mL) by Battaglia[147] et al. (2005) and by Chou[148] (1.2 ng/mL) et al. (2010) by conventional SPR in PBS buffer. To improve the LOD would be necessary to optimize the conditions for the antibody immobilization or considering the use of a second antibody for signal amplification.
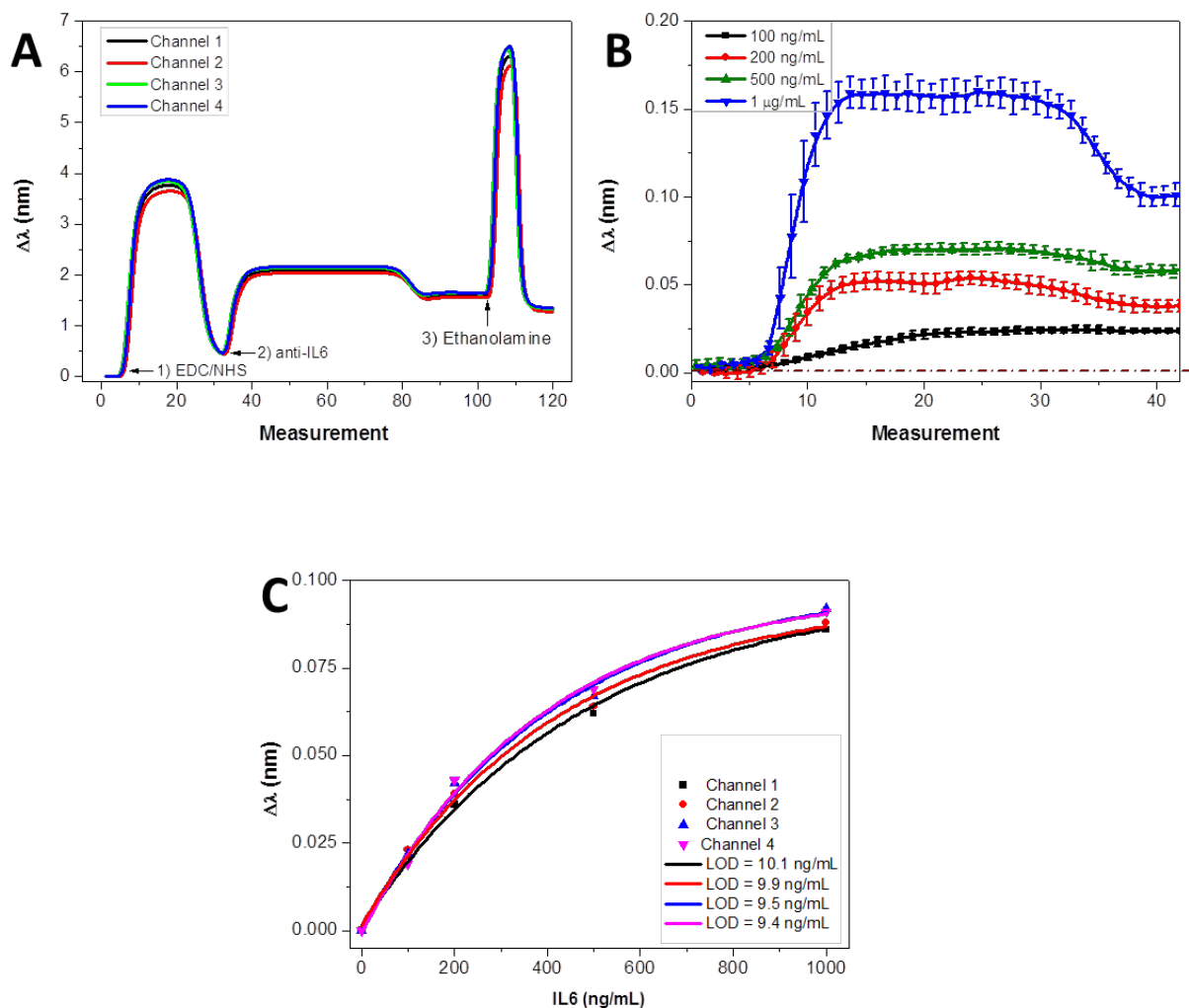
Figure 4.13 Biosensing experiments for the IL6 protein biomarker. (A) Real-time sensograms showing the three steps involved in the covalent immobilization of the specific antibody anti-IL6 in the four-channels: (1) activation of carboxylic SAM layer with EDC/NHS, (2) attachment of the antibody and (3) blocking of unreacted active carboxylic groups with an ethanolamine solution. (B) Sensograms showing the detection of the target IL6 protein at different concentrations (from 100 to 1000 ng/mL) in PBS buffer. (C) Calibration curves for the multichannel IL6 detection.

4.4 Parallel, multiplexed and label-free biosensing of IL6 and CRP biomarkers in buffer

Finally, in order to achieve a parallel and multiplexed biosensing assay, as a first approach and as a proof-of-concept we evaluated with a direct assay the

presence in parallel of IL6 and CRP protein biomarkers under the same bioassay; the dimensions of the channels and the inability to biofunctionalize each channel individually with the proposed microfluidics limit the amount of biomarkers to detect with the selected biofunctionalization strategy.

The biofunctionalization was performed *ex situ*, the main advantages of *ex situ* functionalization compared to *in situ* (in flow) are low reagent consumption and a higher control of immobilization conditions; however, this method has also some disadvantages as it is not possible to monitor the steps of the biofunctionalization process in real time and normally is more time-consuming. The sensor chips were modified to allow the functionalization of two regions individually; to achieve this we created a mask to evaporate with gold two individual zones (0.64 cm^2 each zone), each one for the detection of one protein biomarker (IL6 and CRP). Figure 4.14 illustrates the proposed parallel sensing scheme.
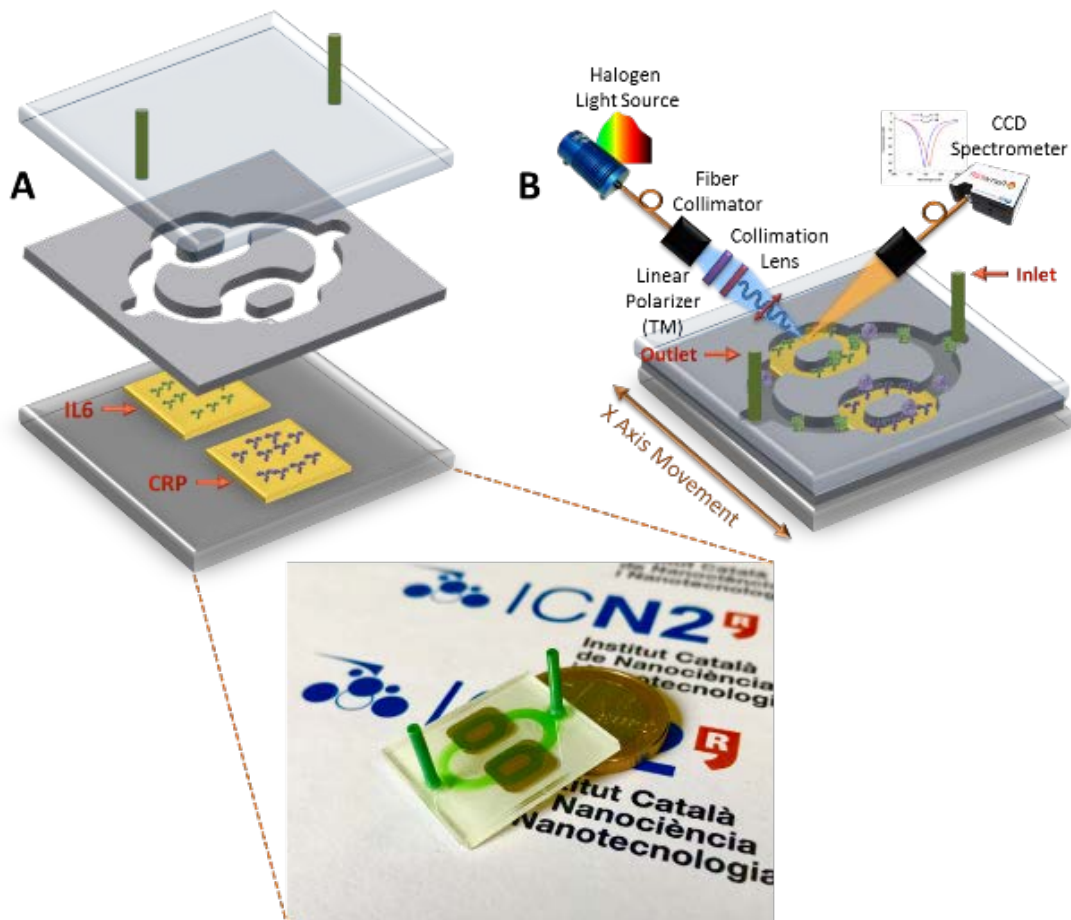
Figure 4.14 Illustration of the proposed detection scheme for parallel biosensing assays. (a) Schematic representation of the parallel multiplexed biosensor and a photograph of the packed biosensor. (b) Schematic representation of the system scheme for a parallel and multiplexed biosensing assay.

The materials and methods for the *ex situ* biofunctionalization methodology are similar to those used for the CRP and IL6 proteins detection *in situ*. The sensor chips were cleaned and activated for surface functionalization by performing consecutive sonication cycles in ethanol and MilliQ water, drying with N_2 stream and finally by placing them in a UV/O_3 generator. An alkanethiol SAM with reactive carboxylic groups was obtained by coating the sensor chips with 1 mM MHDA/MUOH (1:5 ratio) in ethanol overnight at room temperature. The surfaces were then rinsed with ethanol and dried with a N_2 stream.

The immobilization of the specific monoclonal antibodies for Il6 and CRP was performed *ex situ* (see Figure 4.15 left). For the activation of the carboxylic groups, 50 µL of a solution of 0.2 M EDC/0.05 M s-NHS in MES buffer (100 mM pH 5.5) was dropped over the SAM monolayer in the sensing zones and kept reacting for 20 min. Subsequently, the chip was rinsed with MilliQ water and dried with N_2. Later, 50 µL drops of 50 µg/mL anti-CRP and 20 µg/mL anti-IL6 solutions in MES buffer (100 mM pH 5.5) were placed over the activated sensing zones and kept reacting for 120 min. Subsequently, the chip was rinsed with MilliQ water and dried with N_2. Finally, 50 µL drops of a blocking solution (ethanolamine, 1M pH 8.5) were placed over the activated sensing zones and kept reacting for 2 min.

After rinsing the chip with MilliQ water and drying with N_2, the chip was ready for packing (see Figure 4.15 right). The chips were bonded to the microfluidics and placed in the optical platform. To evaluate the cross-interference between the proteins in the immunoreactions, CRP, IL6 and BSA (negative control) proteins diluted in PBS were flowed over the functionalized surface at 80 µL/min. Regeneration of the biosurface was achieved by injecting 5 mM HCl at 80 µL/min for 2 min.
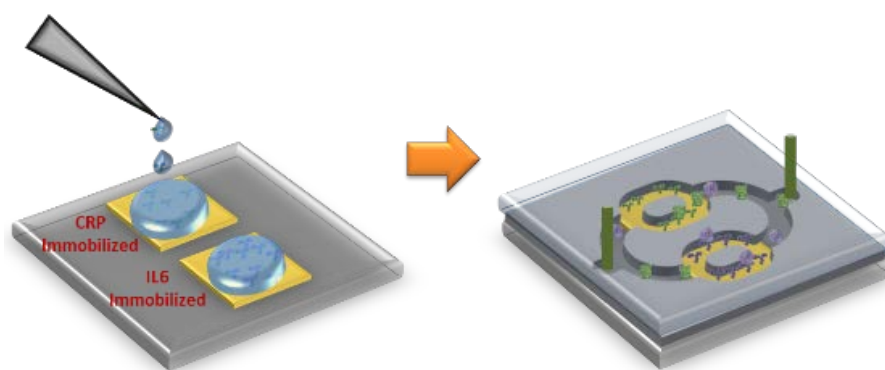
Figure 4.15 Illustration of the proposed *ex situ* biofunctionalization scheme for parallel biosensing assays.

As can be observed in Figure 4.16, after the injection of 1 µg/mL of CRP protein in PBS buffer, the channels functionalized with the anti-CRP (blue and magenta) show a good dose response, meanwhile those functionalized with the anti-IL6 (black and red) resulted in no background ($\Delta\lambda_{SPR}=0$). The same behavior was observed after the injection of 500 ng/mL of IL6 in PBS buffer with no background ($\Delta\lambda_{SPR}=0$) for the channels functionalized with anti-CRP. Finally, no background ($\Delta\lambda_{SPR}=0$) was observed in all the channels after the injection of 5 µg/mL of BSA as a negative control.

These results demonstrate the absence of cross-signals between the channels and the possibility to perform, as a proof-of-concept, parallel and multiplexed plasmonic biosensing assays with the proposed sensor and the designed microfluidic splitter on-chip, thereby greatly simplifying the microfluidic instrumentation normally required for multiplexing evaluations.
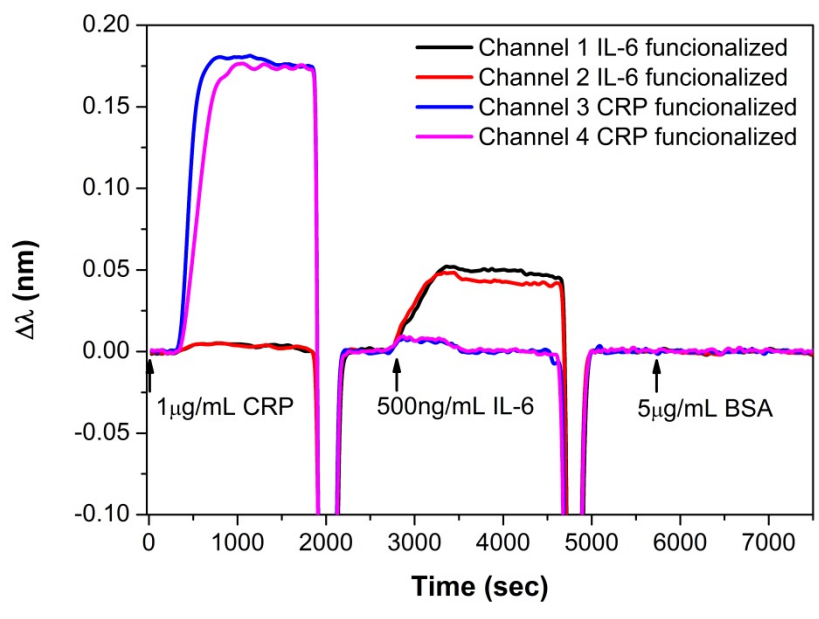
Figure 4.16 Parallel biosensing experiments for CRP and IL6 biomarkers.

Chapter 5. Multilayer Au/Ag Biosensor

This chapter comprises the development of novel Gold/Silver/Gold trilayer Blu-ray disc-based plasmonic nanostructures. For this purpose, FDTD simulations were performed for a trilayer sensor. Later, we describe the fabrication scheme, and the optical and morphological characterization of the sensors. The theoretical sensing improvement was evaluated in two steps: first we evaluated the chemical stability of the trilayer sensor under high oxidative conditions (UV/O3 oxidation and a high salt content media) commonly used in biosensing assays. In a second step, we evaluated the improvement for label-free biosensing of the proposed trilayer sensor *versus* a gold monolayer sensor by evaluating the presence of CRP biomarker in buffer for both sensors. Finally, we evaluated the feasibility of direct detection in a complex biological matrix such as urine.

5.1 Fundamentals of Silver in Plasmonic Biosensors

Plasmonic biosensing on metallic nanostructures mainly is based on gold nanostructures due to their high plasmonic performance and excellent chemical stability of the gold metal[149]. However, due to its dielectric properties, silver has the highest plasmonic activity of all noble metals when used to build nanostructures and is also more economically attractive[150]. Silver-based plasmonic sensors can exhibit higher sensitivity and a sharper reflectivity spectrum than those of gold film and consequently the limit of detection or resolution is significantly improved when silver film is used as the metal film[151]. The main reason for this improvement is due to the larger evanescent field decay length and field enhancement factor for silver-based plasmonic structures (see Figure 5.1) owing to a lower dielectric constant compared with gold[151].
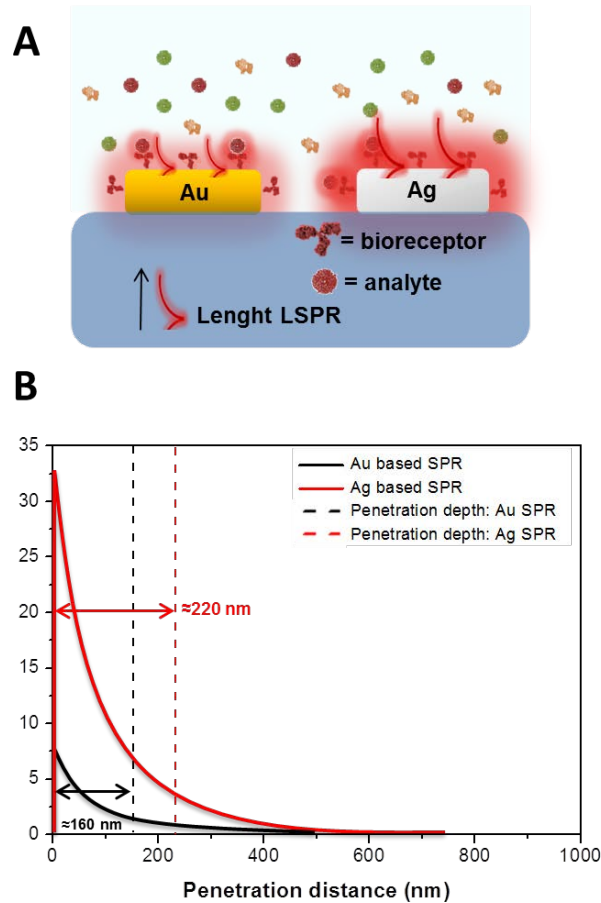
Figure 5.1 (A) Schematic representation of the differences in the evanescent decay length and field enhancement between a silver nanostructure-based biosensor (gold) and a gold nanostructure-based biosensor (left). (B) Comparison of the field enhancement factor versus the penetration distance for an Au and Ag conventional SPR sensor.

However, the main obstacles faced by silver-based nanostructures when dealing with different plasmonic applications are related to the low chemical stability and poor wettability of the silver. Besides the problem oxidation, the deposited Ag atoms have greater tendency to bind to each other rather than to the substrate atoms, favoring three dimensional island growths and consequently an increase in surface roughness that can diminish the sensing performance[150-152].

In order to overcome these challenges two main approaches have been explored to be able to generate chemically stable and flat silver plasmonic films on dielectric substrates: 1) the addition of a protective surface layer (i.e. self-assembled monolayers (SAM)[153], oxides and other metals[154]); and 2) the use of a nucleation

layer (i.e. germanium[151], chromium + gold[150] and polymers[157]). The addition of a protective thin gold film (Ag/Au bilayer system) can increase chemical stability. However, under certain oxidative environments, such as saline solutions, chemical stability and reproducibility for long term use can also be affected. This can be partly related to low wettability (which implies high roughness) of silver on dielectric substrates and the mismatch adhesion of silver with different materials[150,154].

To overcome these difficulties, the use of nucleation layers has also been proposed, but most of the materials employed (i.e. germanium, titanium, chromium) increase ohmic plasmon losses, thereby diminishing the final sensing performance [156]. Recently, another approach using a thin gold nucleation layer between a chromium adhesion layer and the upper silver layer has been demonstrated, successfully generating flat silver plasmonic films with improved chemical stability on glass substrates creating a four-layer system (Cr/Au/Ag/Au) [154].

Finally, the use of polymer-based substrates can increase the potential application of plasmonic nanostructures, as the flexibility these materials can confer expand their use, for example, enabling the direct integration of sensors in the human body, or for solar energy harvesting, among others[157,158]. Considering that efficient deposition of thin gold films in commercial BDs can be accomplished without the need of an adhesion layer (i.e. germanium, chromium, titanium) that can negatively affect the plasmonic performance in different ways[156], it could be possible to achieve flexible and chemical stable silver-based plasmonic biosensors using a trilayer approach.

5.1.1 Design Considerations and Finite-Difference Time-Domain Simulations

As mentioned before, by using a trilayer approach, we can improve the chemical stability and sensing performance in silver-based plasmonic biosensors. In Figure 5.2 we present a schematic representation of the structural geometry for FDTD simulations. The simulation parameters were the same as previously used to model the BD-based gold nanostructures: we calculated the reflectivity of a TM

polarized broadband light source in the visible range (400 to 800 nm) impinging the nanostructured substrate for a 70⁰ fixed incident angle and the electromagnetic field distribution across using commercial software (Lumerical Inc., FDTD solution, Canada).

A nanostructured polycarbonate substrate (n= 1.58) with the structural parameters of the Blu-ray discs (i.e. a slit period of 320 nm, slit width of 160 nm and a height of 20 nm) and H_2O as the sensing medium (n=1.33) were used in the simulations. To fix the thickness of the Au/Ag/Au layers for the simulation, the following parameters were considered: according to Guner[97], et al. (2017) above 100 nm of metal thickness no significant change in the plasmonic reflectance spectra was observed at normal light incidence. For the top gold layer, according to previous results by Wang[154] et al. (2014) of flat Au/Ag layers in glass substrates, a gold top layer of around 10-15 nm can highly improve chemical stability on Au/Ag plasmonic sensors, and for the bottom adhesion layer, a layer around 2 nm can improve the adhesion. Considering these, 2 nm Au/ 83 nm Ag/15 nm Au (100 nm) thickness layers were simulated.

Periodic boundary conditions were used in x and y axis, and a perfect matched layers (PML) approach was used in the z axis, with a uniform mesh size of 2 nm in all axis. The optical constants of the polycarbonate, gold and silver were taken from Sultanova[108] et al. (2009) and Johnson and Christy[109] (1972), respectively, in the range from 400 nm to 800 nm.
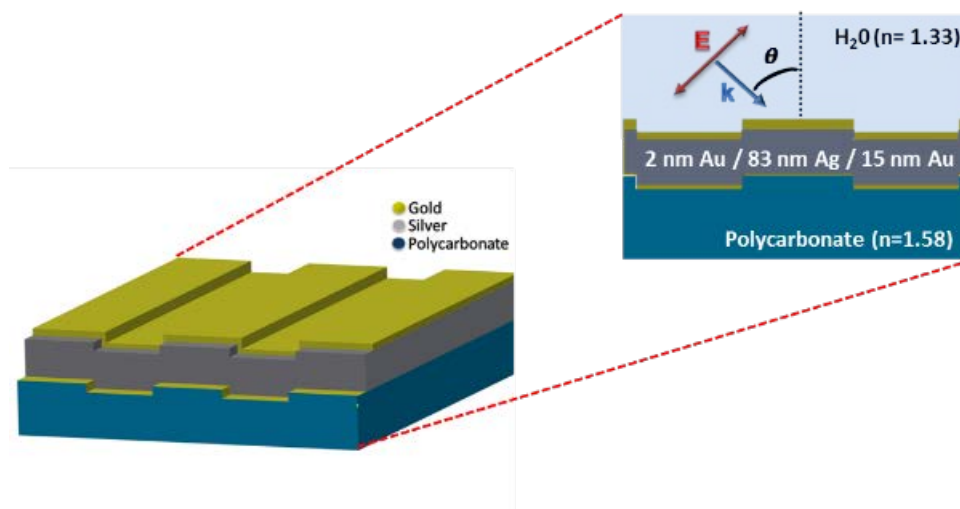
Figure 5.2 Schematic representation of the structural and parameters for the FDTD reflectance simulations of the BD-based Au/Ag/Au trilayer nanostructures.

The FDTD simulation results for the 100 nm gold metal layer thickness and for the total 100 nm metal trilayer thickness under a TM-polarization are present in the Figure 5.3. As can be observed, in Figure 5.3 (left), there is a clear decrease in the FWHM with a narrower plasmonic resonance line width for the reflectance spectra for the 100 nm thickness trilayer sensor compared with the reflectance spectra of the 100 nm gold thickness monolayer sensor. Additionally, by analyzing the optical field distributions calculated from FDTD simulations at the peak resonance wavelength (see Figure 5.3. right) significant differences in the electric field distributions can be observed for the Au monolayer and the Au/Ag/Au trilayer, respectively. The higher plasmonic activity owing to the addition of a silver layer in a Au/Ag/Au configuration is noticeable with an increase in the intensity of the optical fields compared with single Au layers[149,156].
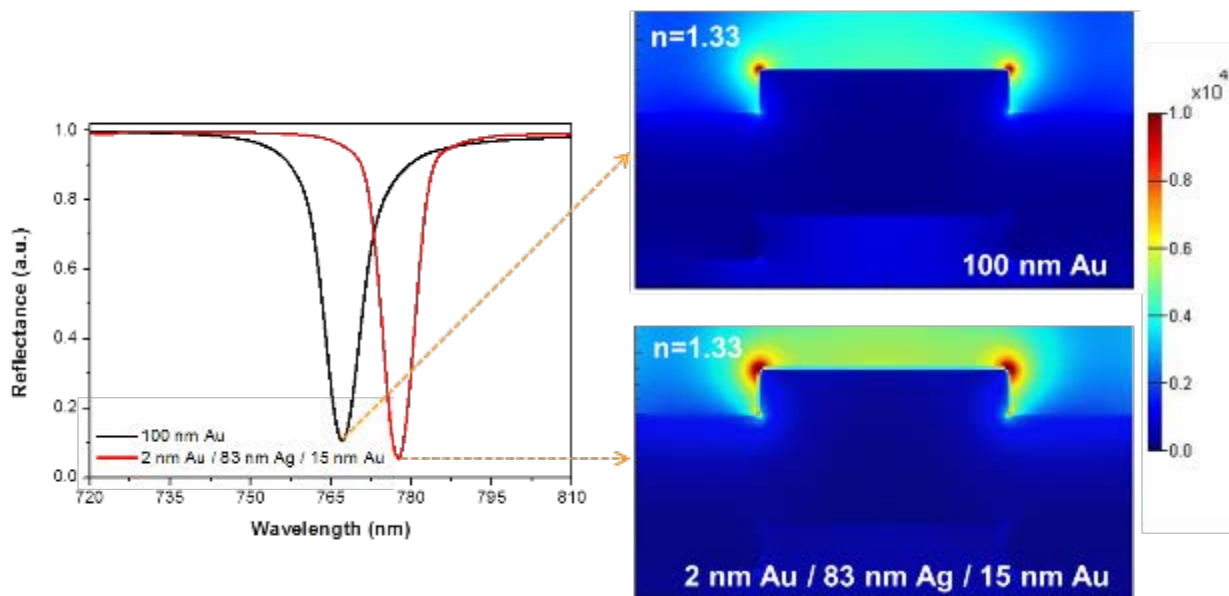
Figure 5.3 FDTD Simulations of the proposed Au monolayer and Au/Ag/Au trilayer metallic nanostructures. The simulated optical reflectance spectra under TM-polarization for the Au monolayer and Au/Ag/Au trilayer film (Left). Simulated electric field distribution for the Au monolayer and Au/Ag/Au trilayer film (Right).

5.2 Fabrication and characterization of the trilayer sensors

Obtaining plasmonic sensor chips from BDs involves a simple fabrication process, based on the coating of a metallic layer on the nanostructured polycarbonate substrate. For the fabrication of the Au/Ag/Au trilayer plasmonic chips, the only modification to the fabrication described in section 2.2.1 was the deposition rate: 0.7 Å/s for gold and 0.8 Å/s for silver. These values were selected to improve the control of the layer thickness. For the adhesion/nucleation layer, different Au layer thicknesses were evaluated (from 0 nm to 5 nm), which seems to be sufficient to improve the adhesion of the silver layer while minimizing alterations to the plasmonic propagation due to a strong optical absorption of the adhesion/nucleation layer[159]. On the other hand, different thicknesses of top the Au layer (5 nm to 25 nm) were evaluated to improve the chemical stability of the sensor under high oxidative media (UV/O3 oxidation and a high salt content media) commonly used in biosensing assays. For comparison, we also fabricated Ag/Au bilayer plasmonic sensors without the Au nucleation layer.

5.2.1 Structural and Chemical Characterization of the Multilayer Sensors

In a first step, the influence of the gold adhesion/nucleation layer on wettability and as a consequence on surface roughness of the plasmonic sensors was evaluated. The bare and the multilayered nanostructured surfaces were first characterized by atomic force microscopy (AFM). The surface morphology and root-mean-square (rms) surface roughness of the plasmonic chips were characterized using an AFM system (Digital Instruments Inc., MM-AFM2, USA). The samples were scanned over a 2.25 μm^2 at a tip velocity of 1 $\mu m/min$ at contact mode.

Figure 5.4 shows the surface roughness and the profile. Surface roughness values obtained in root-mean-square (RMS) were 0.21, 0.36, 1.29 and 0.65 nm for bare Blu-ray, Au, Ag/Au and Au/Ag/Au plasmonic sensors, respectively. For the Au/Ag/Au sensor, a 2 nm Au nucleation layer increases the adhesion of Ag to the substrate, reducing the stratification and therefore decreasing the surface roughness

compared with the Ag/Au sensor (0.44 nm vs 1.08 nm, by subtracting the surface roughness of the bare nanostructured substrate)[156].

The roughness value for the Au/Ag/Au plasmonic film (0.44 nm) was lower than the one previously reported for Cr/Au/Ag/Au[156] and Ge/Ag[152] multilayer plasmonic films, all of them being fabricated on flat glass substrates. These results emphasize that also for polymeric substrates; ultrasmooth plasmonic Ag based nanostructures can be fabricated without using adhesion/nucleation materials, which significantly increase ohmic plasmon losses (i.e. germanium, chromium, titanium)[156].

Blu-ray based substrate

$\sigma_{RMS}=0.21$ nm

Monolayer Au

$\sigma_{RMS}=0.36$ nm

Bilayer Au/Ag

$\sigma_{RMS}=1.29$ nm

Trilayer Au/Ag/Au

$\sigma_{RMS}=0.65$ nm
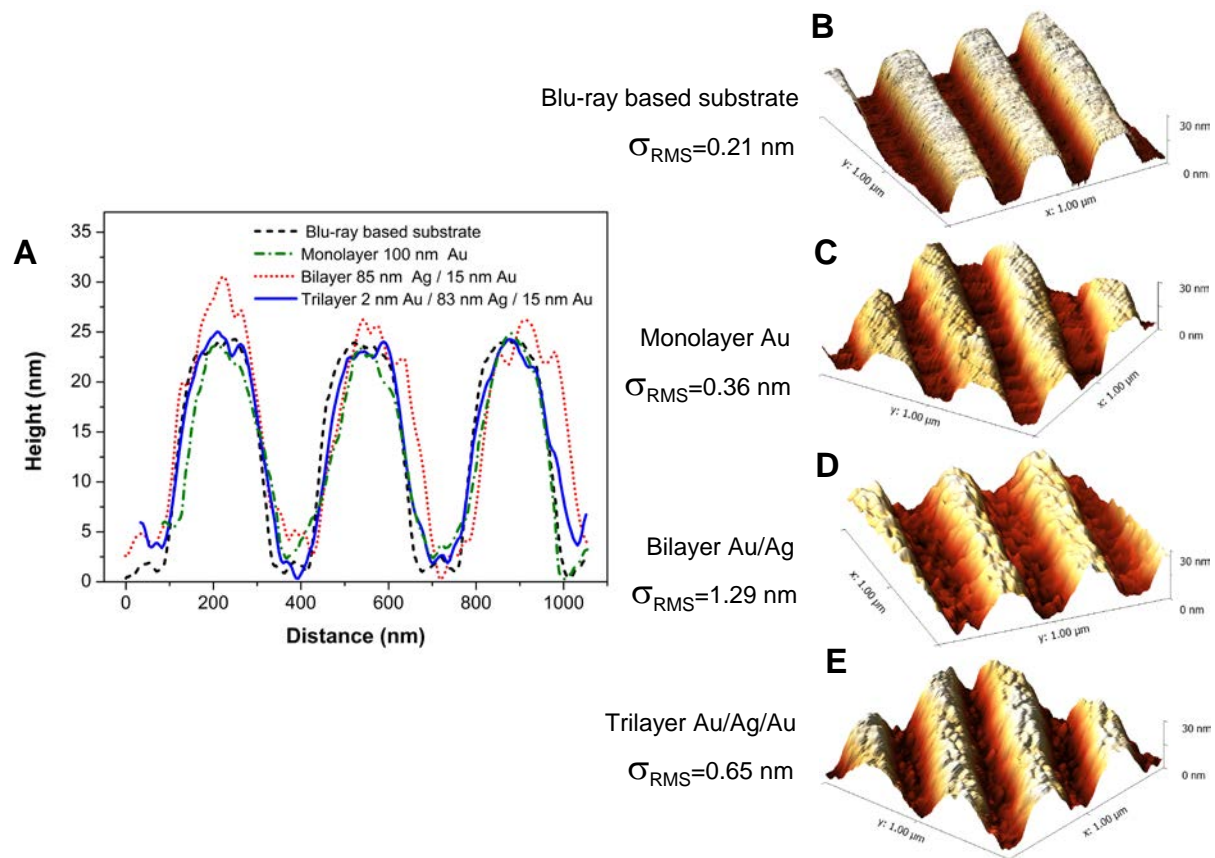
Figure 5.4 AFM characterization: (A) AFM section analysis of four different layers of Blu-ray based substrate: bare Blu-ray substrate, the100 nm Au monolayer substrate, the 85 nm Ag /15 nm Au bilayer substrate and the 2 nm Au / 83 nm Ag /15 nm Au trilayer substrate. AFM images of four different layers of Blu-ray based substrate: (B) the bare Blu-ray based substrate, (C) the 100 nm Au monolayer substrate. (D) The 85 nm Ag /15 nm Au bilayer substrate and the (E) 2 nm Au / 83 nm Ag /15 nm Au trilayer substrate.

SEM images were obtained using a field emission scanning electron microscope (FEI Co., Quanta 650, USA) at a HV of 20kV to improve contrast of the images. Additionally, under the same characterization, energy-dispersive X-ray spectroscopy (EDS) spectra were collected for the elemental analysis and chemical characterization of the multilayer sensors, the spectra were collected for energy dispersion up to 8 keV.

Figure 5.5 shows the EDS spectra of the 5 nm Ag /15 nm Au bilayer substrate and the 2 nm Au / 83 nm Ag /15 nm Au trilayer substrate. The spectra showed, as expected, a chemical composition mainly of C and O from the polycarbonate substrate, and Au and Ag from the metallic multilayer. The total intensity of the energy dispersion peaks for the Au element was slightly higher in the trilayer sensor compared with the bilayer sensor due to the additional nucleation layer. The SEM images (insert Figure 5.5) show a lower roughness for the trilayer sensor in concordance with the images obtained by AFM.
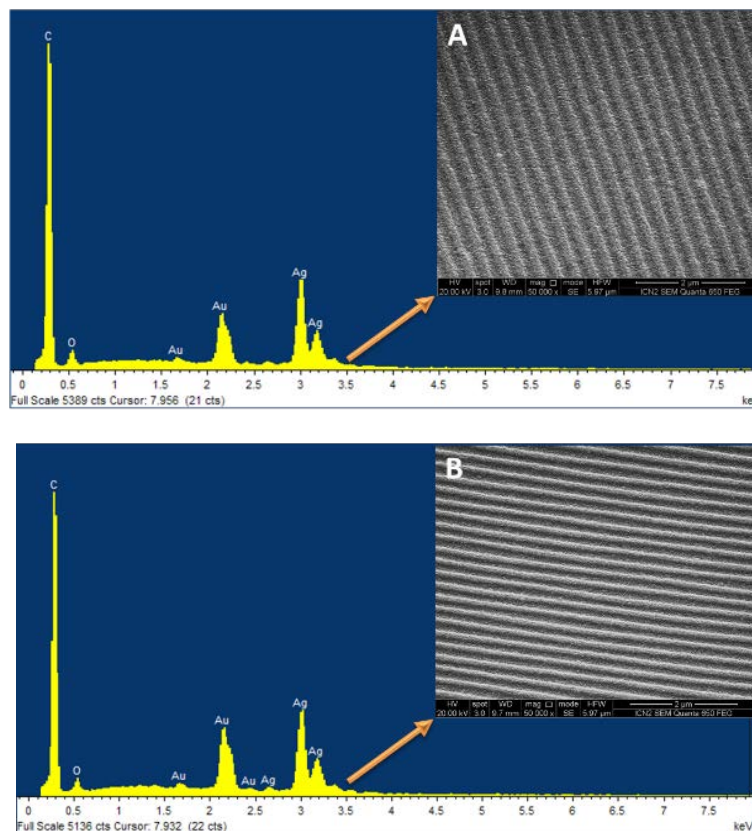
Figure 5.5 SEM and EDS characterization. (A) EDS spectra of the 5 nm Ag /15 nm Au bilayer substrate. (B) EDS spectra of the 5 nm Ag /15 nm Au bilayer substrate. The inserts show the SEM images of the substrates.

5.2.2 Optical Characterization of the Multilayer Sensors

The trilayer Au/Ag/Au plasmonic sensor chip was also optically characterized with reflectance measurements, collecting spectra at different angles of incident light (30º-70º) with a TM polarized broadband light in air (n=1.00) and water (n=1.33) as was previously described for the single gold layer plasmonic sensor in section 3.1 (see Figure 5.6A). The observed shift in the λ_{SPR} to higher wavelengths and the narrower resonant linewidths with high incident angles are in good agreement with the equation that describes the plasmonic effect by the grating coupling method, and with the increase of the light trapping/confinement effect as previously described in section 2.1.1 and 2.1.2.

The optical characterization results were contrasted with those calculated from FDTD simulations. As can be observed in Figure 5.6A, there is a good agreement between the calculated and the experimental reflectance spectra, with a narrower resonant linewidth for the Au/Ag/Au substrate compared with the Au substrate. As previously discussed, the dielectric properties of Ag provide nanostructures with higher plasmon field enhancements and narrower FWHM spectra compared with those of only a Au monolayer.
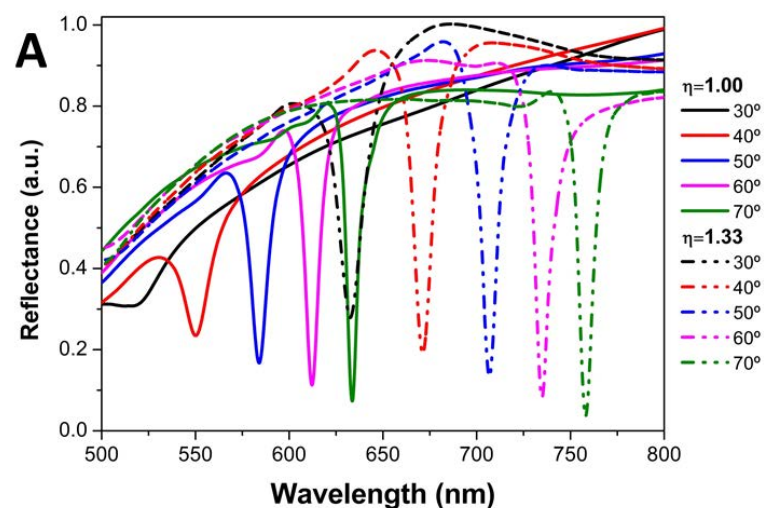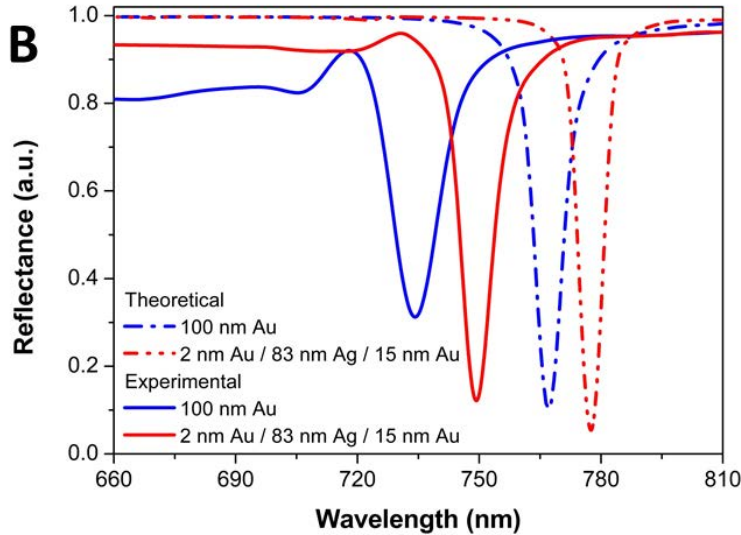
Figure 5.6 Optical characterization of the proposed Au/Ag/Au trilayer plasmonic sensor. (A) Variation of reflectance spectra in air (n=1.00 RIU) and water (n=1.33 RIU) of trilayer (2 nm Au/83 nm Ag/15 nm Au) plasmonic sensor varying oblique light incidence angle. (B) Evaluated and simulated optical reflectance spectra under TM-polarized light for the fabricated Au monolayer and Au/Ag/Au trilayer plasmonic nanostructures.

The performance of the trilayer plasmonic device for sensing applications was also evaluated with different glycerol solutions (ranging from a Δn between 3×10^{-4} and 11.1×10^{-3} RIU). The main parameters were extracted after injection of the different solutions: bulk sensitivity, FWHM and the resultant FOM at different angles of incident light. The measurements were also done in real time, keeping a constant flow of H_2O (30 µL/min) as a running buffer. An enhanced sensor response to the different RI glycerol solutions is observed for the Au/Ag/Au trilayer sensor compared with the Au monolayer sensor (see Figure 5.7A). The Au/Ag/Au sensors reach a sensitivity up to 476 nm·RIU^{-1} (see Figure 5.7B), and a FWHM up to ≈ 7 nm (see Figure 5.7C) allowing to achieve a FOM up to ≈ 69 RIU^{-1} (see Figure 5.7D). The achieved FOM is higher to the previously reported by Choi *et al.* (2016) for DVD based plasmonic sensors (62.5 RIU^{-1}).

The results were compared to those previously obtained for the Au plasmonic sensor. The Au/Ag/Au plasmonic sensor resulted in better overall performance compared with Au layered plasmonic sensors at the entire incident angle tested, with 70° being the optimal one. Although the enhancement in sensitivity was around 12%

(bulk sensitivity of 476 nm·RIU^{-1} *vs* 425 nm·RIU^{-1} in Au), the narrowing of the peak (with a FWHM reduced approximately 57%, from 12 nm to ≈ 7 nm) led to an enhancement of the FOM of a factor of two (from 34.9 to 69.2 RIU^{-1} for the trilayer sensor).
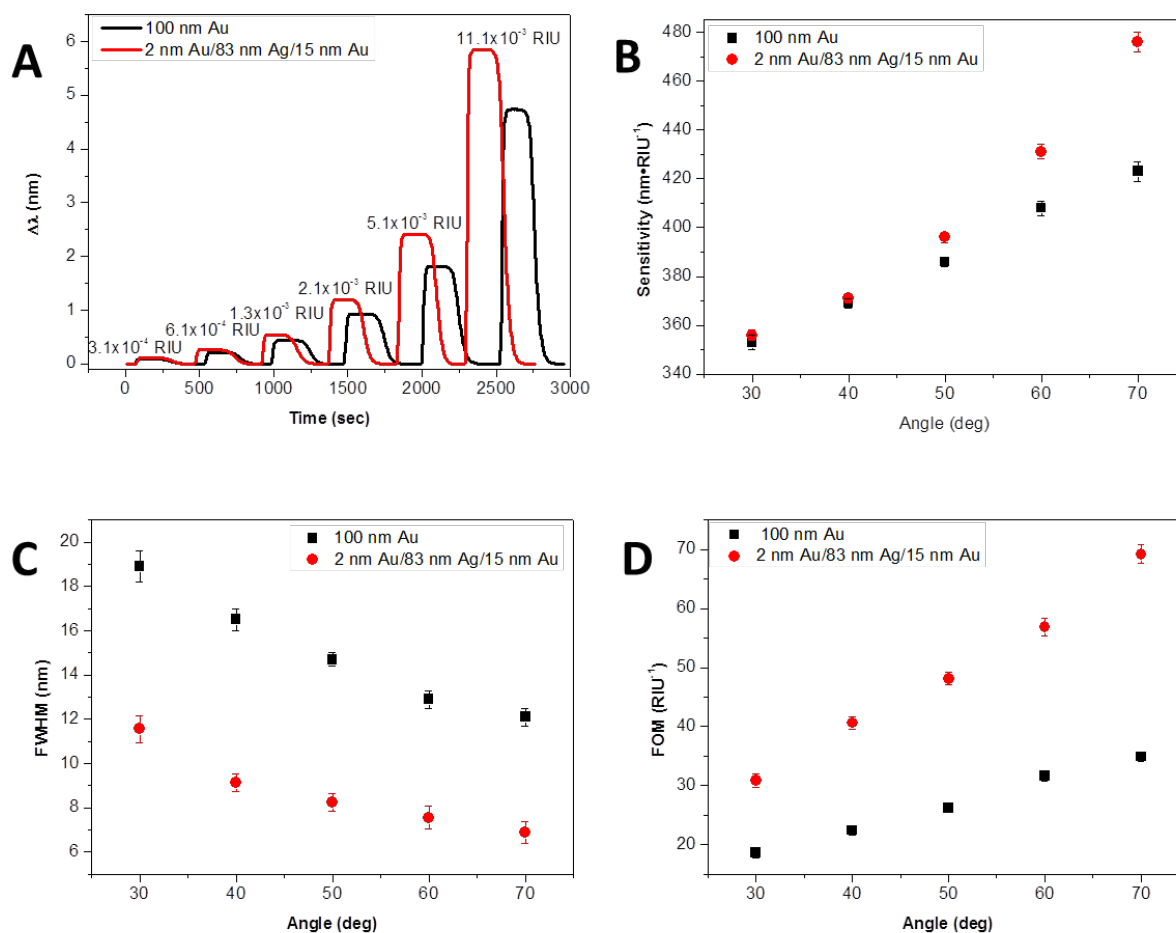
Figure 5.7 (A) Real-time sensograms of different solutions of glycerol for the Au and the Au/Ag/Au sensor, variation of the bulk sensitivity (B), FWHM (C) and FOM (D) respectively as function of the angle of the incidence light for the Au monolayer and Au/Ag/Au trilayer plasmonic devices; the error bar indicates the standard deviation of three measurements.

Finally, it was evaluated the influence of the adhesion/nucleation layer thickness on the sensing performance of the plasmonic sensors. The optical effect of different adhesion/nucleation Au layer thicknesses (0, 2 and 5 nm) was evaluated by estimating the sensitivity of the sensor. Different RI solutions (i.e. glycerol solutions between 4.2 mM and 68 mM) were injected. Sensitivities of 477 nm·RIU^{-1}, 475

nm·RIU^{-1} and 440 nm·RIU^{-1} were estimated for the bilayer (0 nm), the 2 nm adhesion trilayer, and the 5 nm trilayer sensors, respectively.

As shown in Figure 5.8, while there is no difference in the response of the trilayer sensor when the adhesion layer thickness is up to 2 nm (477 nm·RIU^{-1} for a 0 nm Au adhesion layer *vs* 475 nm·RIU^{-1} for a 2 nm Au adhesion layer), there is a significant decrease in the response of the trilayer sensor when the Au adhesion layer thickness is increased from 2 to 5nm. This decrease in the sensor response implies that the sensitivity of the sensor decreases with thick adhesion layers (475 nm·RIU^{-1} for a 2 nm Au adhesion layer *vs* 440 nm·RIU^{-1} for a 5 nm Au adhesion layer); a thicker Au adhesion layer can affect the plasmonic propagation due to a strong optical absorption[159] as well as happens with other adhesion/nucleation materials (i.e. Ge, Cr and Ti)[154,156].
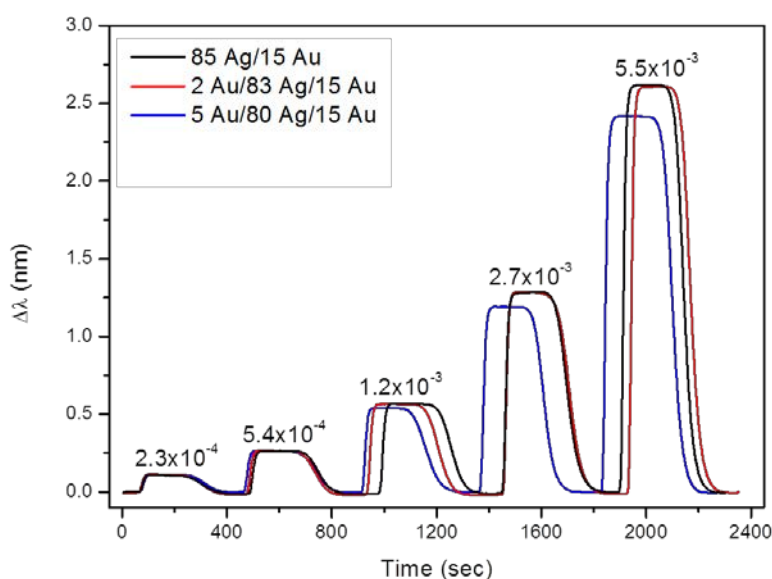
Figure 5.8. Real-time changes in the resonance peak position (λ_{SPP}) for different solutions of glycerol (angle of light incidence= 70⁰) for three multilayer structures with different adhesion/nucleation Au layer thicknesses: (black) no adhesion layer, (red) 2 nm Au and (blue) 5 nm Au.

5.2.3 Chemical Stability of the Multilayer Sensors

As we mentioned in section 5.1, the main obstacle faced by silver-based nanostructures for biosensing applications is related to the low chemical stability of silver; it has been shown previously that the addition of a protective thin gold layer can improve its chemical stability. As a consequence, the effect of the protective Au layer thickness in the chemical stability of the trilayer plasmonic sensor was evaluated under high oxidative conditions (UV/O$_3$ oxidation and a high salt content media) commonly used in biosensing assays and compared with the stability of the bilayer sensors as a reference (no Au nucleation/adhesion layer).

First, trilayer sensors with three different top Au layer thicknesses (5, 15 and 25 nm, respectively) were placed in a UV/O$_3$ generator (BioForce Nanoscience, USA) for 10 min. As shown in Figure 5.9 top, Au layer thickness ≥15 nm provides a significant protection against oxidation. Furthermore, the lack of the 2 nm nucleation layer (i.e. bilayer sensors) resulted in a significant degradation even with a top layer of 15 nm, which clearly demonstrates the improvement in chemical stability by including this layer in the plasmonic sensors. This improvement can be correlated with the higher wettability and adhesion to the substrate of silver with the inclusion of the gold nucleation layer.
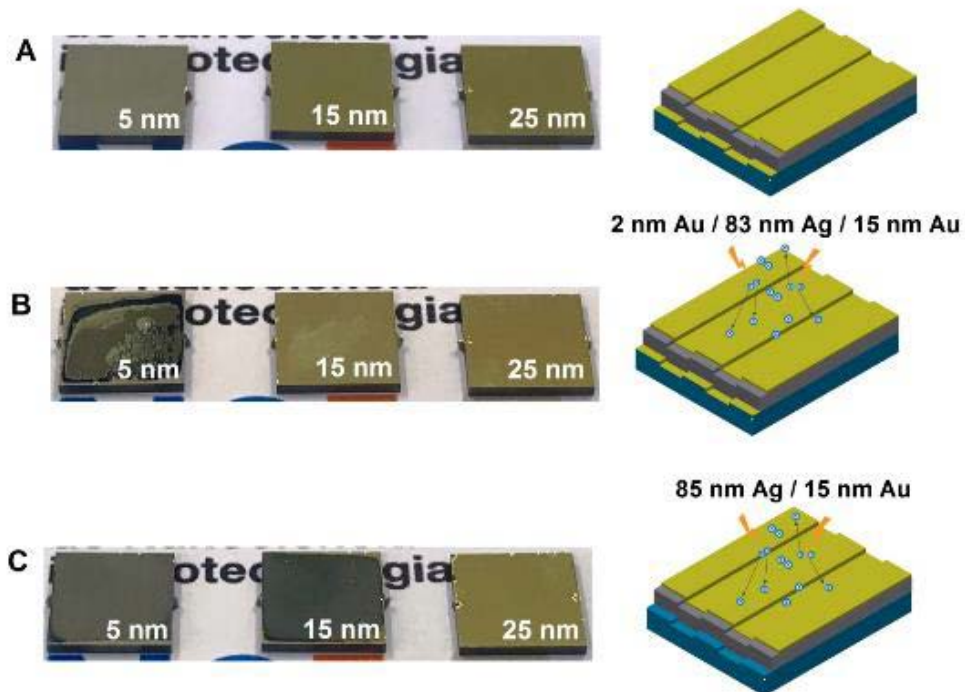
Figure 5.9 UV/O$_3$ effect on multilayer sensors with different top Au layer thicknesses (5, 15 and 25 nm, respectively). (a) Trilayer samples with a 2 nm adhesion/nucleation Au before UV/O3 treatment. (b) Trilayer samples with a 2 nm adhesion/nucleation Au layer thickness after UV/O3 treatment (10 min). (c) Reference bilayer samples (without adhesion/nucleation Au layer) after UV/O3 treatment (10 min).

Finally, the stability under aqueous oxidative media was evaluated by integrating the sensors with the flow cell and performing real-time tracking of the λ_{SPR}. A high salt content solution (PBS 100 mM with 1.4 M NaCl) was continuously flowed at 5 µL/min for more than 120 min.

As can be observed in Figure 5.9 there is a steady baseline ($\Delta\lambda_{SPR}$) for the trilayer (2 nm Au / 83 nm Ag / 15 nm Au) sensor as in the case of the single Au layer sensor, which confirms its chemical stability over time. Under the same experimental conditions, the bilayer sensor (85 nm Ag / 15 nm Au) suffered a pronounced change in the $\Delta\lambda_{SPR}$. As expected, the improvement in wettability and as a consequence, the decrease of the roughness of the silver using the thin Au adhesion/nucleation layer, is correlated with the improved chemical stability of the Au/Ag/Au substrate compared with its Ag/Au counterpart[156].
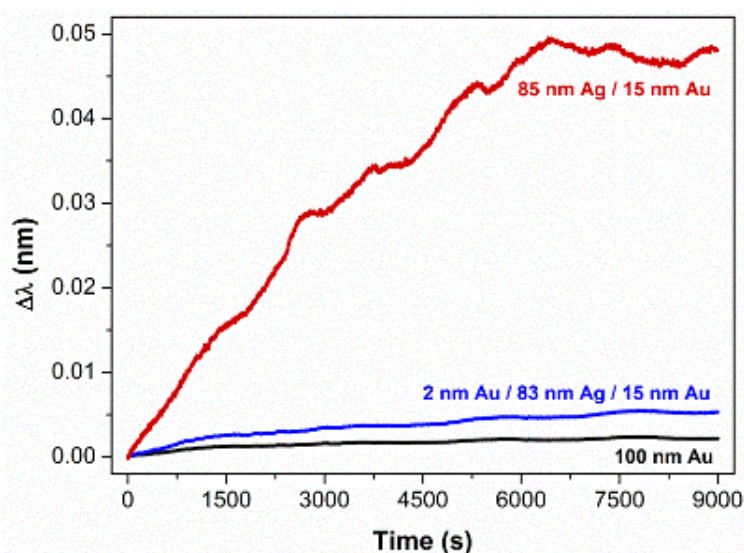
Figure 5.9 Real-time changes in the resonance peak position (λ_{SPP}) in a continuous flow of highly concentrated PBS (100 mM with 1.4 M NaCl) for the three different structures: Au monolayer, Ag/Au bilayer and Au/Ag/Au trilayer.

5.3 Comparison of the biosensing performance

To evaluate the biosensing performance of the Au/Ag/Au plasmonic sensor, a direct assay based on the attachment of specific antibodies and the detection of the corresponding target protein was performed. The selected protein, CRP is a well-known and valuable biomarker associated with inflammation and infection processes as previously described in section 4.2.1. The biosensing assay was performed for Au/Ag/Au trilayer and the Au monolayer sensors to compare their biosensing performance using the single channel experimental set-up

The materials and methods for the biofunctionalization methodology were similar to those previously described in section 4.2.1 for the multichannel detection of CRP. The sensor chips were cleaned and activated following the previous protocol for surface functionalization by performing consecutive 1 min sonication cycles in ethanol and MilliQ water, drying with N_2 stream and finally by placing them in a UV/O$_3$ generator (BioForce Nanoscience, USA) for 20 min. An alkanethiol SAM with reactive carboxylic groups was obtained by coating the sensor chips with 1 mM MHDA/MUOH (1:5 ratio) in ethanol overnight at room temperature. The surfaces were then rinsed with ethanol and dried with a N_2 stream. Prior to the biofunctionalization step, the chips were bonded to the microfluidics and placed in the optical platform.

The immobilization of the specific monoclonal antibody for CRP was performed *in situ*, and was continuously monitored in real time to compare the plasmonic response of the Au/Ag/Au and the Au sensors during the biointeractions. For the activation of the carboxylic groups, a solution of 0.2 M EDC/0.05 M s-NHS in MES buffer (100 mM pH 5.5) was injected and flowed over the SAM monolayer at 20 µL/min (using H_2O as running buffer). Subsequently, a 50 µg/mL anti-CRP solution in MES buffer (100 mM pH 5.5) was injected and flowed at 10 µL/min. Finally, a blocking solution (ethanolamine, 1M pH 8.5) was injected for 2 min at 25 µL/min. After immobilization, PBS (10 mM pH 7.5) was settled as running buffer. For optimization and assessment studies, different concentrations of CRP protein diluted in PBS were flowed over the functionalized surface at 20 µL/min. Regeneration of

the biosurface was achieved by injecting 5 mM HCl at 20 µL/min for 2 min. Calibration curves were fitted to a one-site specific binding model. LOD and LOQ were calculated as the concentration corresponding to the blank signal plus three and ten times the SD, respectively.

Au/Ag/Au and Au nanostructured surfaces were modified by forming a SAM with carboxylic acid, which was further activated and reacted with the specific antibody for CRP. The immobilization was monitored in real time, as can be seen in Figure 5.10a. The detection of CRP at different concentrations (from 25 to 1000 ng/mL) shows a good dose-response (see Figure 5.10b).
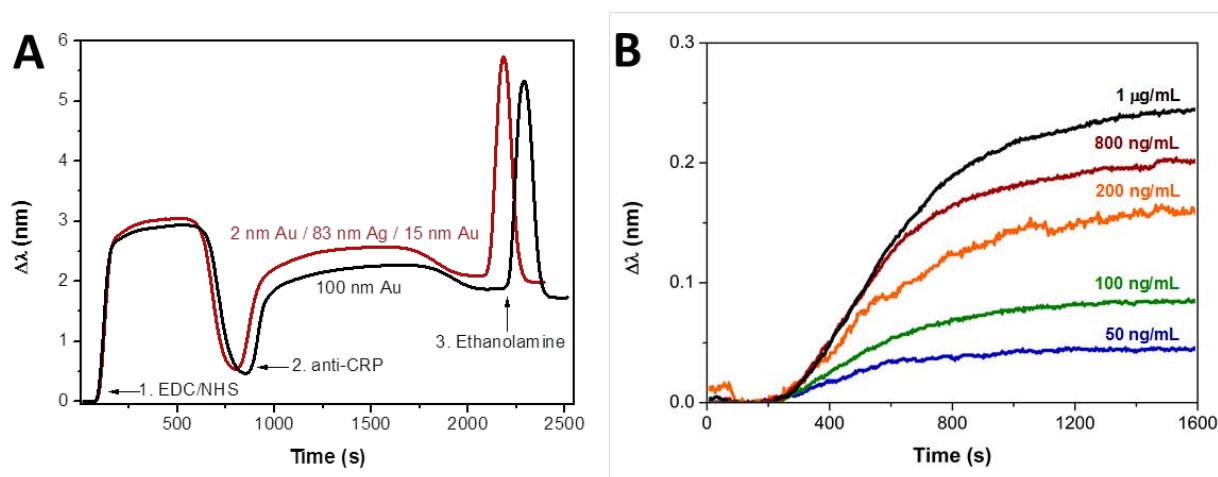
Figure 5.10 Biosensing experiments for the Au monolayer and Au/Ag/Au trilayer sensors. (A) Real-time sensograms showing the three steps involved in the covalent immobilization of the specific antibody anti-CRP over Au monolayer and Au/Ag/Au trilayer substrates. (B) Sensograms showing the detection of the target CRP protein at different concentrations (from 25 to 1000 ng/mL) in PBS buffer.

We were able to achieve a LOD of 2.6 ng/mL (20.8 pM) and a LOQ of 9.1 ng/mL (72.9 pM), respectively (see the calibration curves in Figure 5.11) which represents a slight improvement in biosensing performance compared to the Au single layer sensor (LOD of 3.7 ng/mL and a LOQ of 12.9 ng/mL). Thus, the higher plasmonic activity using a silver layer improved the biosensing performance of the device[153,154].
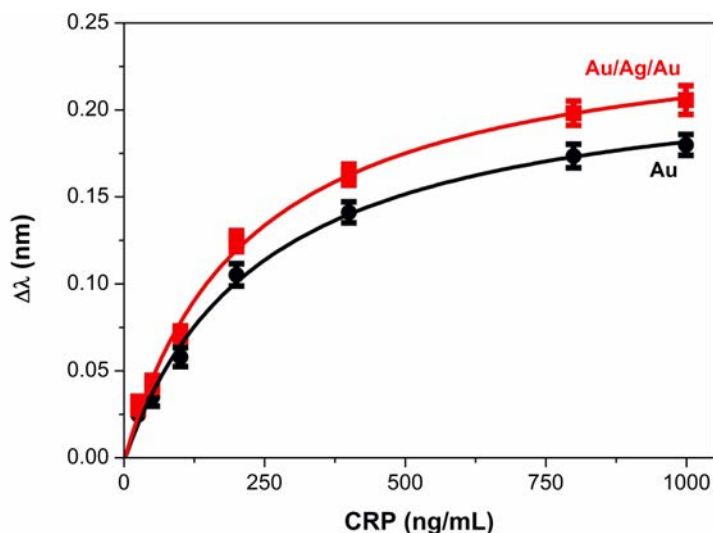
Figure 5.11 Calibration curves for CRP detection for the Au monolayer and Au/Ag/Au trilayer sensors. The error bars reflect the standard deviation (SD) from two measurements.

5.3.1 Detection of C reactive protein in urine

Finally, the viability of measuring biological samples, such as undiluted urine was also assessed with the trilayer sensors. In this case, an additional blocking step with a solution of PLL-PEG (0.5 mg/mL) was included in the biofunctionalization protocol in order to minimize non-specific adsorptions from components present in the complex urine media.

As can be observed in Figure 5.12a, a similar shift was observed for the same concentration of CRP in buffer before and after blocking (see Figure 5.12a (black and red lines), which confirms that this step did not affect the ability of the antibody to bind its target. The injection of pure undiluted urine and undiluted urine including a non-specific protein (i.e. BSA) resulted in no background ($\Delta\lambda_{SPR}=0$) (see Fig. 5.12a, green and magenta lines), which confirms the lack of nonspecific binding onto the biofunctionalized surface. Finally, the same CRP concentration in pure urine also resulted in the same signal obtained in buffer (same $\Delta\lambda_{SPR}=0$) (blue line in Fig. 5.12A). All these measurements confirm the feasibility of directly evaluating urine samples. Sensograms for different CRP concentrations summarized in Figure 5.12B.
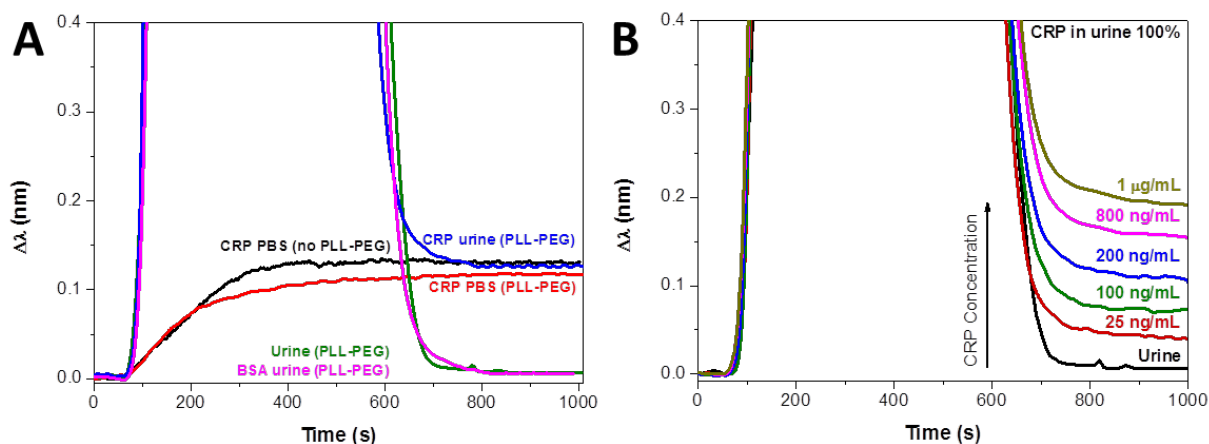
Figure 5.12 Biosensing experiments in undiluted urine for the Au/Ag/Au trilayer sensors. (a) Blocking step and urine effect. Sensograms showing the detection of CRP (200 ng/mL) in PBS without PLL-PEG blocking (black); the detection of CRP (200 ng/mL) in PBS after PLL-PEG blocking (red); nonspecific binding of undiluted urine (green); nonspecific binding of control protein (BSA, 500 μg/mL) in urine (magenta); detection of CRP (200 ng/mL) in undiluted urine (blue); (b) Sensograms showing the detection of the target CRP protein at different concentrations (from 25 to 1000 ng/mL) in undiluted urine.

The resulting calibration curve for CRP in urine showed comparable sensitivities to the ones obtained with standard buffer conditions demonstrating that the urine components did not hinder the immunochemical reaction (see Figure 5.13).
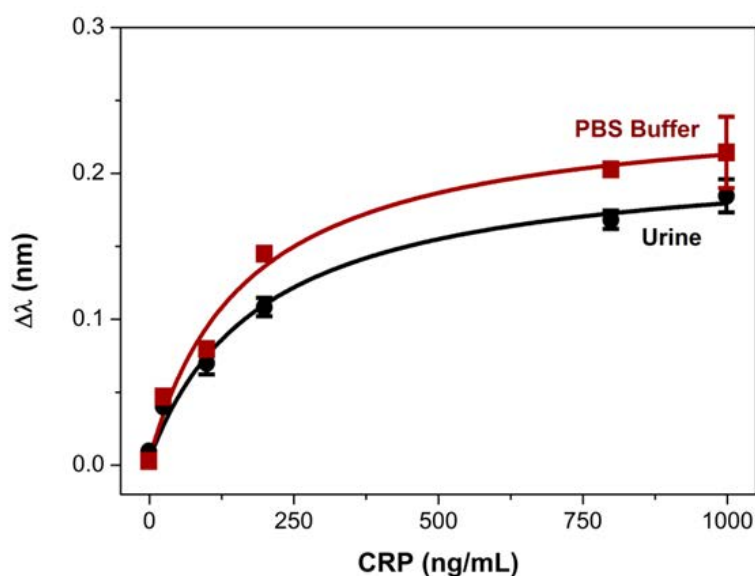
Figure 5.13 CRP calibration curves in PBS and undiluted urine. The error bars reflect the standard deviation (SD) from two measurements.

While the LOD in PBS was 2.6 ng/mL, a close value was reached with pure urine (LOD = 3.5 ng/mL (27.9 pM), and a LOQ = 12.3 ng/mL (97.7 pM)). This value is better compared to the previously obtained (5.3 ng/mL (42.4 pM)) in section 4.2.1, for the Au monolayer biosensor for the same bioassay with CRP protein biomarker.

Overall, the results reflect an improved performance for these easy-to-fabricate Au/Ag/Au plasmonic biosensors with an improved chemical stability and biosensing capabilities compared to their Au monolayer counterpart. However, the Au monolayer plasmonic biosensor is more than enough to achieve a real and commercial device, considering the slightly improvement in biosensing performance provided by the trilayer biosensor.

General Conclusions

This PhD thesis demonstrates the potential value of Blu-ray optical discs as nanostructured substrates to fabricate plasmonic biosensors for their application in the diagnostic field. These new, simple, fast and cost-effective analytical biosensor devices hold great promise for the development of low-cost sensors able to be integrated in portable analytical platforms for a myriad of diagnostics applications.

The main goal of this thesis was the development, fabrication and integration of a high reproducible and cost-effective plasmonic biosensor based on nanostructured materials. The proposed biosensor has been demonstrated, offering a simple and cost-effective fabrication process; additionally, the label-free detection of biomarkers in human fluids was achieved. Furthermore, with simple microfluidics designs, we were able to achieve parallel, multiplexed direct detection of several biomarkers with a high reproducibility between the sensing channels.

The main conclusions that can be drawn from the work done are as follows:

- This study demonstrates that simple, cost-effective nanostructured plasmonic biosensors based on Blu-ray discs with integrated microfluidics can be fabricated for the development of new, simple, fast and cost-effective analytical methodologies for diagnosis. The sensors were fabricated following very simple and reproducible processes. In contrast to other engineered nanoslit based sensors, we were able to take advantage of the high-throughput fabrication process of Blu-ray discs at industrial scale to achieve highly reproducible substrates from batch to batch. We used two different metal layer thicknesses to evaluate its influence in the optical performance of the final sensor device.

- The sensor chips were optically characterized under TM polarized white light at different angles of incidence to increase the light's trapping/confinement with the increase of the light incident angle in order to evaluate their

111

performance as a biosensor. A wavelength shift interrogation method was used to optimize the biosensor performance by tuning the optical conditions and the thickness of the nanostructured substrate. We performed three-dimensional finite difference time-domain simulations to evaluate the reflectance spectra and the electric field distributions with a good agreement between the theoretical simulations and experimental results.

A figure of merit up to 35 nm^{-1} and a bulk limit of detection up to 6.3×10^{-6} RIU were obtained, which are highly competitive values when compared to current state-of-the-art surface plasmon resonance biosensors.

- With a view to achieving a compact operative device, further integration was done by incorporating a Cyclic Olefin Copolymer flow cell with a patterned microfluidics (single channel of 100 μm height) obtained using simple and inexpensive double-sided adhesive tape. All the optical components were fixed on a 75×75 mm portable prototype, illustrating its facile miniaturization, integration and potential portability. Given the simplicity, reproducibility and the low cost of the sensor fabrication process, together with its straightforward integration, the presented sensor device is a promising candidate for the development of competitive POC platforms.

- The viability of this configuration for biosensing was further explored by performing label-free measurements based on the detection of specific antibodies for the GTF2b protein, a tumor-associated antigen related to colorectal cancer. Label-free measurements were also carried out on the detection of C-reactive protein, a well-known and valuable biomarker related with inflammation and infection processes. We achieved limits of detection in the pM order in both cases. We also assessed the feasibility of measuring biological samples by evaluating diluted serum and undiluted urine, achieving promising performance in these complex human matrixes.

- The development of a multiplexed label-free biosensing assay based on the fabricated sensors was further explored by the design and fabrication of a simple four-channel device. With a coefficient of variation of only 5.9%

between sensing channels and a limit of detection of up to 7.52 x10^{-6} RIU, we achieved a competitive multichannel device. Two immunoassays were performed: 1) a four-channel biofunctionalization to detect the presence of a protein, in order to evaluate the inter-channel biosensing performance and reproducibility, and 2) a selective channel biofunctionalization performed to detect the presence of two proteins, in order to evaluate the feasibility to perform multiplexed biosensing. The Interleukin-6 (IL6) and C-reactive (CRP) proteins, well-known and valuable biomarkers associated with inflammation and infection processes were evaluated in buffer and in undiluted urine. Experimental results demonstrate the absence of cross-signals between the biofunctionalized sensing channels and the possibility of performing parallel and multiplexed biosensing assays.

- Finally, in an attempt to improve the sensing performance of the presented nanostructures, we report the fabrication of a simple and ultrasmooth (surface roughness <0.5 nm) Au/Ag/Au nanostructured plasmonic sensor using Blu-ray optical discs. In contrast to other strategies, our approach takes advantage of the high adhesion of gold in polycarbonate to improve the wettability and reduce the surface roughness in the Au/Ag/Au nanostructured plasmonic sensors, without increasing ohmic plasmon losses and using only a thin gold film as an adhesion/nucleation layer for the overlying silver film. This novel trilayer structure achieved better performance in terms of sensitivity and resolution over the purely Au counterpart. Furthermore, we produced Ag containing plasmonic devices which are chemically stable over time. The label-free biosensing capability of the proposed Au/Ag/Au plasmonic structure was evaluated by performing real-time detection of the CRP protein biomarker in PBS buffer and in pure undiluted urine, obtaining sensitivities in both cases in the pM order. Biodetection results showed a slight improvement when compared to Au plasmonic surfaces, indicating the potential to obtain chemically stable and ultrasmooth silver/gold flexible polymer nanostructured sensors for direct and label-free biosensor applications.

Future studies could be focused in the miniaturization and fully integration in a point-of-care system. Furthermore, with the latest advances in integrated photonic devices and microfluidic designs that allow real raw samples it will be possible to achieve truly lab-on-a-chip systems with a high potential for decentralized diagnosis in the near future.

Bibliography

1. Retrieved 12/04/2018, from:
   http://www.iupac.org/goldbook/B00663.pdf., 2018.

2. Dahlin, A. B., Tegenfeldt, J. O., & Höök, F. (2006). Improving the instrumental resolution of sensors based on localized surface plasmon resonance. *Analytical Chemistry*, *78*(13), 4416-4423.

3. Vigneshvar, S., Sudhakumari, C. C., Senthilkumaran, B., & Prakash, H. (2016). Recent advances in biosensor technology for potential applications– an overview. *Frontiers in bioengineering and biotechnology*, *4*(1), 11-20.

4. Da Silva, E. T., Souto, D. E., Barragan, J. T., de F Giarola, J., de Moraes, A., & Kubota, L. T. (2017). Electrochemical Biosensors in Point-of-Care Devices: Recent Advances and Future Trends. *ChemElectroChem*, *4*(4), 778-794.

5. Wang, J. (2006). Electrochemical biosensors: towards point-of-care cancer diagnostics. *Biosensors and Bioelectronics*, *21*(10), 1887-1892.

6. Zhu, C., Yang, G., Li, H., Du, D., & Lin, Y. (2014). Electrochemical sensors and biosensors based on nanomaterials and nanostructures. *Analytical Chemistry*, *87*(1), 230-249.

7. Arlett, J. L., Myers, E. B., & Roukes, M. L. (2011). Comparative advantages of mechanical biosensors. *Nature Nanotechnology*, *6*(4), 203-215.

8. Deng, X., Chen, M., Fu, Q., Smeets, N. M., Xu, F., Zhang, Z., & Hoare, T. (2016). A highly sensitive immunosorbent assay based on biotinylated graphene oxide and the quartz crystal microbalance. *ACS Applied Materials & Interfaces*, *8*(3), 1893-1902.

9. Atay, S., Pişkin, K., Yılmaz, F., Çakır, C., Yavuz, H., & Denizli, A. (2016). Quartz crystal microbalance based biosensors for detecting highly metastatic breast cancer cells via their transferrin receptors. *Analytical Methods*, *8*(1), 153-161.

10. Shen, Z., Huang, M., Xiao, C., Zhang, Y., Zeng, X., & Wang, P. G. (2007). Nonlabeled quartz crystal microbalance biosensor for bacterial detection using carbohydrate and lectin recognitions. *Analytical chemistry*, *79*(6), 2312-2319.

11. Dubiel, E. A., Martin, B., Vigier, S., & Vermette, P. (2017). Real-time label-free detection and kinetic analysis of Etanercept—Protein A interactions using quartz crystal microbalance. *Colloids and Surfaces B: Biointerfaces*, *149*(1), 312-321.

12. Reviakine, I., Johannsmann, D., & Richter, R. P. (2011). Hearing what you cannot see and visualizing what you hear: interpreting quartz crystal microbalance data from solvated interfaces. *Analytical Chemistry*, *83*(23), 8838–8848.

13. Fan, X., White, I. M., Shopova, S. I., Zhu, H., Suter, J. D., & Sun, Y. (2008). Sensitive optical biosensors for unlabeled targets: A review. *Analytica Chimica Acta*, *620*(1), 8-26.

14. Hutchinson, A. M. (1995). Evanescent wave biosensors. *Molecular Biotechnology*, *3*(1), 47-54.

15. Fan, X., White, I. M., Shopova, S. I., Zhu, H., Suter, J. D., & Sun, Y. (2008). Sensitive optical biosensors for unlabeled targets: A review. *Analytica Chimica Acta*, *620*(1-2), 8-26.

16. Vollmer, F., & Arnold, S. (2008). Whispering-gallery-mode biosensing: label-free detection down to single molecules. *Nature Methods*, *5*(7), 591–596.

17. Kozma, P., Kehl, F., Ehrentreich-Förster, E., Stamm, C., & Bier, F. F. (2014). Integrated planar optical waveguide interferometer biosensors: A comparative review. *Biosensors and Bioelectronics*, *58*, 287-307.

18. Baaske, M., & Vollmer, F. (2012). Optical resonator biosensors: molecular diagnostic and nanoparticle detection on an integrated platform. *ChemPhysChem*, *13*(2), 427-436.

19. Bogaerts, W., De Heyn, P., Van Vaerenbergh, T., De Vos, K., Kumar Selvaraja, S., Claes, T., & Baets, R. (2012). Silicon microring resonators. Laser & Photonics Reviews, 6(1), 47-73.

20. Nguyen, H. H., Park, J., Kang, S., & Kim, M. (2015). Surface plasmon resonance: a versatile technique for biosensor applications. *Sensors*, *15*(5), 10481-10510.

21. Brulé, T., Granger, G., Bukar, N., Deschênes-Rancourt, C., Havard, T., Schmitzer, A. R., & Masson, J. F. (2017). A field-deployed surface plasmon resonance (SPR) sensor for RDX quantification in environmental waters. *Analyst*, *142*(12), 2161-2168.

22. Masson, J. F. (2017). Surface plasmon resonance clinical biosensors for medical diagnostics. *ACS sensors*, *2*(1), 16-30.

23. Homola, J. (2003). Present and future of surface plasmon resonance biosensors. *Analytical and bioanalytical chemistry*, *377*(3), 528-539.

24. Homola, J., Yee, S. S., & Gauglitz, G. (1999). Surface plasmon resonance sensors. *Sensors and Actuators B: Chemical*, *54*(1-2), 3-15.

25. Boriskina, S. V., Cooper, T. A., Zeng, L., Ni, G., Tong, J. K., Tsurimaki, Y., & Chen, G. (2017). Losses in plasmonics: from mitigating energy dissipation to embracing loss-enabled functionalities. *Advances in Optics and Photonics*, *9*(4), 775-827.

26. Jana, J., Ganguly, M., & Pal, T. (2016). Enlightening surface plasmon resonance effect of metal nanoparticles for practical spectroscopic application. *RSC Advances*, *6*(89), 86174-86211.

27. Vinogradov, A. P., Dorofeenko, A. V., Pukhov, A. A., & Lisyansky, A. A. (2018). Exciting surface plasmon polaritons in the Kretschmann configuration by a light beam. *Physical Review B*, *97*(23), 1-9.

28. Harris, R. D., & Wilkinson, J. S. (1995). Waveguide surface plasmon resonance sensors. *Sensors and Actuators B: Chemical*, *29*(1), 261-267.

29. Homola, J. (2008). Surface plasmon resonance sensors for detection of chemical and biological species. *Chemical Reviews*, *108*(2), 462-493.

30. Homola, J., Koudela, I., & Yee, S. S. (1999). Surface plasmon resonance sensors based on diffraction gratings and prism couplers: sensitivity comparison. *Sensors and Actuators B: Chemical*, *54*(1), 16-24.

31. Dostálek, J., Homola, J., & Miler, M. (2005). Rich information format surface plasmon resonance biosensor based on array of diffraction gratings. *Sensors and Actuators B: Chemical*, *107*(1), 154-161.

32. Snopok, B. A. (2012). Theory and practical application of surface plasmon resonance for analytical purposes. *Theoretical and Experimental Chemistry*, *48*(5), 283-306.

33. Piliarik, M., & Homola, J. (2009). Surface plasmon resonance (SPR) sensors: approaching their limits?. *Optics Express*, *17*(19), 16505-16517.

34. Lopez, G. A., Estévez, M. C., Soler, M., & Lechuga, L. M. (2017). Recent advances in nanoplasmonic biosensors: Applications and lab-on-a-chip integration. *Nanophotonics*, *6*(1), 123-136.

35. Špačková, B., Wrobel, P., Bocková, M., & Homola, J. (2016). Optical biosensors based on plasmonic nanostructures: a review. *Proceedings of the IEEE*, *104*(12), 2380-2408.

36. Mayer, K. M., & Hafner, J. H. (2011). Localized surface plasmon resonance sensors. *Chemical Reviews*, *111*(6), 3828-3857.

37. Tokel, O., Inci, F., & Demirci, U. (2014). Advances in plasmonic technologies for point of care applications. *Chemical Reviews*, *114*(11), 5728-5752.

38. Willets, K. A., & Van Duyne, R. P. (2007). Localized surface plasmon resonance spectroscopy and sensing. *Annual Reviews in Physical Chemistry*, *58*, 267-297.

39. Dahlin, A. B., Wittenberg, N. J., Höök, F., & Oh, S. H. (2013). Promises and challenges of nanoplasmonic devices for refractometric biosensing. *Nanophotonics*, *2*(2), 83-101.

40. Piliarik, M., Šípová, H., Kvasnička, P., Galler, N., Krenn, J. R., & Homola, J. (2012). High-resolution biosensor based on localized surface plasmons. *Optics Express*, *20*(1), 672-680.

41. Sipova, H., Vrba, D., & Homola, J. (2011). Analytical value of detecting an individual molecular binding event: the case of the surface plasmon resonance biosensor. *Analytical Chemistry*, *84*(1), 30-33.

42. Svedendahl, M., Chen, S., Dmitriev, A., & Kall, M. (2009). Refractometric sensing using propagating versus localized surface plasmons: a direct comparison. *Nano Letters*, *9*(12), 4428-4433.

43. Estévez, M. C., Otte, M. A., Sepúlveda, B., & Lechuga, L. M. (2014). Trends and challenges of refractometric nanoplasmonic biosensors: A review. *Analytica Chimica Acta*, *806*, 55-73.

44. Otte, M. A., Sepulveda, B., Ni, W., Juste, J. P., Liz-Marzán, L. M., & Lechuga, L. M. (2009). Identification of the optimal spectral region for plasmonic and nanoplasmonic sensing. *ACS Nano, 4*(1), 349-357.

45. Martinsson, E., Otte, M. A., Shahjamali, M. M., Sepúlveda, B., & Aili, D. (2014). Substrate effect on the refractive index sensitivity of silver nanoparticles. *The Journal of Physical Chemistry C, 118*(42), 24680-24687.

46. Mazzotta, F., Johnson, T. W., Dahlin, A. B., Shaver, J., Oh, S. H., & Höök, F. (2015). Influence of the evanescent field decay length on the sensitivity of plasmonic nanodisks and nanoholes. *ACS Photonics, 2*(2), 256-262.

47. Cialla, D., März, A., Böhme, R., Theil, F., Weber, K., Schmitt, M., & Popp, J. (2012). Surface-enhanced Raman spectroscopy (SERS): progress and trends. *Analytical and Bioanalytical Chemistry, 403*(1), 27-54.

48. Khanikaev, A. B., Wu, C., & Shvets, G. (2013). Fano-resonant metamaterials and their applications. *Nanophotonics, 2*(4), 247-264.

49. Bahramipanah, M., Dutta-Gupta, S., Abasahl, B., & Martin, O. J. (2015). Cavity-coupled plasmonic device with enhanced sensitivity and figure-of-merit. *ACS Nano, 9*(7), 7621-7633.

50. Feuz, L., Jonsson, M. P., & Höök, F. (2012). Material-selective surface chemistry for nanoplasmonic sensors: optimizing sensitivity and controlling binding to local hot spots. *Nano Letters, 12*(2), 873-879.

51. Kumar, K., Dahlin, A. B., Sannomiya, T., Kaufmann, S., Isa, L., & Reimhult, E. (2013). Embedded plasmonic nanomenhirs as location-specific biosensors. *Nano Letters, 13*(12), 6122-6129.

52. Soler, M., Estévez, M., Álvarez, M., Otte, M. A., Sepúlveda, B., & Lechuga, L. M. (2014). Direct detection of protein biomarkers in human fluids using site-specific antibody immobilization strategies. *Sensors, 14*(2), 2239-2258.

53. Huertas, C. S., Carrascosa, L. G., Bonnal, S., Valcárcel, J., & Lechuga, L. M. (2016). Quantitative evaluation of alternatively spliced mRNA isoforms by label-free real-time plasmonic sensing. *Biosensors and Bioelectronics*, *78*, 118-125.

54. Zhu, Z., Feng, M., Zuo, L., Zhu, Z., Wang, F., Chen, L., & Luo, S. Z. (2015). An aptamer based surface plasmon resonance biosensor for the detection of ochratoxin A in wine and peanut oil. *Biosensors and Bioelectronics*, *65*, 320-326.

55. Wijaya, E., Lenaerts, C., Maricot, S., Hastanin, J., Habraken, S., Vilcot, J. P., & Szunerits, S. (2011). Surface plasmon resonance-based biosensors: From the development of different SPR structures to novel surface functionalization strategies. *Current Opinion in Solid State and Materials Science*, *15*(5), 208-224.

56. Mauriz, E., García-Fernández, M. C., & Lechuga, L. M. (2016). Towards the design of universal immunosurfaces for SPR-based assays: A review. *TrAC Trends in Analytical Chemistry*, *79*, 191-198.

57. Joshi, K. A., Tang, J., Haddon, R., Wang, J., Chen, W., & Mulchandani, A. (2005). A disposable biosensor for organophosphorus nerve agents based on carbon nanotubes modified thick film strip electrode. *Electroanalysis*, *17*(1), 54-58.

58. Brena, B., González-Pombo, P., & Batista-Viera, F. (2013). Immobilization of enzymes: a literature survey. In *Immobilization of enzymes and cells* (pp. 15-31). Humana Press, Totowa, NJ.

59. Mohamad, N. R., Marzuki, N. H. C., Buang, N. A., Huyop, F., & Wahab, R. A. (2015). An overview of technologies for immobilization of enzymes and surface analysis techniques for immobilized enzymes. *Biotechnology & Biotechnological Equipment*, *29*(2), 205-220.

60. Shankaran, D. R., & Miura, N. (2007). Trends in interfacial design for surface plasmon resonance based immunoassays. *Journal of Physics D: Applied Physics*, *40*(23), 7187.

61. Datta, S., Christena, L. R., & Rajaram, Y. R. S. (2013). Enzyme immobilization: an overview on techniques and support materials, *3 Biotech*, *3*(1), 1-9.

62. Shen, Q., Yang, R., Hua, X., Ye, F., Zhang, W., & Zhao, W. (2011). Gelatin-templated biomimetic calcification for β-galactosidase immobilization. *Process Biochemistry*, *46*(8), 1565-1571.

63. Górecka, E., & Jastrzębska, M. (2011). Immobilization Techniques and Biopolymer Carriers–A Review. *Food Science and Biotechnology*, *75*, 27-34.

64. Tsai, W. C., & Li, I. C. (2009). SPR-based immunosensor for determining staphylococcal enterotoxin A. *Sensors and Actuators B: Chemical*, *136*(1), 8-12.

65. Vaisocherova, H., Yang, W., Zhang, Z., Cao, Z., Cheng, G., Piliarik, M., & Jiang, S. (2008). Ultralow fouling and functionalizable surface chemistry based on a zwitterionic polymer enabling sensitive and specific protein detection in undiluted blood plasma. *Analytical Chemistry*, *80*(20), 7894-7901.

66. Kausaite-Minkstimiene, A., Ramanaviciene, A., Kirlyte, J., & Ramanavicius, A. (2010). Comparative study of random and oriented antibody immobilization techniques on the binding capacity of immunosensor. *Analytical Chemistry*, *82*(15), 6401-6408.

67. Jung, Y., Lee, J. M., Jung, H., & Chung, B. H. (2007). Self-Directed and Self-Oriented Immobilization of Antibody by Protein G− DNA Conjugate. *Analytical Chemistry*, *79*(17), 6534-6541.

68. Masson, J. F., Battaglia, T. M., Cramer, J., Beaudoin, S., Sierks, M., & Booksh, K. S. (2006). Reduction of nonspecific protein binding on surface plasmon resonance biosensors. *Analytical and Bioanalytical Chemistry*, *386*(7-8), 1951-1959.

69. Aubé, A., Breault-Turcot, J., Chaurand, P., Pelletier, J. N., & Masson, J. F. (2013). Non-specific adsorption of crude cell lysate on surface plasmon resonance sensors. *Langmuir*, *29*(32), 10141-10148.

70. Wang, X., Li, Y., Wang, H., Fu, Q., Peng, J., Wang, Y., & Zhan, L. (2010). Gold nanorod-based localized surface plasmon resonance biosensor for sensitive detection of hepatitis B virus in buffer, blood serum and plasma. *Biosensors and Bioelectronics*, *26*(2), 404-410.

71. Bergstrand, A., Rahmani-Monfared, G., Östlund, Å., Nydén, M., & Holmberg, K. (2009). Comparison of PEI-PEG and PLL-PEG copolymer coatings on the prevention of protein fouling. *Journal of Biomedical Materials Research Part A*, *88*(3), 608-615.

72. Oh, B. K., Kim, Y. K., Park, K. W., Lee, W. H., & Choi, J. W. (2004). Surface plasmon resonance immunosensor for the detection of Salmonella typhimurium. *Biosensors and Bioelectronics*, *19*(11), 1497-1504.

73. Khanna, V. K. (2016). Top-Down Nanofabrication. In *Integrated Nanoelectronics* (pp. 381-396). Springer, New Dehli.

74. Khanna, V. K. (2016). Bottom-up Nanofabrication. In *Integrated Nanoelectronics* (pp. 397-417). Springer, New Dehli.

75. Zeng, S., Yong, K. T., Roy, I., Dinh, X. Q., Yu, X., & Luan, F. (2011). A review on functionalized gold nanoparticles for biosensing applications. *Plasmonics*, *6*(3), 491-506.

76. Fredriksson, H., Alaverdyan, Y., Dmitriev, A., Langhammer, C., Sutherland, D. S., Zäch, M., & Kasemo, B. (2007). Hole–mask colloidal lithography. *Advanced Materials*, *19*(23), 4297-4302.

77. Lotito, V., & Zambelli, T. (2017). Approaches to self-assembly of colloidal monolayers: A guide for nanotechnologists. *Advances in Colloid and Interface Science*, *246*, 217-274.

78. Biswas, A., Bayer, I. S., Biris, A. S., Wang, T., Dervishi, E., & Faupel, F. (2012). Advances in top–down and bottom–up surface nanofabrication: Techniques, applications & future prospects. *Advances in colloid and interface science*, *170*(1-2), 2-27.

79. Chen, Y. (2015). Nanofabrication by electron beam lithography and its applications: A review. *Microelectronic Engineering*, *135*, 57-72.

80. Volkert, C. A., & Minor, A. M. (2007). Focused ion beam microscopy and micromachining. *MRS bulletin*, *32*(5), 389-399.

81. Aksu, S., Yanik, A. A., Adato, R., Artar, A., Huang, M., & Altug, H. (2010). High-throughput nanofabrication of infrared plasmonic nanoantenna arrays for vibrational nanospectroscopy. *Nano Letters*, *10*(7), 2511-2518.

82. Seo, J. H., Park, J. H., Kim, S. I., Park, B. J., Ma, Z., Choi, J., & Ju, B. K. (2014). Nanopatterning by laser interference lithography: applications to optical devices. *Journal of Nanoscience and Nanotechnology*, *14*(2), 1521-1532.

83. Kooy, N., Mohamed, K., Pin, L. T., & Guan, O. S. (2014). A review of roll-to-roll nanoimprint lithography. *Nanoscale Research Letters*, *9*(1), 320-329.

84. Gartia, M. R., Hsiao, A., Pokhriyal, A., Seo, S., Kulsharova, G., Cunningham, B. T., & Liu, G. L. (2013). Colorimetric plasmon resonance imaging using nano lycurgus cup arrays. *Advanced Optical Materials*, *1*(1), 68-76.

85. Shen, Y., Zhou, J., Liu, T., Tao, Y., Jiang, R., Liu, M., & Jin, C. (2013). Plasmonic gold mushroom arrays with refractive index sensing figures of merit approaching the theoretical limit. *Nature Communications*, *4*, 2381-2390.

86. Lee, K. L., Huang, J. B., Chang, J. W., Wu, S. H., & Wei, P. K. (2015). Ultrasensitive biosensors using enhanced Fano resonances in capped gold nanoslit arrays. *Scientific Reports*, *5*, 8547-8556.

87. Dodson, S., Haggui, M., Bachelot, R., Plain, J., Li, S., & Xiong, Q. (2013). Optimizing electromagnetic hotspots in plasmonic bowtie nanoantenna. *The Journal of Physical Chemistry Letters*,*4*(3), 496-501.

88. Abbas, A., Tian, L., Morrissey, J. J., Kharasch, E. D., & Singamaneni, S. (2013). Hot Spot-Localized Artificial Antibodies for Label-Free Plasmonic Biosensing. *Advanced Functional Materials*, *23*(14), 1789-1797.

89. Whitesides, G. M. (2006). The origins and the future of microfluidics. *Nature*, *442*(7101), 368-373.

90. Jung, W., Han, J., Choi, J. W., & Ahn, C. H. (2015). Point-of-care testing (POCT) diagnostic systems using microfluidic lab-on-a-chip technologies. *Microelectronic Engineering*, *132*, 46-57.

91. Novak, R., Wartmann, D., Mathies, R. A., Dostálek, J., & Ertl, P. (2015). Microfluidic platform for multiplexed cell sampling and time-resolved SPR-based cytokine sensing. In *6th European Conference of the International Federation for Medical and Biological Engineering* (pp. 785-788). Springer, Cham.

92. He, J., Boegli, M., Bruzas, I., Lum, W., & Sagle, L. (2015). Patterned plasmonic nanoparticle arrays for microfluidic and multiplexed biological assays. *Analytical Chemistry*, *87*(22), 11407-11414.

93. Retrieved 12/04/2018, from:
    http://hamamatsu.magnet.fsu.edu/articles/quantumefficiency.html, 2018.

94. Cappi, G., Spiga, F. M., Moncada, Y., Ferretti, A., Beyeler, M., Bianchessi, M., & Guiducci, C. (2015). Label-free detection of tobramycin in serum by transmission localized surface plasmon resonance. *Analytical Chemistry*, *87*(10), 5278-5285.

95. Roda, A., Michelini, E., Zangheri, M., Di Fusco, M., Calabria, D., & Simoni, P. (2016). Smartphone-based biosensors: A critical review and perspectives. *Trends in Analytical Chemistry*, *79*, 317-325.

96. Guner, H., Ozgur, E., Kokturk, G., Celik, M., Esen, E., Topal, A. E., & Dana, A. (2017). A smartphone based surface plasmon resonance imaging (SPRi) platform for on-site biodetection. *Sensors and Actuators B: Chemical*, *239*, 571-577.

97. Kaplan, B., Guner, H., Senlik, O., Gurel, K., Bayindir, M., & Dana, A. (2009). Tuning optical discs for plasmonic applications. *Plasmonics*, *4*(3), 237-243.

98. Dou, X., Phillips, B. M., Chung, P. Y., & Jiang, P. (2012). High surface plasmon resonance sensitivity enabled by optical discs. *Optics letters*, *37*(17), 3681-3683.

99. Martinez-Perdiguero, J., Retolaza, A., Juarros, A., Otaduy, D., & Merinoa, S. (2012). Enhanced transmission through gold nanohole arrays fabricated by thermal nanoimprint lithography for surface plasmon based biosensors. *Procedia Engineering*, *47*, 805-808.

100. Austin, M. D., Ge, H., Wu, W., Li, M., Yu, Z., Wasserman, D. & Chou, S. Y. (2004). Fabrication of 5 nm linewidth and 14 nm pitch features by nanoimprint lithography. *Applied Physics Letters*, *84*(26), 5299-5301.

101.   Ogończyk, D., Węgrzyn, J., Jankowski, P., Dąbrowski, B., & Garstecki, P. (2010). Bonding of microfluidic devices fabricated in polycarbonate. *Lab on a Chip*, *10*(10), 1324-1327.

102.   Nge, P. N., Rogers, C. I., & Woolley, A. T. (2013). Advances in microfluidic materials, functions, integration, and applications. *Chemical Reviews*, *113*(4), 2550-2583.

103.   Patnaik, A., & Li, C. (1998). Evidence for metal interaction in gold metallized polycarbonate films: an X-ray photoelectron spectroscopy investigation. *Journal of Applied Physics*, *83*(6), 3049-3056.

104.   Otte, M. A., Estévez, M. C., Carrascosa, L. G., González-Guerrero, A. B., Lechuga, L. M., & Sepúlveda, B. (2011). Improved biosensing capability with novel suspended nanodisks. *The Journal of Physical Chemistry C, 115*(13), 5344-5351.

105.   Kruglyak, H. (1991). The compact disc as a diffraction grating. *Physics Education*, *26*(4), 255-257.

106.   DeWeerd, A. J. (2016). CD, DVD, and Blu-Ray Disc Diffraction with a Laser Ray Box. *The Physics Teacher*, *54*(5), 300-301.

107.   Lee, K. L., Chang, C. C., You, M. L., Pan, M. Y., & Wei, P. K. (2016). Enhancing the surface sensitivity of metallic nanostructures using oblique-angle-induced Fano resonances.*Scientific reports*, *6*, 33126-33135.

108.   Sultanova, N., Kasarova, S., & Nikolov, I. (2009). Dispersion proper ties of optical polymers. *Acta Physica Polonica-Series A General Physics*, *116*(4), 585-587.

109.   Johnson, P. B., & Christy, R. W. (1972). Optical constants of the noble metals. *Physical review B*, *6*(12), 4370-4379.

110. Zhou, W., & Odom, T. W. (2011). Tunable subradiant lattice plasmons by out-of-plane dipolar interactions. *Nature Nanotechnology, 6*(7), 423-427.

111. Drdácký, M., Lesák, J., Rescic, S., Slížková, Z., Tiano, P., & Valach, J. (2012). Standardization of peeling tests for assessing the cohesion and consolidation characteristics of historic stone surfaces. *Materials and Structures, 45*(4), 505-520.

112. Byun, I., Coleman, A. W., & Kim, B. (2013). Transfer of thin Au films to polydimethylsiloxane (PDMS) with reliable bonding using (3-mercaptopropyl) trimethoxysilane (MPTMS) as a molecular adhesive. *Journal of Micromechanics and Microengineering, 23*(8), 85016-85026.

113. Jin, Y., Kang, X., Song, Y., Zhang, B., Cheng, G., & Dong, S. (2001). Controlled nucleation and growth of surface-confined gold nanoparticles on a (3-aminopropyl) trimethoxysilane-modified glass slide: a strategy for SPR substrates. *Analytical Chemistry, 73*(13), 2843-2849.

114. Nath, P., Fung, D., Kunde, Y. A., Zeytun, A., Branch, B., & Goddard, G. (2010). Rapid prototyping of robust and versatile microfluidic components using adhesive transfer tapes. *Lab on a Chip, 10*(17), 2286-2291.

115. San-Miguel, A., & Lu, H. (2013). Microfluidics as a tool for C. elegans research. WormBook, ed. The C. elegans Research Community, WormBook, doi/10.1895/wormbook.1.162.1, http://www.wormbook.org

116. Kyriacou, G., Chang, H., Gargiuli, J., Agarwal, A., & Vadgama, P. (2016). Microfluidics a Potent Route to Sample Delivery for Non-intrusive Sensors. In *Biosensors for Security and Bioterrorism Applications* (pp. 15-34). Springer, Cham.

117. Kulisch, W. (2011). Nanotechnology-Based Modern Sensors and Biosensors. In *Nanotechnological Basis for Advanced Sensors* (pp. 3-24). Springer, Dordrecht.

118.	Soler, M., Mesa-Antúnez, P., Estévez, M. C., Ruiz-Sánchez, A. J., Otte, M. A., Sepúlveda, B., & Lechuga, L. M. (2015). Highly sensitive dendrimer-based nanoplasmonic biosensor for drug allergy diagnosis. *Biosensors and Bioelectronics*, *66*, 115-123.

119.	Soler, M., Estévez, M. C., Villar-Vázquez, R., Casal, J. I., & Lechuga, L. M. (2016). Label-free nanoplasmonic sensing of tumor-associate autoantibodies for early diagnosis of colorectal cancer. *Analytica Chimica Acta*, *930*, 31-38.

120.	Kim, J., Surapaneni, R., & Gale, B. K. (2009). Rapid prototyping of microfluidic systems using a PDMS/polymer tape composite. *Lab on a Chip*, *9*(9), 1290-1293.

121.	Patko, D., Mártonfalvi, Z., Kovacs, B., Vonderviszt, F., Kellermayer, M., & Horvath, R. (2014). Microfluidic channels laser-cut in thin double-sided tapes: cost-effective biocompatible fluidics in minutes from design to final integration with optical biochips. *Sensors and Actuators B: Chemical*, *196*, 352-356.

122.	Friend, J., & Yeo, L. (2010). Fabrication of microfluidic devices using polydimethylsiloxane. *Biomicrofluidics*, *4*(2), 26502-26508.

123.	Khanarian, G. (2001). Optical properties of cyclic olefin copolymers. *Optical Engineering*, *40*(6), 1024-1030.

124.	Aghvami, S. A., Opathalage, A., Zhang, Z. K., Ludwig, M., Heymann, M., Norton, M., & Fraden, S. (2017). Rapid prototyping of cyclic olefin copolymer (COC) microfluidic devices. *Sensors and Actuators B: Chemical*, *247*, 940-949.

125.	Lee, K. L., Chen, P. W., Wu, S. H., Huang, J. B., Yang, S. Y., & Wei, P. K. (2012). Enhancing surface plasmon detection using template-stripped gold nanoslit arrays on plastic films. *ACS Nano*, *6*(4), 2931-2939.

126.   Barderas, R., Villar-Vázquez, R., Fernández-Aceñero, M. J., Babel, I., Peláez-García, A., Torres, S., & Casal, J. I. (2013). Sporadic colon cancer murine models demonstrate the value of autoantibody detection for preclinical cancer diagnosis. *Scientific Reports*, *3*, 2938-2945.

127.   Liu, W., Peng, B., Lu, Y., Xu, W., Qian, W., & Zhang, J. Y. (2011). Autoantibodies to tumor-associated antigens as biomarkers in cancer immunodiagnosis. *Autoimmunity Reviews*, *10*(6), 331-335.

128.   Casiano, C. A., Mediavilla-Varela, M., & Tan, E. M. (2006). Tumor-associated antigen arrays for the serological diagnosis of cancer. *Molecular & Cellular Proteomics*, *5*(10), 1745-1759.

129.   Chen, H., Werner, S., Tao, S., Zörnig, I., & Brenner, H. (2014). Blood autoantibodies against tumor-associated antigens as biomarkers in early detection of colorectal cancer. *Cancer Letters*, *346*(2), 178-187.

130.   Barderas, R., Babel, I., Díaz-Uriarte, R., Moreno, V., Suárez, A., Bonilla, F., & Casal, J. I. (2012). An optimized predictor panel for colorectal cancer diagnosis based on the combination of tumor-associated antigens obtained from protein and phage microarrays. *Journal of Proteomics*, *75*(15), 4647-4655.

131.   Dutta, P., Horiuchi, K., & Jubery, T. Z. (2015). Microfluidic Circuits. In *Encyclopedia of Microfluidics and Nanofluidics* (pp. 1901-1909). Springer, New York.

132.   Oh, K. W., Lee, K., Ahn, B., & Furlani, E. P. (2012). Design of pressure-driven microfluidic networks using electric circuit analogy. *Lab on a Chip*, *12*(3), 515-545.

133.   Ferry, M. S., Razinkov, I. A., & Hasty, J. (2011). Microfluidics for synthetic biology: from design to execution. *Methods in Enzymology*, *497*, 295-372.

134.   Pepys, M. B., & Hirschfield, G. M. (2003). C-reactive protein: a critical update. *The Journal of Clinical Investigation*, *111*(12), 1805-1812.

135.   Allin, K. H., & Nordestgaard, B. G. (2011). Elevated C-reactive protein in the diagnosis, prognosis, and cause of cancer. *Critical Reviews in Clinical Laboratory Sciences*, *48*(4), 155-170.

136.   Erlinger, T. P., Platz, E. A., Rifai, N., & Helzlsouer, K. J. (2004). C-reactive protein and the risk of incident colorectal cancer. *Jama*, *291*(5), 585-590.

137.   Vincent, J. L., Sakr, Y., Sprung, C. L., Ranieri, V. M., Reinhart, K., Gerlach, H., ... & Sepsis Occurrence in Acutely Ill Patients Investigators. (2006). Sepsis in European intensive care units: results of the SOAP study. *Critical Care Medicine*, *34*(2), 344-353.

138.   Enguix, A., Rey, C., Concha, A., Medina, A., Coto, D., & Diéguez, M. A. (2001). Comparison of procalcitonin with C-reactive protein and serum amyloid for the early diagnosis of bacterial sepsis in critically ill neonates and children. *Intensive Care Medicine*, *27*(1), 211-215.

139.   Castelli, G. P., Pognani, C., Meisner, M., Stuani, A., Bellomi, D., & Sgarbi, L. (2004). Procalcitonin and C-reactive protein during systemic inflammatory response syndrome, sepsis and organ dysfunction. *Critical Care*, *8*(4), 234-241.

140.   Kordass, U., Carlson, R., Stein, V. M., & Tipold, A. (2016). Measurements of C-reactive protein (CRP) and nerve-growth-factor (NGF) concentrations in serum and urine samples of dogs with neurologic disorders. *BMC veterinary research*, *12*(1), 7-15.

141.   Chuang, Y. C., Tyagi, V., Liu, R. T., Chancellor, M. B., & Tyagi, P. (2010). Urine and serum C-reactive protein levels as potential biomarkers of lower urinary tract symptoms. *Urological Science*, *21*(3), 132-136.

142.   Tanaka, T., Narazaki, M., & Kishimoto, T. (2014). IL-6 in inflammation, immunity, and disease. *Cold Spring Harbor Perspectives in Biology*, *6*(10), a016295.

143.   Hou, T., Huang, D., Zeng, R., Ye, Z., & Zhang, Y. (2015). Accuracy of serum interleukin (IL)-6 in sepsis diagnosis: a systematic review and meta-analysis. *International journal of clinical and experimental medicine*, *8*(9), 15238-15243.

144.   Naugler, W. E., & Karin, M. (2008). The wolf in sheep's clothing: the role of interleukin-6 in immunity, inflammation and cancer. *Trends in molecular medicine*, *14*(3), 109-119.

145.   Wong, H. R., Walley, K. R., Pettilä, V., Meyer, N. J., Russell, J. A., Karlsson, S., ... & Lindsell, C. J. (2015). Comparing the prognostic performance of ASSIST to interleukin-6 and procalcitonin in patients with severe sepsis or septic shock.*Biomarkers*, *20*(2), 132-135.

146.   Calandra, T., Gerain, J., Heumann, D., Baumgartner, J. D., & Glauser, M. P. (1991). High circulating levels of interleukin-6 in patients with septic shock: evolution during sepsis, prognostic value, and interplay with other cytokines. *The American Journal of Medicine*, *91*(1), 23-29.

147.   Battaglia, T. M., Masson, J. F., Sierks, M. R., Beaudoin, S. P., Rogers, J., Foster, K. N., & Booksh, K. S. (2005). Quantification of cytokines involved in wound healing using surface plasmon resonance. *Analytical Chemistry*, *77*(21), 7016-7023.

148.   Chou, T. H., Chuang, C. Y., & Wu, C. M. (2010). Quantification of Interleukin-6 in cell culture medium using surface plasmon resonance biosensors. *Cytokine*, *51*(1), 107-111.

149.   Zhu, X., Zhuo, X., Li, Q., Yang, Z., & Wang, J. (2016). Gold nanobipyramid-supported silver nanostructures with narrow plasmon linewidths and improved chemical stability. *Advanced Functional Materials*, *26*(3), 341-352.

150.   Wang, G., Wang, C., Yang, R., Liu, W., & Sun, S. (2017). A Sensitive and Stable Surface Plasmon Resonance Sensor Based on Monolayer Protected Silver Film. *Sensors*, *17*(12), 2777-2785.

151.   Chen, W., Thoreson, M. D., Ishii, S., Kildishev, A. V., & Shalaev, V. M. (2010). Ultra-thin ultra-smooth and low-loss silver films on a germanium wetting layer. *Optics Express*, *18*(5), 5124-5134.

152.   Logeeswaran, V. J., Kobayashi, N. P., Islam, M. S., Wu, W., Chaturvedi, P., Fang, N. X., & Williams, R. S. (2008). Ultrasmooth silver thin films deposited with a germanium nucleation layer. *Nano Letters*, *9*(1), 178-182.

153.   Cheng, Z., Wang, Z., Gillespie, D. E., Lausted, C., Zheng, Z., Yang, M., & Zhu, J. (2015). Plain silver surface plasmon resonance for microarray application. *Analytical Chemistry*, *87*(3), 1466-1469.

154.   Wang, Z., Cheng, Z., Singh, V., Zheng, Z., Wang, Y., Li, S., & Zhu, J. (2014). Stable and sensitive silver surface plasmon resonance imaging sensor using trilayered metallic structures. *Analytical Chemistry*, *86*(3), 1430-1436.

155.   Ke, L., Lai, S. C., Liu, H., Peh, C. K. N., Wang, B., & Teng, J. H. (2012). Ultrasmooth silver thin film on PEDOT: PSS nucleation layer for extended

surface plasmon propagation. *ACS Applied Materials & Interfaces*, *4*(3), 1247-1253.

156. Wróbel, P., Stefaniuk, T., Trzcinski, M., Wronkowska, A. A., Wronkowski, A., & Szoplik, T. (2015). Ge wetting layer increases ohmic plasmon losses in Ag film due to segregation. *ACS Applied Materials & Interfaces*, *7*(17), 8999-9005.

157. Shir, D., Ballard, Z. S., & Ozcan, A. (2016). Flexible plasmonic sensors. *IEEE Journal of Selected Topics in Quantum Electronics*, *22*(4), 12-20.

158. Smith, J. G., Faucheaux, J. A., & Jain, P. K. (2015). Plasmon resonances for solar energy harvesting: a mechanistic outlook.*Nano Today*, *10*(1), 67-80.

159. Kossoy, A., Merk, V., Simakov, D., Leosson, K., Kéna-Cohen, S., & Maier, S. A. (2015). Optical and Structural Properties of Ultra-thin Gold Films. *Advanced Optical Materials*, *3*(1), 71-77.

160. Meng, Q. Q., Zhao, X., Lin, C. Y., Chen, S. J., Ding, Y. C., & Chen, Z. Y. (2017). Figure of merit enhancement of a surface plasmon resonance sensor using a low-refractive-index porous silica film. *Sensors*, *17*(8), 1846-1857.

161. Choi, B., Dou, X., Fang, Y., Phillips, B. M., & Jiang, P. (2016). Outstanding surface plasmon resonance performance enabled by templated oxide gratings. *Physical Chemistry Chemical Physics*, *18*(37), 26078-26087.

Abbreviations and Acronyms

AFM	atomic force microscopy
BD	Blu-ray disc
BSA	Bovine Serum Albumin
BW-SPR	Bloch wave surface plasmon resonance
CCD	charge-coupled device
CNC	computer numerical control
COC	cyclic olefin copolymer
CRP	C-reactive protein
EDC	1-ethyl-4 (3-dimethylaminopropyl) carbodiimide hydrochloride
EDS	Energy-dispersive X-ray spectroscopy
ELISA	enzyme-linked immunosorbent assay
EM	electromagnetic
FDTD	finite-difference time-domain
FOM	figure of merit
FWHM	full width at half maximum
GTF2b	general transcription factor IIB
IgG	immunoglobulin G
IL6	Interleukin-6 protein
IR	Infrared
LED	light-emitting diode

LOC   lab-on-a-chip

LOD   limit of detection

LOQ   limit of quantification

LSPR   localized surface plasmon resonance

MES   2-(N-morpholino)ethanesulfonic acid

MHDA   mercaptohexadecanoic acid

MUOH   mercaptoundecanol

MW   molecular weight

NHS   n-hydroxysulfosuccinimide

PBS   phosphate buffered saline

PC   polycarbonate

PDMS   polydimethylsiloxane

PLL-PEG   poly(L-lysine)-graft-poly(ethylene glycol) co-polymer

PML   perfect matched layers

PMMA   poly-methyl methacrylate

POC   point of care

QCM   quartz crystal microbalance

RGB   red-green-blue

RI   refractive index

RIU   refractive index units

RMS   root-mean-square

SAM   self- assembled monolayers

SD   standard deviation

SPR surface plasmon resonance

SPRi SPR imaging

TAA tumor-associated antigen

TIR   total internal reflection

TM   transverse-magnetic

UV/O_3 ultraviolet/ozone

Appendix A. Publications

Journal Articles:

1. Lopez-Muñoz, G. A., Estévez, M. C., Soler, M., & Lechuga, L. M. (2017). **Recent advances in nanoplasmonic biosensors: Applications and lab-on-a-chip integration.** *Nanophotonics*, *6*(1), 123-136.

2. López-Muñoz, G. A., Estévez, M. C., Peláez-Gutiérrez, E. C., Homs-Corbera, A., García-Hernandez, M. C., Imbaud, J. I., & Lechuga, L. M. (2017). **A label-free nanostructured plasmonic biosensor based on Blu-ray discs with integrated microfluidics for sensitive biodetection**. *Biosensors and Bioelectronics*, *96*, 260-267.

3. López-Muñoz, G. A., Estévez, M. C., Vázquez-García, M., Berenguel-Alonso, M., Alonso-Chamarro, J., Homs-Corbera, A., & Lechuga, L. M. (2018). **Gold/Silver/Gold trilayer films on nanostructured polycarbonate substrates for direct and label-free nanoplasmonic biosensing**. *Journal of Biophotonics*, e201800043.

Conferences and Courses:

1. Europt(r)ode XIV (2018), **Oral Presentation**, Silver/Gold nanostructures based on Blu-ray optical discs with integrated microfluidics for multiplexed label-free plasmonic biosensors. Napoli, Italy.

2. VIII International Congress on Analytical Nanoscience and Nanotechnology (NyNA 2017), **Oral Presentation**, Metallic nanostructures based on Blu-ray discs for multiplexed plasmonic biodetection. Barcelona, Spain.

3. 2nd Scientific Meeting of BNC-b Students (JPHD 2016),**Conference Organizer**, PhD students of Barcelona Nanotechnology Cluster, Barcelona, Spain.

4. Advanced Study Course on Optical Chemical Sensors (ASCOS 2015), **Participant Student**, Lab-on-a-disc biosensors, Porto, Portugal.

Appendix B. Sensing capabilities/performance of Plasmonic color laser printing

1.- Introduction

We describe the evaluation of the sensing performance of plasmonic gold nanostructures provided by Prof. Anders Kristersen from the Department of Micro- and Nanotechnology, Technical University of Denmark (TUD) to evaluate their suitability for label-free biosensing.

Plasmonic colors are based on engineering nanostructures that are generated by laser pulses which induce a transient local heat generation that leads to melting and reshaping of a thin metallic layer and a polymer layer forming isolated nanostructures. Depending on the laser pulse energy, different surface morphologies that support different plasmonic resonances leading to different color appearances can be created[1]. These structures are a promising, rapidly emerging research field that could have a large technological impact. The concept of color laser printing is illustrated in Fig. A.1. the printable plasmonic metasurface is composed of metal disks on top of dielectric pillars, hovering above a holey metal film[2]. This design with polymeric pillars can be implemented by nano-imprinting, roll-to-roll processing or injection molding technologies based on a master.

We decided to evaluate the sensing performance of different gold nanostructures fabricated by plasmonic color laser printing. This novel fabrication method, allows the possibility to have a wide variety of nanostructures with different shapes and materials in a fast and highly controlled manner. On the other hand, the presence of highly ordered plasmonic nanostructures allows using simple detection

---

[1] Zhu, X., Vannahme, C., Højlund-Nielsen, E., Mortensen, N. A., & Kristensen, A. (2016). Plasmonic colour laser printing. *Nature Nanotechnology*, 11(4), 325-329.

[2] Clausen, J. S., Højlund-Nielsen, E., Christiansen, A. B., Yazdi, S., Grajower, M., Taha, H., & Mortensen, N. A. (2014). Plasmonic metasurfaces for coloration of plastic consumer products. *Nano Letters*, 14(8), 4499-4504.

methods (transmission/reflection) to monitor the plasmonic peak position over the time.
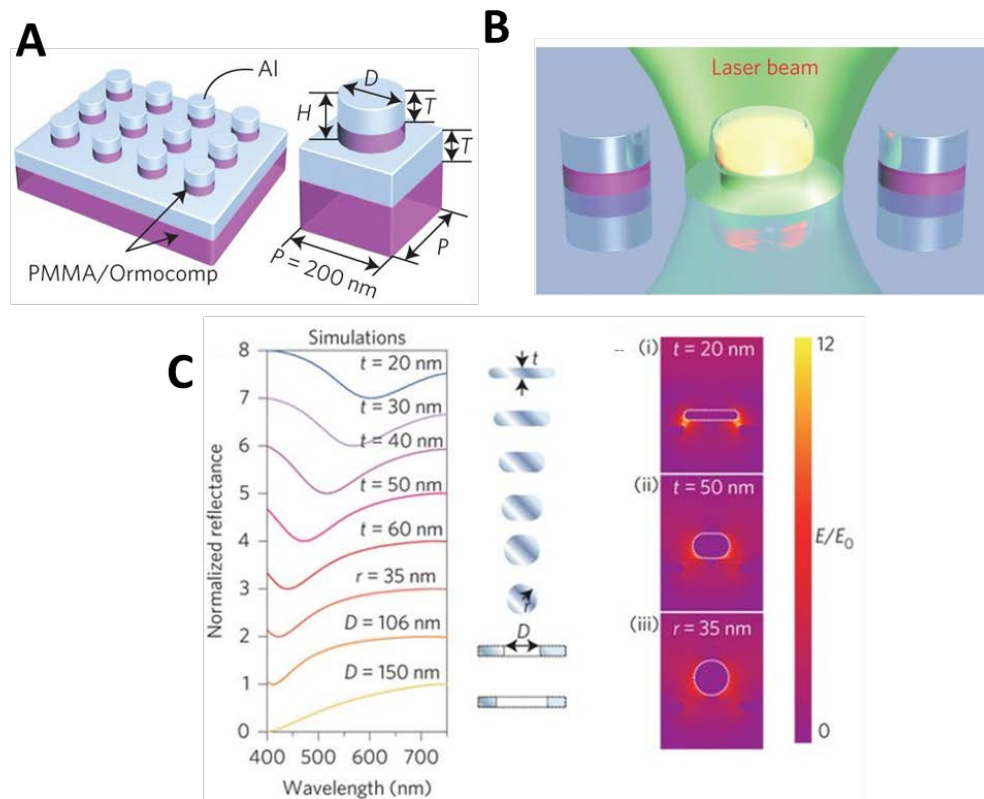
Figure A.1. (a) Schematic illustrations of the plasmonic metasurface and a unit cell with parameter settings, where the periodicity, P = 200 nm, the thickness of Al is T = 20 nm, the height of the pillars is H = 30 nm and the diameter of the disks is D. (b) A schematic illustration of laser printing. The printing is governed by photo–thermal reshaping of the metasurface. (c) Simulated spectra of models by imitating the morphology transformation in measurements and simulated electric field enhancements for selected morphologies of (i) t = 20 nm, (ii) t = 50 nm and (iii) r = 35 nm (sphere). Reprinted with permission from[1] 2016, Springer Nature.

2.- Materials and Methods

Integration of Nanostructured plasmonic chip. Individual nanostructured plasmonic gold chips (size of 1 cm^2) were provided by TUD. According to the information the structured chips are gold nanopillars with the following features:

- Substrate: Si coated with a thin PMMA Layer

- Pillar dimensions: 40 and 50 nm height in a square lattice with a pitch between the pillars of 200 nm.
- Au film thickness: 20 nm

To preliminary assess the performance for plasmonic sensing, we integrated the chip with a microfluidic flow cell in order to carry out real-time transmittance measurements in aqueous media. The flow cell was fabricated patterning a microfluidic channel (10 mm length and 1.5 mm width) in a 75 μm thick double-sided adhesive tape sheet. A COC slide (1 mm thickness) patterned with a CNC router was added as a cover to facilitate the connection of the fluidic tubes.

Experimental setup and optical characterization. The sensor chips were clamped to a custom-made optical platform in reflectance measurements (see Figure A.2). The chips were connected to a microfluidic system consisting of a syringe pump with adjustable pumping speed in order to guarantee a constant liquid flow, and a manually operated injection valve. Transmittance measurements were performed with a compact broadband light source (HL-2000-HP Ocean Optics, US) at a 90⁰ normal incidence angle with non-polarization. The reflected light was collected and fiber-coupled to a compact CCD spectrometer (Jazz, with a spectrum range between ≈ 350 to 1000 nm and 0.4 nm resolution, Ocean Optics, US). Reflectivity spectra were acquired every 3 ms, and 300 consecutive spectra were averaged to generate the spectrum to be analyzed. By using virtual instrumentation software (National Instruments, Labview, USA) it was possible to track the real-time changes in the resonance peak position (λSPP) via polynomial fit.
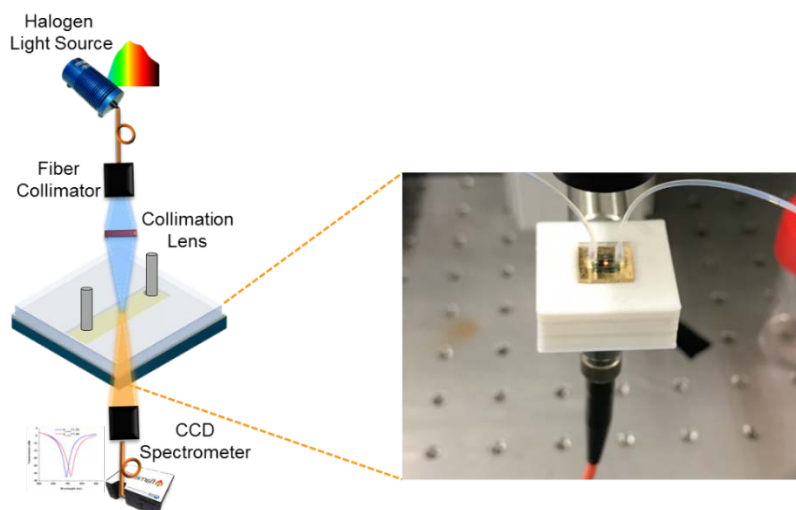
Figure A.2. Reflectance detection scheme. a) Normal incidence transmittance detection scheme. The insert shows the schematic representation of the set-up including the optical detection scheme and the microfluidic system.

3.- Results and Discussion

Characterization of plasmonic nanopillars chip. First we evaluated the plasmonic activity during a high refractive index change: from air to water (Δn= 0.333 RIU). As can be observed in figure A.2, the plasmonic activity is very weak for sensing purposed with a wide and not well defined plasmonic peak. To observe the plasmonic activity we normalize the signals considering the air signal as reference.
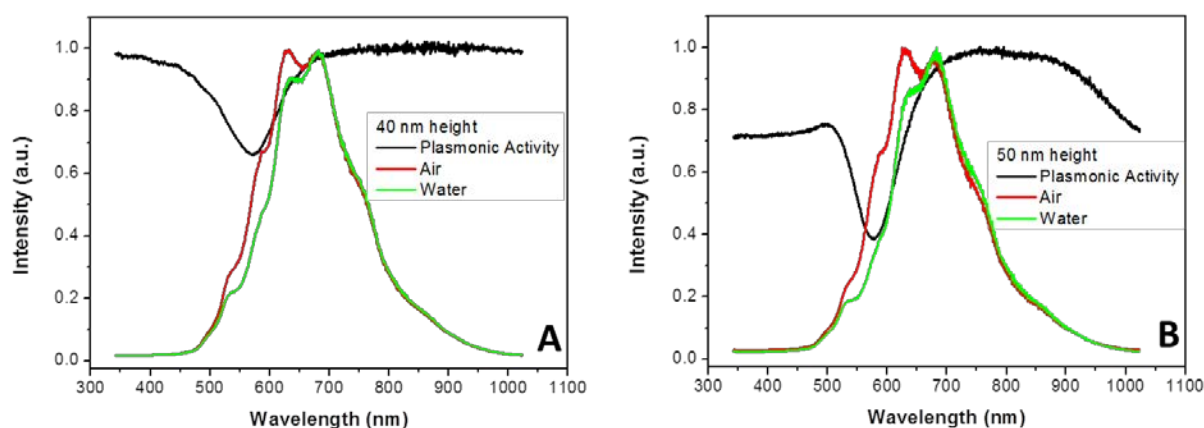
Figure A.3. Plasmonic activity in the two samples evaluated: a) 40 nm height and b) 50 nm height under a high refractive index change (air (green line) to water (red line) equivalent to

a Δn= 0.333 RIU). Black lines represent the plasmonic activity when the signals are normalized using the air signal as reference.

By tracking the wavelength shifts in the minimum value of the normalized signal we estimate the bulk refractive index (RI) sensitivity in both plasmonic surfaces using a solution of glycerol in water (10% glycerol in water, equivalent to a Δn= 0.0138 RIU). As can be observed in figure A.3, we obtained a poor signal to noise ratio, with low bulk sensitivity of only 81 nm·RIU^{-1} on average and an estimated LOD of only LOD= 8.1×10^{-4} RIU which is not very suitable for biosensing applications.
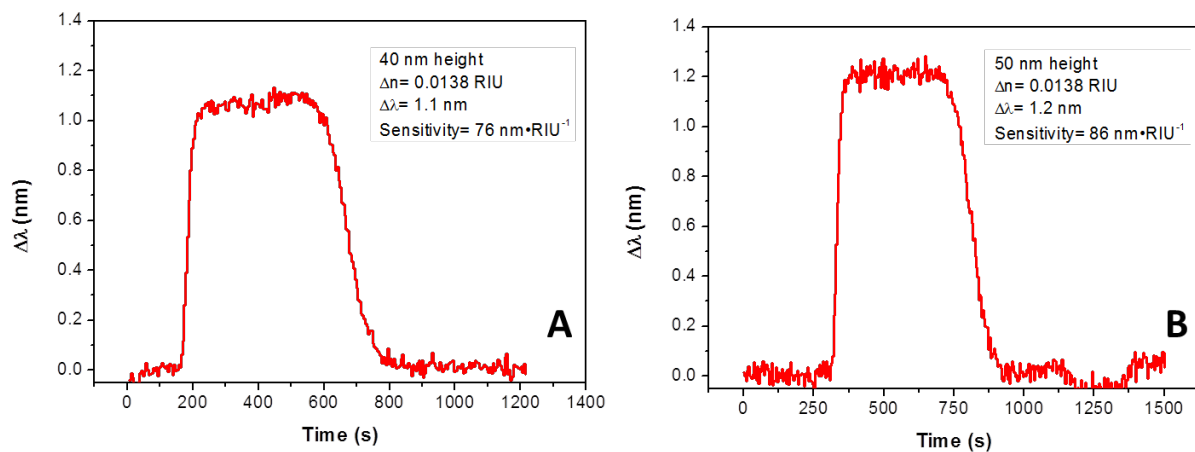
Figure A.4. Bulk refractive index sensitivity evaluation of booth samples: a) 40 nm height and b) 50 nm height using a 10% glycerol solution (Δn= 0.0138 RIU).

4.- Conclusion

Regarding the results obtained, we have observed a limited sensitivity (**≈ 81 nm·RIU^{-1} on average)**, which is worse than other nanostructures we have previously used, such as gold nanodisks **(350 nm·RIU^{-1})** or nanoslits **(425 nm·RIU^{-1})**. The experiments we have done are based on transmission in aqueous media under a normal incident light considering the low gold thickness layer (20 nm).

Although it could be possible to develop sensors with this novel technology, the limited sensitivity and signal to noise ratio make them not suitable for most biosensing applications. However, there are different approaches that can be

explored trying to improve the present limitations of these nanostructures. Considering the presence of high order nanostructures, it could be possible to explode other photonic effects related with grating coupling similar to those explored for the Blu-ray based gold nano-slits in this thesis to improve the sensing performance and the signal-to-noise ratio. Another approach to improve the sensing performance could be related to the evaluation of different metallic layer thicknesses and polarization of light in order to improve the excitation of the plasmonic resonances.

Finally, this technology offers a high flexibility to generate and tune plasmonic nanostructures in a highly controlled and simple manner opening a wide field of research for their potential use in biosensing platforms.

Appendix C. Sensing performance of Plasmonic gold nanowire arrays

1.- Introduction

We describe the evaluation of the sensing performance of commercially plasmonic gold nanowire arrays provided by the company Nanosens (The Netherlands) to check their suitability for label-free biosensing.

Plasmonic nanowire arrays are top down fabricated with tunable sub-20 nm separation nanogaps without the use of chemical etching or milling of the metallic layer and with a high control in the nanogaps separation. These arrays are suitable and attractive for plasmonic applications mainly due to the high confinement of plasmon resonances[3]. The high density of the nanowire arrays and the high confinement of the near-field electromagnetic fields allow to achieve localized surface plasmon resonance. Even more, when the gap distance is less than 10 nm there is an extra enhancement of the electromagnetic field by the "coupling effect" phenomenon. This enhancement on the electromagnetic field on the surface of the nanogaps can dramatically enhance the detection of molecules localized in the nanogaps due to the increase surface of "hotspots"[4].

We decided to evaluate the sensing performance of the provided gold nanowire arrays fabricated by top-down methods in wafer scale (see Figure A.5). These structures might have a high biosensing performance considering the increase surface of "hot spots" which are well known to allow an enhanced biodetection due to the high confinement and enhancement of the electromagnetic fields. On the other hand, the presence of highly ordered plasmonic nanostructures allows taking advantage of plasmonic grating coupling effect.

---

[3]Le Thi Ngoc, L., Jin, M., Wiedemair, J., van den Berg, A., & Carlen, E. T. (2013). Large area metal nanowire arrays with tunable sub-20 nm nanogaps. *Acs Nano*, 7(6), 5223-5234.

[4] Jin, M., Zhu, Y., Van Den Berg, A., Zhang, Z., Zhou, G., & Shui, L. (2016). Wafer-scale fabrication of high-density nanoslit arrays for surface-enhanced Raman spectroscopy. *Nanotechnology*, 27(49), 49LT01-49LT09.
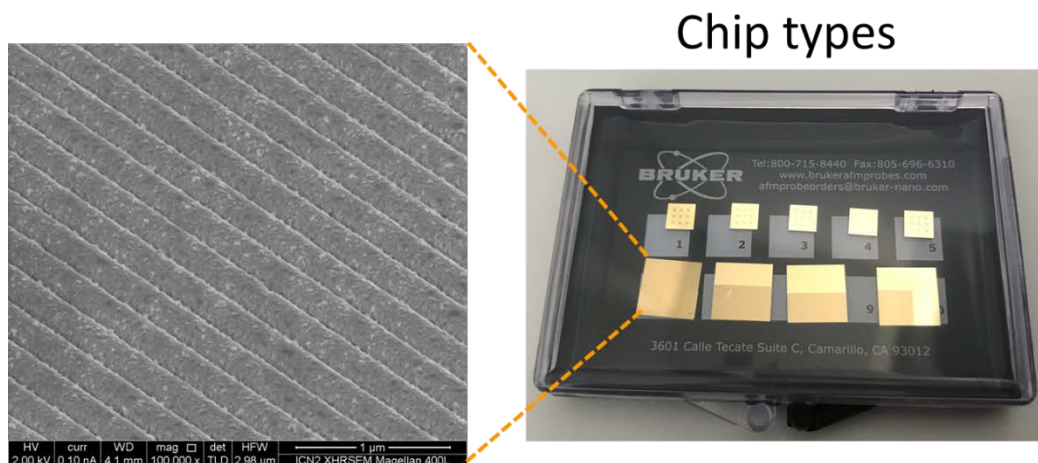
Figure A.5. Image of the evaluated plasmonic chips and a Scanning Electron Microscopy (SEM) image (insert) of the plasmonic nanogaps.

2.- Materials and Methods

Integration of Nanostructured plasmonic chip. Individual nanostructured plasmonic gold chips (size of 1 cm^2) were provided by Nanosens. According to the information the structured chips are gold nanogaps with the following features:

- Substrate: Si/coated with thin SiN
- Au gap: sub 20 nm with some local points of sub 10 nm (designated as local hot spots, where the sensitivity can be significantly enhanced).
- Pitch of the gap: 250 nm
- Au thickness: around 150 nm

To preliminary assess the performance for plasmonic sensing; we integrated the chip with a microfluidic flow cell in order to carry out real-time measurements in aqueous media. The flow cell was fabricated patterning a microfluidic channel (10 mm length, 1.5 mm width) in a 75 μm thick double-sided adhesive tape sheet. A COC slide (1 mm thickness) patterned with a CNC router was added as a cover to facilitate the connection of the fluidic tubes (see Figure A.6).
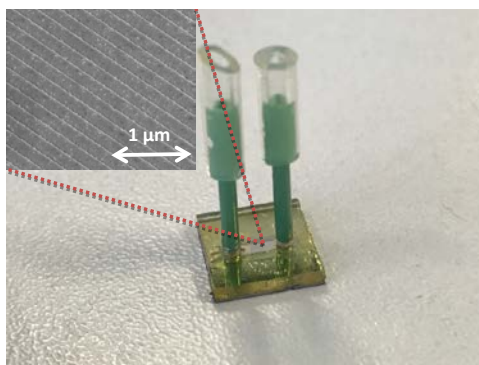
Figure A.6. Image of the integrated chip with the microfluidics channel and a Scanning Electron Microscopy (SEM) image (insert) of the plasmonic nanogaps.

Experimental setup and optical characterization. The sensor chips were clamped to a custom-made optical platform (see Figure A.7). The chips were connected to a microfluidic system consisting of a syringe pump with adjustable pumping speed in order to guarantee a constant liquid flow, and a manually operated injection valve. Reflectance measurements were performed under TM-polarization of a compact broadband light source (HL-2000-HP Ocean Optics, US) at different incident angles (ranging from 30⁰ to 70⁰). The incident excitation plane was perpendicularly aligned to the nanogaps direction.

The reflected light was collected and fiber-coupled to a compact CCD spectrometer (Jazz, with a spectrum range between ≈ 350 to 1000 nm and 0.4 nm resolution, Ocean Optics, US). Reflectivity spectra were acquired every 3 ms, and 250 consecutive spectra were averaged to generate the spectrum to be analyzed. By using virtual instrumentation software (National Instruments, Labview, USA) it was possible to track the real-time changes in the resonance peak position (λ_{SPP}) *via* polynomial fit. The bulk refractive index (RI) sensitivity and full width at half maximum (FWHM) of the sensor as a function of the incidence angle, were determined by flowing solutions of HCl in water (ranging from a RIU between 1.36322 and 1.34207 RIU).
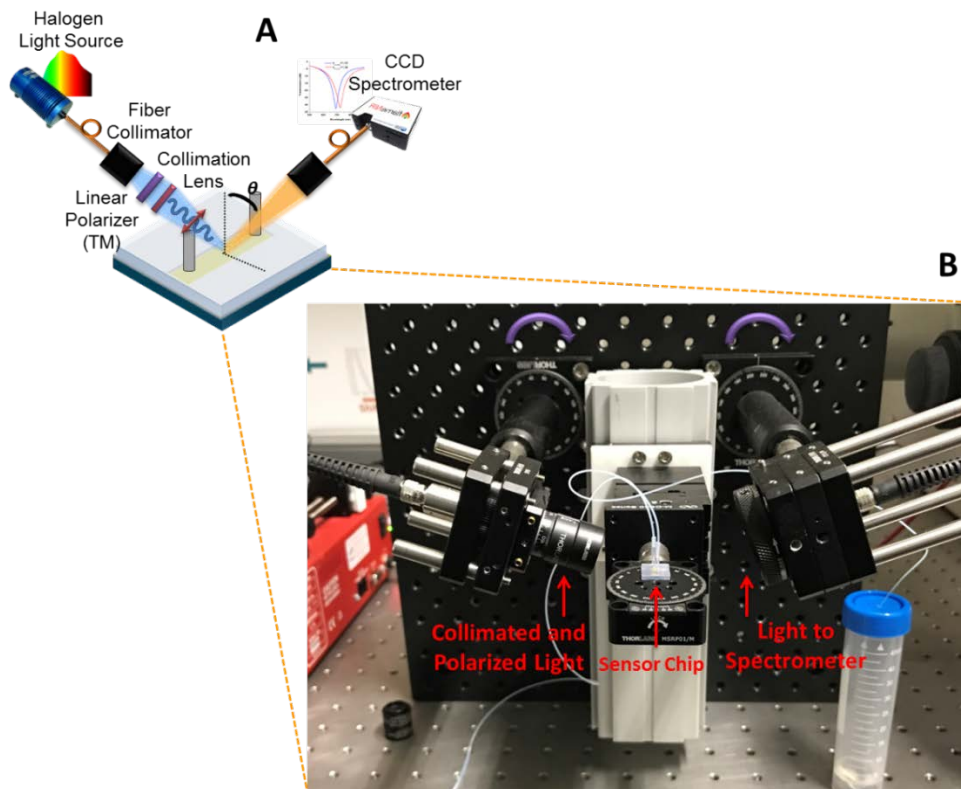
Figure A.7. Reflectance detection scheme and experimental set-up employed. a) Variable angle (30º-70º deg) reflectance detection scheme. b) Experimental set-up including the optical detection scheme and the microfluidic system.

3.- Results and Discussion

Characterization of plasmonic nanogaps chip. Different angles of incident light (between 30º-70º) were studied for the reflection measurements in order to evaluate its influence on the sensing performance due to the possible generation of other resonant modes under oblique-angle incident light. Reflection spectra were collected in water (n=1.33 RIU).

Figure A.8a, shows the reflectance spectra for the plasmonic nanogaps under different angles of incident light. An improvement in the narrow and definition of the resonance peak λ_{SPP} can be observed as the incidence angle increases, with a decrease in the full width at half maximum (FWHM). This behavior can be correlated with the possibility of inducing other resonant modes in the nanostructures.

The influence of the angle of the incident light was also studied by evaluating aqueous solutions with different RI. From the generated spectra, both bulk RI sensitivity and FWHM were extracted. As can be observed in Figures A.8b and A.8c, a higher incident angle promotes an increase in sensitivity and a decrease in FWHM for both thicknesses. Maximum bulk sensitivity and minimum FWHM values were obtained at 70° incident angle of light. A maximum sensitivity value of **220 nm·RIU^{-1}** with FWHM values of 37 nm have been achieved for this value of the incident light angle.
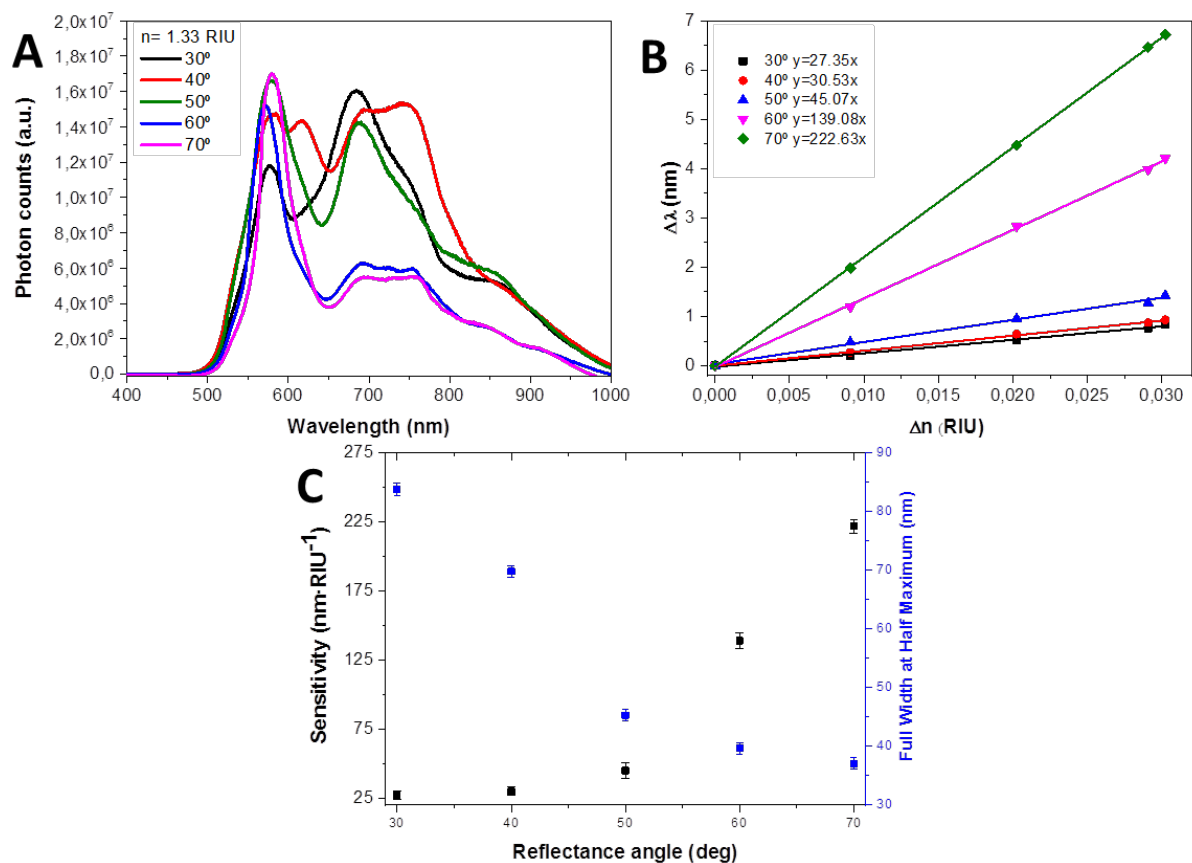
Figure A.8. Optical Characterization of plasmonic chips. (a) Variation of the reflectance spectra in water (n=1.33 RIU) of nanostructured nanogaps chip varying the oblique light incidence angle. (b) Calibration curves and bulk sensitivity determination for the chip varying the oblique light incidence angle. (c) Variation of the bulk sensitivity (*black*) and FWHM linewidth (*blue*) as function of the angle of the incidence light.

4.- Conclusion

Regarding the results obtained, we have observed a limited sensitivity (**≈ 220 nm·RIU^{-1}**), which can be comparable to or slightly worse than other nanostructures we have previously used, such as gold nanodisks **(350 nm·RIU^{-1})** or nanoslits **(425 nm·RIU^{-1})**. The experiments we have done are based on reflection in aqueous media and we have changed the angle of the incident light in order to evaluate its influence in the performance. Similarly to what we have previously obtained, higher angles of light result in better performance, but even in the best conditions (70º) the sensitivity is moderate.

Although this technology is attractive due to the possibility to get nanostructured substrates in wafer scale with a high precision in the nanogaps distances, it´s necessary a deep study of the nanostructures trying to improve their sensing performance to make them suitable for most biosensing applications. However, they offer the possibility to explode the photonic effects related with grating coupling to improve the sensing performance and signal-to-noise ratio. One approach to improve the sensing performance could be related with the evaluation of different metallic layer thicknesses trying to improve the excitation of the plasmonic resonances.

Finally, this technology offers a high control of the nanogaps dimension in plasmonic nanostructures, and as consequence in the "coupling effect" for a sensitive detection of molecules. The simple control of the nanogaps dimension opens an attractive field of research for biosensing platforms based on surface-enhanced Raman spectroscopy and plasmon resonances.